August 2013

Evaluating the Summer Thermal Structure of Southern Green Bay, Lake Michigan

Brice Grunert
University of Wisconsin-Milwaukee

EVALUATING THE SUMMER THERMAL STRUCTURE OF SOUTHERN GREEN BAY, LAKE MICHIGAN

by

Brice Grunert

A Thesis Submitted in

Partial Fulfillment of the

Requirements for the Degree of

Master of Science

in Freshwater Sciences and Technology

at

The University of Wisconsin – Milwaukee

August 2013

ABSTRACT

EVALUATING THE SUMMER THERMAL STRUCTURE OF
SOUTHERN GREEN BAY, LAKE MICHIGAN

by

Brice Grunert

The University of Wisconsin – Milwaukee, 2013
Under the Supervision of Professor J. Val Klump

The summer thermal structure of southern Green Bay, Lake Michigan was evaluated using cable moorings equipped with thermistors and a near real-time coastal monitoring buoy. The net heat flux for the southern bay was calculated over the study period. Cold water intrusions from Lake Michigan were tracked using water temperature, with the path of these water masses tracking along the western shore of Green Bay. Water clarity was measured across the study region as k_d. Surface diel warming was evaluated and compared with meteorological forcing variables and sensible and latent heat flux to determine the effect of water clarity on the overall thermal structure of Green Bay for the study period. Interannual climate and variation in observed thermal structure at a station in the bay is considered between 2011 and 2012.

TABLE OF CONTENTS

LIST OF FIGURES

LIST OF TABLES

ACKNOWLEDGEMENTS

Over the years, there have been too many people to mention that have helped me become the person that I am today and that I will be in the future. But there are those that I know have made a profound influence on my character, have supported me, and have further motivated me to make a difference in both the lives of those around me and in the world we live.

First, I would like to thank members of my committee, Dr. Hector Bravo, Dr. Mike Zorn, and Dr. John Janssen, for being patient and extremely helpful over the years. To all the students and faculty at SFS who have taken the time to help or simply talk with me about my work or my future. They are a great group of people and I can't thank them enough. In particular, Tom Hansen has been extremely helpful and patient with me.

I would like to thank Dr. Harvey Bootsma. He introduced me to the world of limnology and he is largely responsible for the cascade of events that led me here. I would also like to thank Dr. Rick Goetz, who I only knew for a short time but also had a remarkable impact on both my vision and imagination in the world of aquatic ecology.

Val's influence is something that often goes unnoticed, but it's constantly there in a solid, humble way. Looking back, I realize what I have learned from him and it is more than what is in the pages of this document. His wisdom and experience have taught me that approaching research with arrogance is seldom successful, but to always be aggressive and confident with my work. For that and the countless opportunities he has included me in, I am extremely grateful.

I would like to thank Captain Greg and Karen, for helping me smile every time I see them, whether in rough seas or "just peachy" days. Geoff has been instrumental in everything I do, from helping with moorings to lending tools, and he is certainly one of the hardest working individuals I know. These folks are the backbone of WATER and what will be SFS. Don and Kim have been a constant resource, both intellectually and in the field. I can gladly look back and be thankful for all their help. Shelby has been a shoulder to lean on in tough times and has helped me along with both her intellect and persistent enthusiasm.

Jim, Jerry, and Dr. Kahl have all played a vital role in my growth, intellectual capacities, and overall humor in the field. Their minds are clever and witty, but their intellect never gets in the way of enjoying life. And that skill is something I hope to inherit for those who deserve the final acknowledgements – my family.

I would like to thank my mother and father for working hard to give me the support that has led to all my successes, and for being there to help me learn from my failures. To my wife, who constantly reminds me that no matter how intelligent I am as a scientist, that doesn't make me a better person. She drives me to my full potential. And to my daughter Angie, who reminds me that a successful career and good parenting aren't synonymous, but they should be.

"And the waves that hit his face,
Marked the past
And the farrows on his skin
Oh, how time goes fast."

-Of Monsters and Men

"'And only as you gasp your dying breath shall you understand, your life amounted to no more than one drop in a limitless ocean!'

Yet what is any ocean but a multitude of drops?"

-David Mitchell

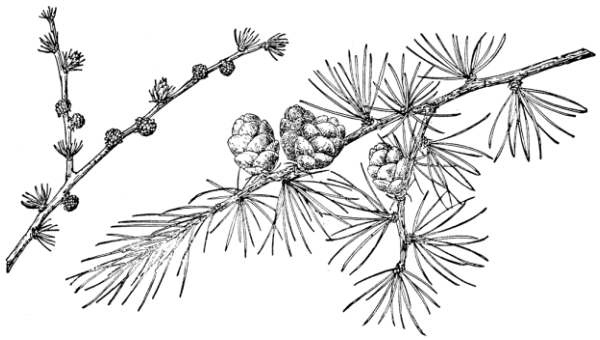

Chapter 1

1.1 Introduction

The Laurentian Great Lakes (herein: Great Lakes) are dynamic systems that respond quickly to meteorological forcing and external loadings yet are also large enough that energetic and chemical inputs are attenuated and modified within the environment. While many of the underlying physical, chemical, and biological processes have been extensively studied, meteorological forces, external loadings, and internal processes are changing as the climate changes, anthropogenic loading and agricultural practices change, and as the ecosystem continues to adjust to primarily past, but ongoing, aquatic invaders (WICCI 2011; Waples and Klump 2002; Hecky et al. 2004). Some, such as the reduction in PCB contamination exemplified in Green Bay, are for the better, while others, such as the recent resurgence of harmful algal blooms (HABs) in western Lake Erie, are certainly for the worse (Boyer 2008; Gebremariam 2013). Others, such as changes in wind direction, are still being considered. Thus, continual monitoring of the system with more advanced techniques is required to better understand what the current state of the system is to allow better predictions of where the system is headed.

While the most dynamic and unstable systems are the hardest to study, they also tend to be the most important from a sociocultural perspective, as the large populations, industrial presence, or vast agricultural influence that lead to anthropogenic changes within the environments often rely on the affected body of water. Green Bay, Lake Michigan, is an ideal example as the region's population relies on extensive dairy and crop farms within the Fox and Wolf River watersheds, an extremely dense industrial presence in the lower Fox River dominated by paper mills, and a popular tourist destination in the Door County peninsula. While the second largest metropolis in Wisconsin has benefited from these activities, the bay itself continues to struggle with persistent hypoxia and anoxia. The threat

of a changing climate is predicted to exacerbate the anthropogenic-induced hypoxia which persists in the bay. Understanding the driving physical variables within the system is crucial to better understand how changes in nutrient and pollutant loading will continue to shape how the bay responds, both chemically and biologically.

1.2 Study Hypotheses

This study considers the thermal structure of Green Bay south of Chambers Island over the stratified period through spatially and temporally dense data sets. While the thermal structure can be dominated at times by internal processes, these processes originate through meteorological forcing. Thus, heat flux, wind speed and direction, and water clarity are considered to determine where heat is being trapped, transported, or simply passed through (e.g. returned to the atmosphere) within the system during the study period. The goal is that by better understanding these processes, the behavior of thermally distinct water masses and the overall thermal behavior of the bay will be understood within the context of the study period. To achieve this goal, several hypotheses were considered and tested:

1) Green Bay will exhibit a persistent, stable thermocline at sites with a depth greater than 15 meters, with shallower sites exhibiting temporary stratification due to cold water intrusions.

2) Water clarity will play a role in the initial distribution of incoming heat energy and will result in a greater likelihood of thermal stratification at more turbid sites in the context of depth differences.

3) During the period for which air temperature is warmer than surface water temperature, convective mixing within the water column will be reduced and water clarity will exhibit a stronger role in determining overall thermal structure of the water column, namely that the depth of the mixed layer will be shallower.

4) An unstable ABL (air temperature < surface water temperature) will occur earlier in the stratified season at sites with reduced water clarity.

5) Stations along the main axis of the bay and with a long fetch in the predominant wind direction will display a mixed layer depth which reacts predominantly to wind speed rather than water clarity.

1.3 Study Site

Green Bay is a shallow, elongated embayment (mean depth 14m) (Fig. 1.1). Riverine input results in an approximate inflow-outflow "residence time" of six years; however, warm surface bay waters flow into Lake Michigan's northwestern region and cold, bottom Lake Michigan waters flow into the bay in a reciprocal manner, allowing free exchange of water rather than a unilateral flow out of the bay. This exchange is strongly driven by the direction, persistence, and speed of regional winds and results in an actual residence time of approximately 6 months (Waples and Klump 2002; Klump et al. 2009). This process indicates a significant horizontal component to the movement of heat within the system

Cold water intrusions from Lake Michigan are variable in their flow rate and size. However, internal seiches within Green Bay have an approximate periodicity of 8 days along the long axis of the bay (southwest-northeast) and are closely tied to the activity of Lake Michigan (Kennedy 1982; Hamidi et al., in prep). The cold water intrusions have the majority of influence within the hypolimnion of the bay north of Chambers Island, but are known to travel south of Chambers Island, occasionally traveling as southerly as Station 8 (Fig. 1.2). These water masses play a major role in water exchange and stratification in lower Green Bay but are notoriously hard to track.

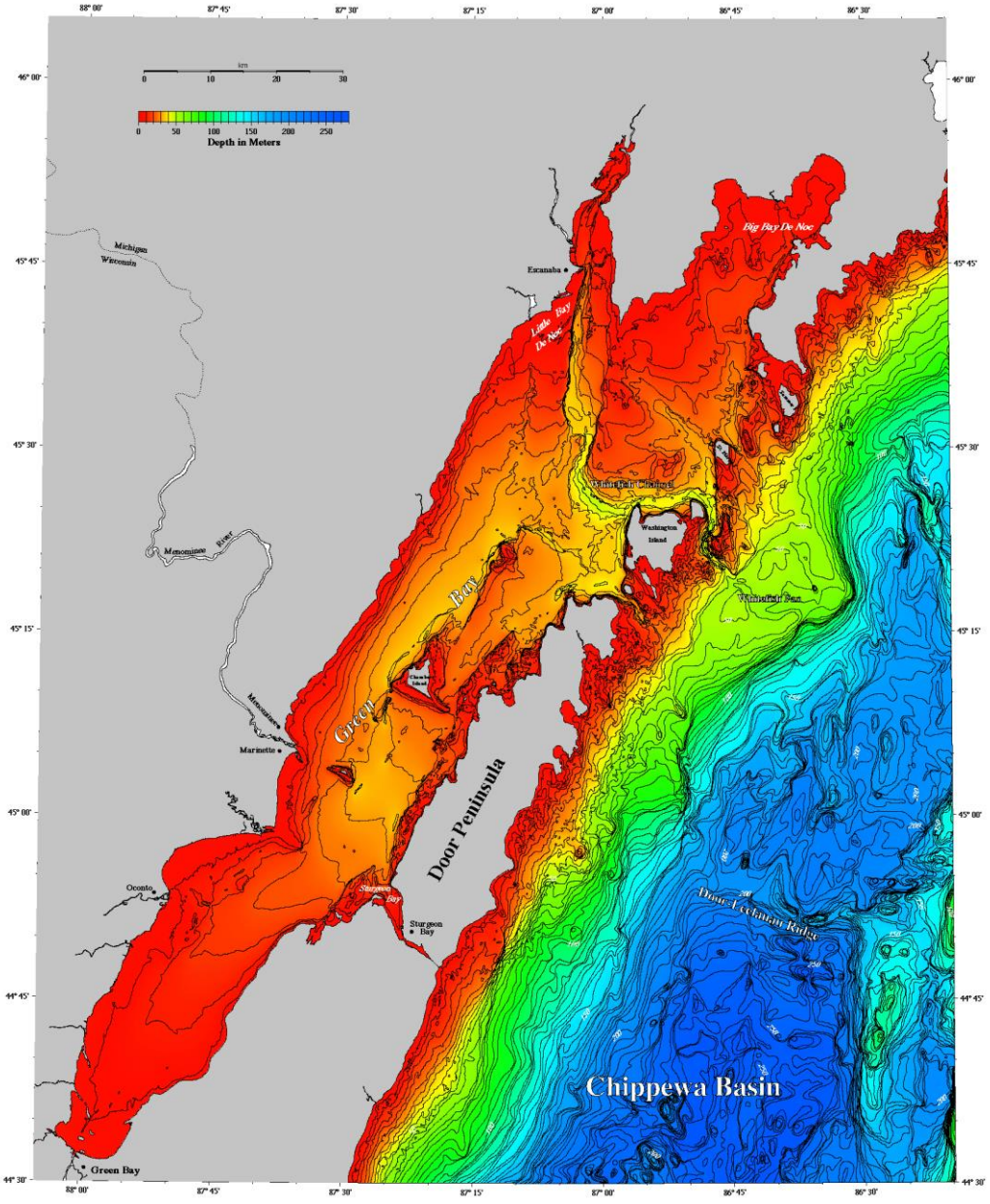

Figure 1.1. Green Bay bathymetry map.

Green Bay represents ~7% of the surface area and ~1.4% of the volume of Lake Michigan, yet receives water from one-third of the Lake Michigan watershed and one-third of the total nutrient loading to Lake Michigan. The bulk of this loading (~70%) comes from the Fox River, which enters the bay at the far southern end. The result has been eutrophic to

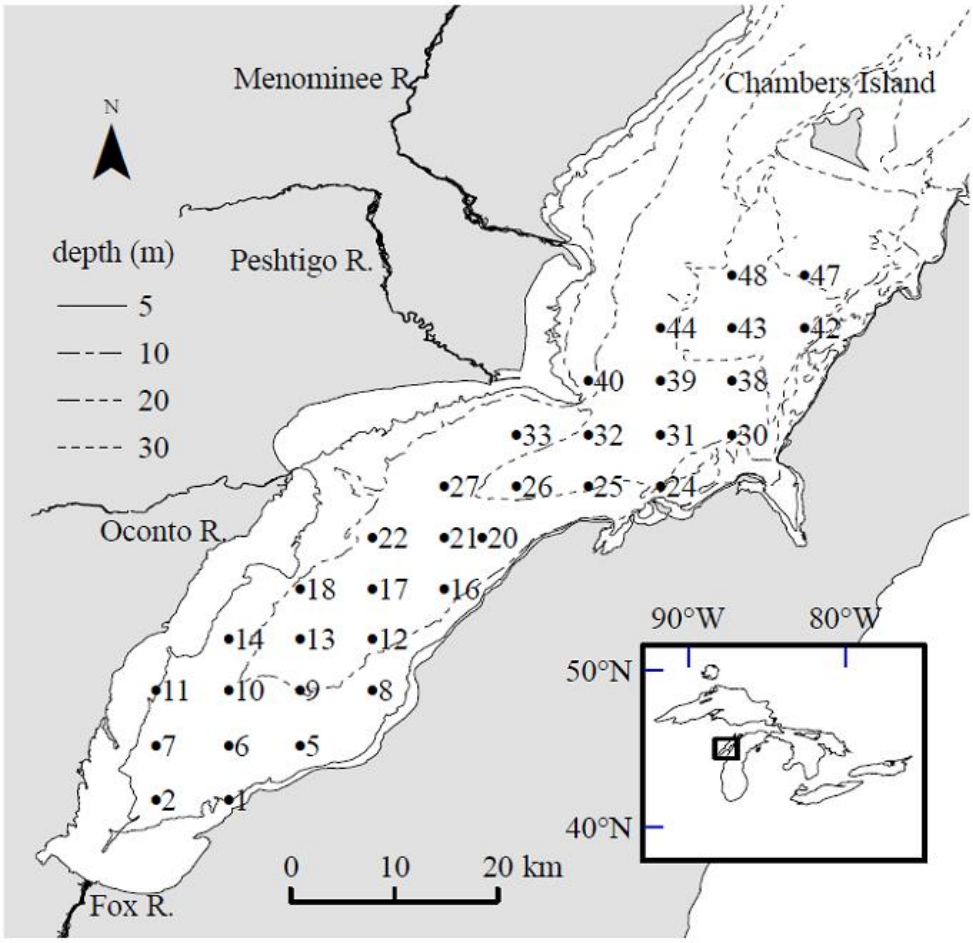

Figure 1.2. Map of Green Bay with station locations indicated by the black circles.

hypereutrophic conditions persisting in the bay for the last century, with Lower Green Bay designated as an Area of Concern (AOC) by the Canadian-US International Joint Commission (IJC), as well as being listed by the US EPA, due to persistent summer dissolved oxygen levels below 5 $mg \cdot L^{-1}$, and recurring hypoxia (< 2 $mg \cdot L^{-1}$) (Klump et al. 2009). While guidelines have been set by the IJC to decrease phosphorus inputs to the Great Lakes, a resurgence of harmful algal blooms has occurred in Green Bay, best exemplified by the similar but exaggerated conditions in the western and central basins of Lake Erie (Boyer 2008). This increase in pelagic productivity has led to an increase in occurrence and severity of benthic hypoxic events due to an increase in organic carbon settling into the

benthos, resulting in sediments that quickly become anoxic (Klump unpublished data). The result is occasional fish kills and a lack of an invertebrate forage base for fish, decreasing the ecological functioning of the system (Klump et al. 1997; Kastor, pers. comm.).

While the primary driver of benthic hypoxia in Green Bay is the anthropogenic-induced hypereutrophic conditions, the set up within this system for such conditions is the seasonal stratification typical of large temperate lakes such as the central basin of Lake Erie, where varying degrees of benthic anoxia have been linked to the time of formation and the stability of the thermocline (Lam et al. 1983). Green Bay hydrodynamic processes, and thus stratification, are similar to those seen in other parts of the Great Lakes, with the exception that Green Bay is relatively shallow, with depths progressively increasing from south to north where the bay exchanges water with Lake Michigan. The result is a dynamic, event-driven system that allows mixing and breakdown of the thermocline periodically throughout the summer with strong storm events (Klump, unpublished data). As in other systems, the frequency and longevity of these mixing events plays a critical role in the overall health of lower Green Bay (McInnes and Quigg 2010). The role of understanding the thermal structure of Green Bay becomes even more important when considering potential impacts on the bay due to climate warming and water quality as stress on freshwater supplies increases through the 21st century.

1.4 Thermal Structure

During the stratified period, Green Bay is dominated by two types of water. Southern bay water, due to warm water inputs from the Fox River and rapid heating and thorough mixing within the shallow environment, is warm (>15° C) from early to late May and increases in temperature through the summer (≥ 25° C). Cooling of these waters occurs primarily during fall turnover (mid-September). Cool northern bay waters maintain a stark temperature difference primarily through cold water intrusions from Lake Michigan. While

the northern region of Green Bay is deep enough to maintain stable stratification through the summer, incoming cold Lake Michigan waters are the dominant component to the persistence and stability of the thermocline throughout much of the bay south of Chambers Island. Even sites deeper than 15 meters (typically considered the shallowest depth for persistent stratification through the summer in Green Bay) would experience significant heating of the hypolimnion, and thus weakening of the thermocline, without these inputs. This is exemplified when considering historic temperature profiles between Chambers Island East and West. The western passage is dominated by substantial but episodic flows of cold Lake Michigan water, driven by wind speed and direction, which results in cold hypolimnion temperatures and a stable thermocline while shallower, Chambers East sites have a less stable thermocline that forms with cold water inputs and then is greatly deepened or broken down between these inputs.

These cold water intrusions will often travel much farther south than Chambers Island. While the cause of these cold water masses is known – strong, persistent southwesterly winds resulting in enhanced transport of warm, surface bay waters into Lake Michigan and the reciprocal return flow of cold, bottom Lake Michigan waters – the mechanics of how and when the flow travels into southerly waters is not well understood. Of particular interest is whether this is strictly Lake Michigan water or whether it is hypolimnetic northern Green Bay waters that have been displaced. However, the two are not necessarily distinct as significant mixing within the hypolimnion between these waters is expected. The main difference between hypolimnetic waters throughout the bay is the oxygen content of the waters.

1.5 Light and the Aquatic Environment

The behavior of light within pure water is well known (Kirk 1994; Pope and Fry 1997; others). The degree and significance of light scattering and absorbing particles within

the water column of lakes such as the Great Lakes, however, is not well known. Historically, chlorophyll was considered the primary absorber, with minerals and other inorganic particles comprising the bulk of the light scattering particles within the water column. However, chromophoric (or colored) dissolved organic matter (CDOM) is now considered a major player in the aquatic environment, as a primarily planktonic by-product in oceanic environments and primarily from allocthonous inputs in lakes and coastal environments (Gnanadesikan and Anderson 2009; Effler et al. 2010). Absorption behavior for phytoplankton and CDOM is relatively well-known (Kirk 1994; Babin et al. 2003; Effler et al. 2010). However, accurately portraying the absorption and scattering spectra for a particular water body is more difficult, as the concentration of the various light absorbing and scattering components is typically not known. Additionally, fluctuations in many of these components are expected based on the time of year and location within a specific water body.

This study considers the overall light extinction, or attenuation, coefficient (k_d or LEC), a composite of the absorption and scattering that has occurred within the water column above the depth of measurement. K_d, while not immediately helpful for determining specific spectral properties of the water, particularly for remote sensing, is useful as: 1) k_d indicates the contribution of solar irradiance at a particular depth to local heating (primarily) or biological productivity (secondarily) and 2) depending on the instrument, can indicate the general optical properties of the water column, e.g. CDOM rich or turbid waters will absorb exponentially more light of shorter wavelengths (Murtugudde et al. 2002; Effler et al. 2010). Some authors consider visible and infrared light within different depths of the water column due to the effect each has on local heating within the water column. Here, the attenuation of shortwave radiation is considered synonymous with the attenuation of light.

1.6 Water Clarity

Physical water parameters, such as temperature, current direction and speed, and water residence time, can significantly impact the biological activity of aquatic systems (McKinley and Wetzel 1979; King et al. 1999b). Typically, particulate and dissolved organic matter (POM and DOM, respectively) are seen as factors directly affecting aquatic biological systems by providing alternate trophic pathways (Wetzel 1992; Sadro et al. 2011) and altering primary productivity by more rapidly attenuating light (Frenette et al. 2006). However, POM and DOM can also affect the thermal structure of a water body, with indirect effects on subsequent dissolved oxygen levels and ecotype structure of the water column (Mazumder and Taylor 1994; Fee et al. 1996; Pérez-Fuentetaja et al. 1999; Snucins and Gunn 2000; Gunn et al. 2001; Houser 2006).

Water color and clarity have been found to dictate the depth of formation and the stability of the thermocline in small lakes in various environments (Fee et al. 1996; Pérez-Fuentetaja et al. 1999; Snucins and Gunn 2000; Houser 2006). The role of water color and clarity in large lake systems has been more contested, with speculation to the overall role in thermocline formation and depth of the mixed layer. Mazumder and Taylor (1994) found that water clarity played a role in Great Lakes' depth of stratification, albeit a smaller role than meteorological conditions. Simpson and Dickey (1981) also found that water clarity significantly affected the depth of stratification in oceanic systems during the summer period and suggested that it is crucial to modeling these systems, a finding supported by later studies (Schneider and Zhu 1998; Gnanadesikan and Anderson 2009). However, Mazumder and Taylor (1994) relied upon a sparse data set, likely resulting in inaccurate results for such a large, temporally and spatially complex system as the Great Lakes, and oceanic systems are not necessarily accurate representations of large lake environments as physical forcing variables can differ significantly due to the spatial scales of these two systems (Boyce 1974; Schwab and Beletsky 2003). Fee et al. (1996) suggested that water

clarity would not play a role in the thermal structure and stratification of large lakes (>500 ha), as beyond this size, meteorological forcing variables outlined by Boyce (1974) would play the dominant role in mixing depth and subsequent thermal structure.

Increases in solar radiation in the spring months causes the onset of stratification, starting with the appearance of a thermal bar that gradually moves across the surface until two layers of water with distinctly different temperatures form. Solar radiation is the primary variable dictating water surface temperature; however, it is not necessarily the primary variable dictating depth of the mixed layer and subsequent spatial resolution in the vertical thermal structure. In water bodies with a large fetch, or large lake systems with appropriate depth and size, other variables such as wind forcing, the Coriolis force, surface seiche, internal seiche and basin-scale currents play a larger role. Enhanced heating of the surface layer during the day can also lead to significant convective mixing as the surface waters cool in the evening while the underlying waters remain warmer. Depending on the scale, this mixing can be enough to erode the thermocline (King et al. 1997).

Arguably, solar radiation cannot play a significant role in determining the depth of the mixed layer in large lake environments such as the Great Lakes as the effect of solar radiation exponentially decreases as the size of the water body increases (and the depth of the mixed layer subsequently increases), while meteorological forcing variables often increase in intensity as the size of the water body increases (Boyce 1974; Liu and Ross 1980). However, while the vertical distribution of irradiance can be represented by an exponential function, this is inaccurate in shallow waters (<10m) (Simpson and Dickey 1981). Within the upper two to three meters of the water column, approximately one-third of the incident value has been absorbed (primarily longer wavelengths within the visible spectrum), resulting in enhanced heat attainment within the surface waters. Additionally, during the period of water column stratification in the Great Lakes, the atmospheric

boundary layer is at its peak stability (Blanken et al. 2011), which decreases the wind speeds and turbulent mixing (Liu and Ross 1980). In turbid environments where the majority of solar radiation is trapped within the upper 3m of the water column, such as Green Bay, Lake Michigan, the role of water clarity may increase to the point that it becomes a key component of the complex interactions that result in the observed mixed layer depth and thermal structure of the water column. Green Bay is a unique system to study the impact of these different meteorological factors, as it has characteristics of both large and small lakes. Its eutrophic conditions, depth and rapid response to changes in wind speed and direction are similar to conditions most often seen in small- to medium-sized lakes. However, it's fetch, internal and surface seiches (including effects from Lake Michigan), and thermal capacity are more closely aligned with large lakes (Mortimer 1978; Kennedy 1982). Ultimately, determining the fate of heat and the amount of solar radiation that is absorbed and translated into biochemical energy by phytoplankton will illuminate the transfer of heat throughout the water column. Additionally, this will indicate which variables are the driving forces behind the observed thermal structure of the water column.

During the formation of the thermocline, the high stability found within the atmospheric boundary layer may result in water clarity playing a large role in the formation and depth of thermal stratification. However, the observed depth of the mixed layer may depend upon large storm events periodically deepening the mixed layer. Thus, the observed mixed layer depth may reflect the strength and frequency of these events in combination with the effects of water clarity (Gorham and Boyce 1989). Thus, heat attained by POM and DOM via absorption of solar energy may be crucial to the overall thermal structure and thermocline stability in Green Bay as observed in oceanic studies (Kara et al. 2005).

The mechanics of how the thermocline forms and breaks down, as well as its stability and interaction with surface and meteorological conditions, is arguably the most

critical physical process to understand when attempting to remediate the biological conditions of Green Bay and other hypereutrophic environments throughout the Great Lakes (Gorham and Boyce 1989; Verburg and Antenucci 2010). Green Bay stratification is strongly dependent on the prevailing meteorological conditions and the thermal characteristics of the water column from the previous months (Schertzer et al. 1987). Within hypereutrophic aquatic environments, high rates of microbial activity, particularly in the benthos where organic matter accumulates, can deplete oxygen levels to hypoxic and anoxic levels in as little as a month after the onset of stratification, with hypoxic conditions largely contingent on the existing and future thermal structure of the water body (Burns et al. 2005; Dobiesz and Lester 2009; Valenta et al. 2012; Klump unpub. data). Considering that Green Bay and similar Great Lakes systems (i.e. Western Lake Erie, Saginaw Bay) rely upon water column mixing to re-oxygenate the benthos, understanding the thermal structure and seasonal cycle of the thermocline is critical to efforts to remediate ecosystem functioning within these environments. Concerns about increasing temperatures due to climate change have also led to efforts to better understand the coupled dynamics that can affect the benthic respiration rates within these systems. The data obtained in 2012 are crucial to this effort, as the abnormally hot and dry summer may allow the year to be a model for future conditions within the bay.

1.7 Heat Budget

One of the most powerful tools in understanding the thermal processes of a system such as Green Bay is to compose an energy or heat budget for the system. A heat budget allows for the driving variables – shortwave radiation, longwave radiation, sensible heat, latent heat, and advection – and their fluxes to be estimated, which in turn indicates the sources or sinks for heat within the water column at a given time, as well as illuminating movements of heat through the water column, both horizontally and vertically when spatial

data are sufficient. For temperate aquatic systems, shortwave radiative inputs are the driving force in the spring and early summer and the latent heat term is the dominant output beginning in late summer and into the fall, as the atmospheric boundary layer (ABL) becomes increasingly unstable with cooling air temperatures and warmer water temperatures (Blanken et al. 2011). A heat budget also summarizes the total heat exchange between the aquatic system and atmospheric forcing variables, with the sign of the flux indicating whether the lake is absorbing or releasing heat (an overall positive flux indicates heat is being absorbed, and a negative flux indicates heat is being released). Advection is calculated as the change in temperature unaccounted for by the air-sea heat flux and can be quite significant in some systems.

Chapter 2: Methods

2.1 Equipment

All observations were made during the months of June through October on monthly cruises in Green Bay at pre-determined stations which have been sampled in previous years (Fig. 2.1). High density, short term data sets collected during these cruises were supplemented by whole season moorings collecting data every 3 or 6 minutes from June or July through October, and a real-time coastal monitoring buoy collecting data every half hour. Thermal and light profiles were obtained through a combination of hand-lowered YSI (Dayton, OH) 6600 series Sondes equipped with temperature, fluorescence, turbidity, pH,

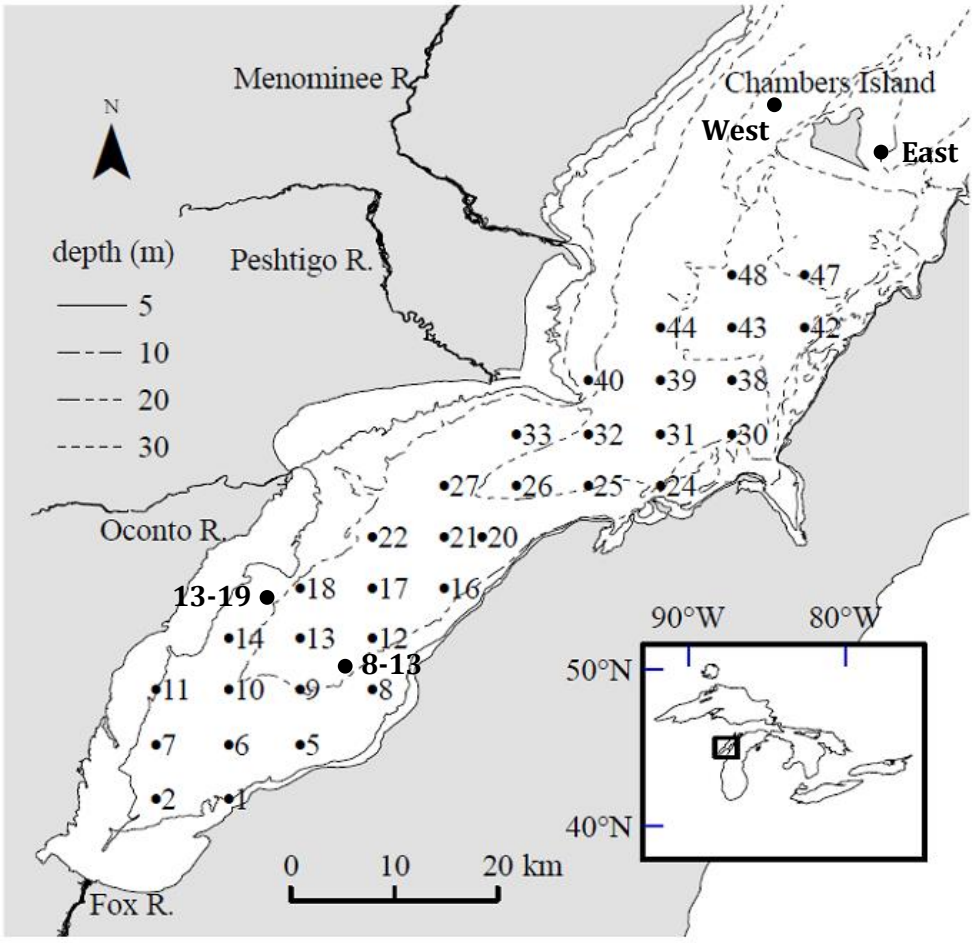

Figure 2.1. Map of Green Bay with station locations indicated by the black circles. Coarse depth contours are indicated within the figure.

dissolved oxygen, and conductivity sensors and Onset (Bourne, MA) HOBO pendants during the cruises, and wire moorings that remained in the bay during our absence (Fig. 2.2). Wire moorings were equipped with HOBO temperature and HOBO pendant temperature/light data loggers (herein HOBO loggers and HOBO pendants, respectively) at varying distances from the bottom, depending on the depth of the site (Table 2.1), and YSI 6600 series Sondes equipped with similar sensors as mentioned above were moored 1m from the bottom at most sites. Stations equipped with HOBO loggers included Stations 8, 8-13, 9, 13, 13-19, 21, 31, Chambers East (CE), and Chambers West (CW) (refer to Fig. 2.1 above for station locations). Stations 8, 8-13, 9, 13, 21, 31, CE, and CW were also equipped with HOBO pendants (Table 2.1). The mooring at Chambers West was snagged by a commercial fishing operation after approximately two weeks in the water. After retrieval, the mooring was redeployed but permanently lost after the second deployment. Some stations experienced

Table 2.1. Station ID, depth of station (meters), and the location of sensors (S#) within the water column at each station. Sensor values are measured in meters from the bottom. A indicates within the vicinity of the bottom sediments; S indicates a sensor located on a float at the water surface. * indicates a temperature/light logger.

Station ID	Station Depth	S1	S2	S3	S4	S5	S6	S7	S8	S9	S10
8	8.3	A	1	2*	4.7	S					
8-13	9.7	A	0.5	1	2*	4*	6.5*				
9	9.1	A	1*	2	4*	5.5*	S				
13	10.6	A	1	2*	4*	7*					
13-19	7.7	A	0.5	1	2	4					
21	15.8	A	1	2*	4*	7*	12*	S			
31	23.9	A	1	2	3	5	8*	12*	16*	19*	S
CE	20.5	A	1	3	5*	8*	11*	16*			
CW	28.3	1	5	9	12*	15*	18*	21*	S		

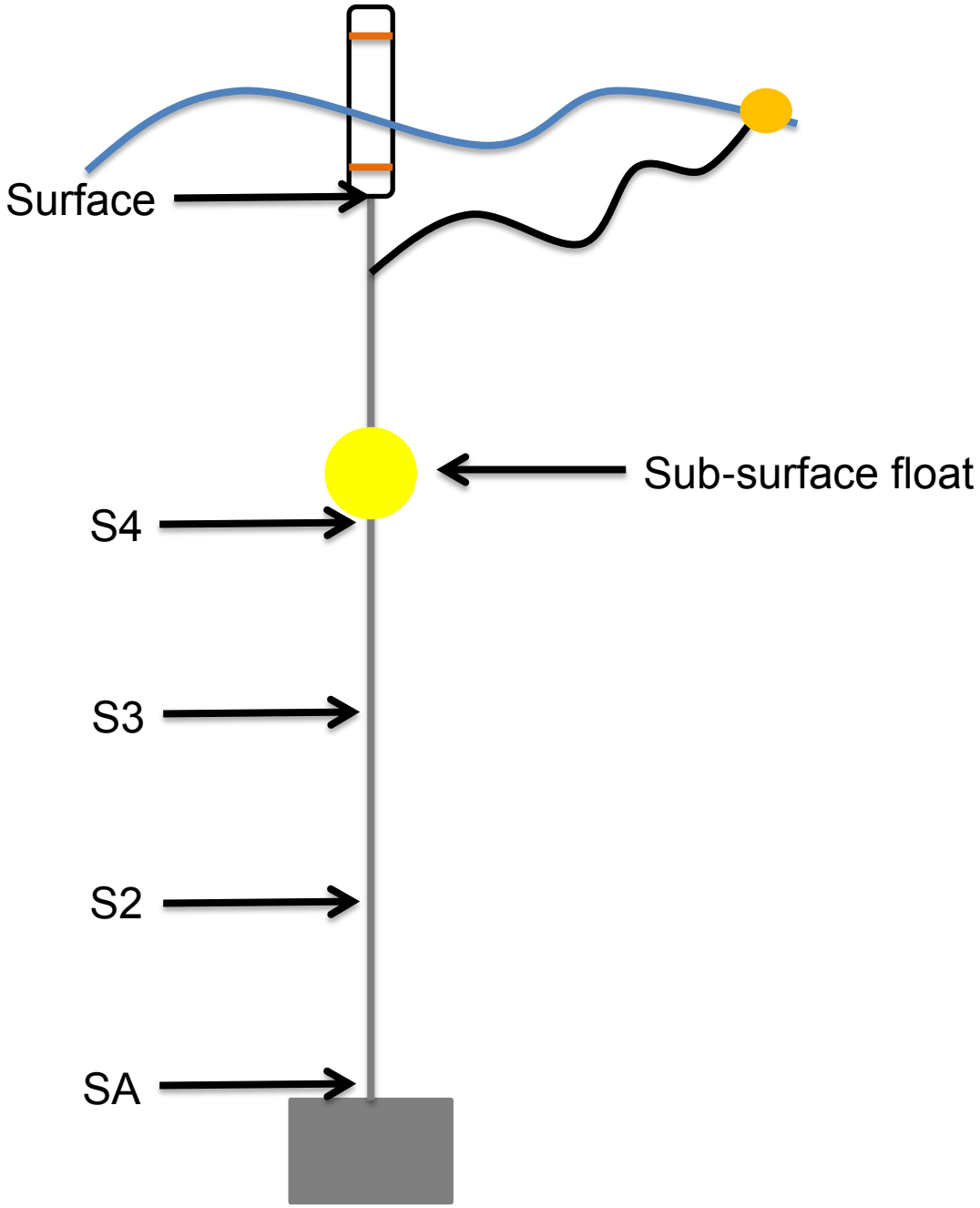

Figure 2.2. Schematic of a typical mooring in Green Bay, with S# indicating sub-surface sensors within the water column, SA indicating the sensor attached to the top of the anchor (typically at or very close to the sediment-water interface), and Surface indicating the surface sensor, housed in a small, protective PVC pipe attached to the base of the spar buoy.

one or more HOBO logger failures during a portion of the field season.

The HOBO pendants had an accuracy of ±0.53°C between temperatures of 0 and 50°C. Light measurement accuracy was based on relative light levels, with a response curve peaking at 900nm (100% response), with 80% response rates occurring from approximately 680-1050nm and overall responses gathered between 150-1200nm at diminishing response rates from the spectral peak between 680 and 1050nm (Appendix A). Irradiance was measured in lumens foot^{-2} (lum ft^{-2}). Sensor drift on an annual basis is less than 0.1°C.

At Station 17, both a wire mooring, equipped with a bottom Sonde, and a CB-1500 coastal monitoring buoy from Fondriest Environmental (Dayton, OH; herein buoy) were maintained (Fig. 2.3). The buoy was equipped with a Lufft WS501-UMB Compact Weather Station (Santa Barbara, CA) measuring temperature, relative humidity, global radiation (shortwave irradiance), air pressure, mean wind speed and direction (average wind speed

Figure 2.3. Image of the Fondriest Environmental buoy.

over a 2 minute period), and wind gust speed, a YSI 6600 series multi-parameter sonde measuring temperature, fluorescence, turbidity, pH, dissolved oxygen, and conductivity, and a Nexsens (Dayton, OH) temperature string with thermistors every 1m from 2-12m.

Measurements by the WS501-UMB were accurate for air temperature to ±0.2˚C within the conditions experienced. Relative humidity was measured in percent (%), with an accuracy of ±2%. Air pressure was measured in hectopascals (hPa, with 1 hPa=1mbar), with an accuracy of ±1.5hPa. Wind direction was measured from 0 to 360˚, with an accuracy of less than 3˚; however, compass accuracy on the Lufft is less than 10˚, which resulted in overall wind directional accuracy of ±13˚. Wind speed was measured as both mean and maximum (gust) wind speeds in meters second^{-1} (m s^{-1}), with an accuracy of 3% or ±0.3m s^{-1}. Global radiation was measured across a spectral range of 310-2800nm in Watts meter^{-2} (W m^{-2}), with a resolution of < 1 W m^{-2} and a daily expected uncertainty of less than 10%.

Thermal profiles were created for stations with moorings, as well as Station 17. Additionally, inter-annual variation was compared at Station 9 using data from 2011 (also collected using HOBO loggers). To more thoroughly compare these two years, climate rankings provided by the National Climatic Data Center (NCDC) were gathered. NCDC rankings are based on records from 1895 to the present year, with 1 being the coldest year on record, 118 (through 2012) being the warmest year on record, and maps being broken down by further rankings (Fig. 2.4). To simplify the rankings, we treated the coldest year on record as 0, the warmest year on record as 1, and determined the decimal rank for each month within each division by dividing by the number of years of record (119 for March and April, due to 2013 data being available, and 118 for the rest of the months). The value for each division was then averaged together by month and year to get an overall climate rank for the bay.

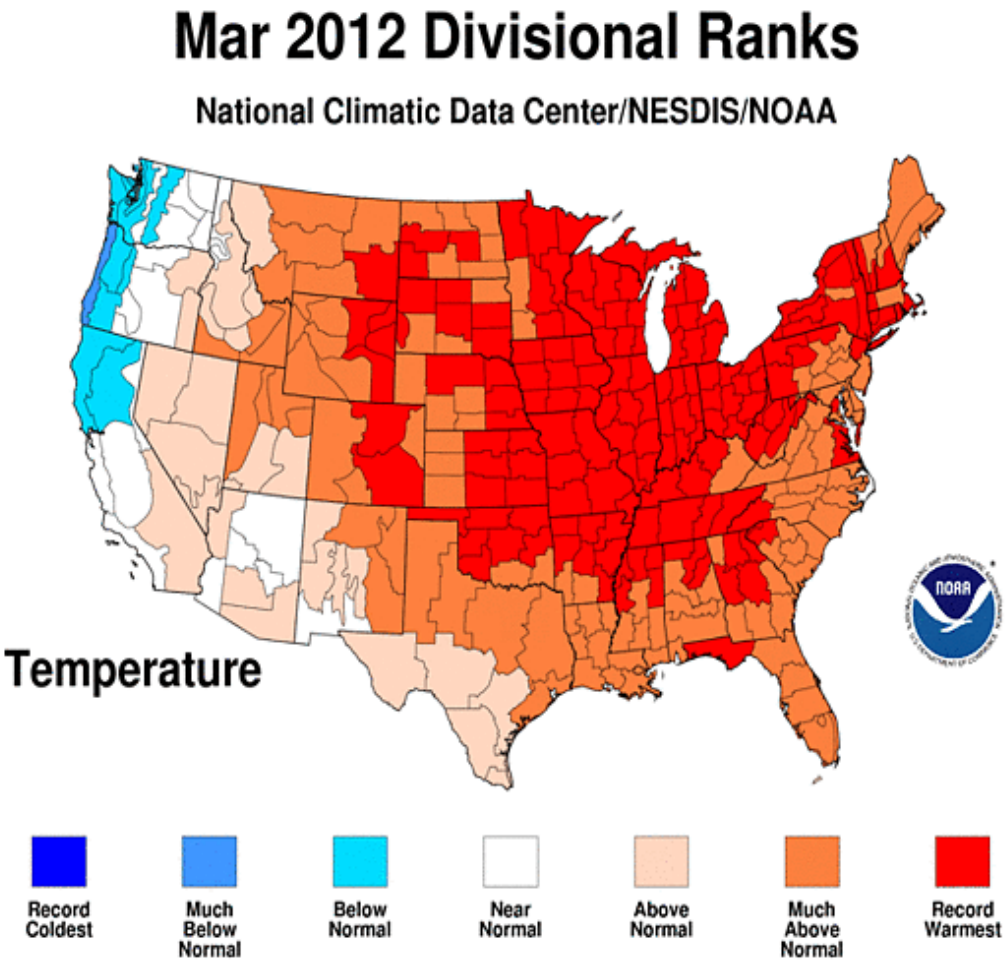

Figure 2.4. Example of the climate ranking maps provided by NCDC.

2.2 Heat Budget

Hydrodynamic processes within the Great Lakes are complex and are thoroughly described by Boyce (1974), Mortimer (2004), and others. The thermal structure and subsequent heat, or energy, budget for the Great Lakes can be sufficiently summarized through the following expression:

$$Q_{NET} = Q_{SW} - Q_{SW\uparrow} + Q_{LW} - Q_{LW\uparrow} - Q_E - Q_H - Q_{ADV} \qquad (1)$$

where Q_{SW} is the solar radiation (shortwave) incident upon the surface waters, $Q_{SW\uparrow}$ is the solar radiation (shortwave) reflected at the surface waters, Q_{LW} is the longwave radiation incident upon the surface waters from the overlying atmosphere, $Q_{LW\uparrow}$ is the longwave radiation emitted by the water body to the overlying atmosphere, Q_E is the latent heat loss,

or heat loss due to the evaporation of water, Q_H is the sensible heat loss (or gain) from the heat flux across the air-water interface, Q_{ADV} is the total heat loss (or gain) from waters directly entering the water body (i.e. inflow from rivers, groundwater, precipitation and outflow from the water body), and Q_{NET} is the total heat lost (or gained) during the observed period.

The solar radiation incident upon the surface waters varies spatially and temporally (diurnal and seasonal), depending on the type of clouds and the total cloud cover (spatial and temporal-diurnal), as well as the time of year (temporal-seasonal) and the time of day (temporal-diurnal). Shortwave radiation was determined using data collected by the pyranometer atop the Lufft sensor on the buoy. While not necessarily representative of the entire bay, it was assumed for this study that solar irradiance, and thus cloud cover, was homogenous across the southern bay (the area of interest for this study).

The reflected solar radiation was determined by the expression:

$$Q_{SW\uparrow} = \alpha Q_{SW} \qquad (2)$$

where $Q_{SW\uparrow}$ is the reflected solar radiation, α is the albedo, and Q_{SW} is the incident solar radiation obtained from the Lufft sensor on the buoy. A value of 0.08 determined by Schertzer (1978; 1987) for open water conditions on Lake Superior and Lake Erie was used for α.

Cloud cover determines the amount of longwave radiation received by the surface waters from the overlying atmosphere. The complexity of these processes is illuminated when considering the dynamics between shortwave and longwave radiation. Shortwave radiation, in effect, dictates the longwave radiation emitted by the water body, as the temperature of the water dictates the amount of longwave radiation emitted by the water body. Solar irradiance is the primary mode of heating of the surface waters and, in combination with wind speed, is the primary mode of cooling of surface waters (via latent

heat loss). However, warmer air (and a higher content of moisture therein) increases the incident longwave radiation (Lofgren and Zhu 2000). The result is typically no net effect on the energy budget between the competing processes of incoming and outgoing longwave radiation (Verburg and Antenucci 2010).

Incident longwave radiation is a function of the vapor pressure of the air, air temperature, and cloud cover. Under cloudless, or clear-sky, conditions, the incident longwave radiation was determined using the equation:

$$Q_{LW\text{-}CL} = \varepsilon_{cl}\sigma T_a^4 \quad (3)$$

where ε_{cl} is the emissivity of the atmosphere under clear-sky conditions, σ is the Stefan-Boltzmann constant (σ=5.67 x 10^{-8} W m^{-2} K^{-4}), and T_a is the near-surface air temperature (in Kelvin).

The ε_{cl} is determined using an equation from Brutsaert (1982):

$$\varepsilon_{cl} = 1.24\left(\frac{e_a}{T_a}\right)^{1/7} \quad (4)$$

where e_a is the vapor pressure of air. It should be noted that a value of 0.643, rather than the constant above of 1.24, provided by Kruk et al. (2010) was used initially. However, this constant resulted in unrealistic incoming longwave radiation estimates. Thus, Brutsaert's constant, and equation, were used.

Incident longwave radiation under cloud cover, and particularly all-sky conditions, relies upon a parameterization that is less certain than the aforementioned equations. While many parameterizations have been offered for different regions, parameterizations that use a cloud fraction term which is then multiplied by the clear-sky longwave radiation value are preferred. While a significant amount of research was done on the physical limnology of the Great Lakes in the 1950's to 1990's, more recent, enhanced parameterizations for large lakes are only available for sensible and latent heat terms, to the author's knowledge. Longwave parameterization enhancements, while improving for terrestrial situations and

despite the high cost of longwave measuring instruments (pyrgeometers), have not been performed for the Great Lakes region (discounting satellite data which is insufficient for this study due to the frequency of data). While the parameterizations presented by Duarte et al. (2006) and supported by Kruk et al. (2010) are specific to terrestrial systems in southern Brazil and the constant provided by Kruk et al. (2010) was inaccurate for clear-sky longwave parameterizations, this parameterization primarily accounts for the constant present with cloud cover. Due to the in-depth analyses associated with the equations, the equation was deemed superior to previous parameterizations. Thus, the following expression from Duarte et al. (2006) was used:

$$Q_{LW-AS} = Q_{lw-cl}(1 + 0.242c^{0.583}) \qquad (5)$$

where c is the fraction of cloud cover from 0.05 to 1. Cloud fractions were determined using methods similar to those found in Crawford and Duchon (1999) and Duarte et al. (2006):

$$c = 1 - \frac{Q_{sw\ obs}}{Q_{sw\ max}} \qquad (6)$$

where $Q_{SW\ OBS}$ is the observed value of irradiance and $Q_{SW\ MAX}$ is the maximum observed value of irradiance for the time period. This analysis differed from previous analyses by breaking down observations into one hour segments (for which two irradiance measurements were made), with maximum observed values for each hour being used as the denominator. These values were further broken down by a running maximum that considered values two weeks prior and two weeks after the observation to prevent the bias of changing seasonal solar values from significantly affecting the analysis. Hour periods for which sunrise/sunset were observed within were removed from subsequent months (e.g. the 6:00 hour was present in July analyses but not August, September, or October analyses). Sunrise/sunset times were based on observations (consistent 0 $W \cdot m^{-2}$ values). Maximum observed irradiance values were used as opposed to theoretical irradiance values due to the fair certainty that clear sky conditions were observed at least once per four week period per

hour period (an assumption that is somewhat, but not entirely, verified by the data) and in an attempt to reduce parameterizations to the extent possible.

One issue with the above method for determining cloud cover is that only daytime values for irradiance are measured, and thus nighttime cloud cover cannot be determined. Others have used a linear relationship between the last observed cloud cover in the evening and the first cloud cover observation from the subsequent morning (Sridhar and Elliott 2002; Duarte et al. 2006). However, this method carries with it considerable uncertainty, and the Austin-Straubel International Airport meteorological station, located approximately 50 kilometers from the buoy, collected fractional cloud cover data. These cloud cover values were used when data from the buoy was missing (primarily overnight values). However, it did not supersede calculated cloud cover from irradiance data, as the cloud cover was only precise to five cloud fractions – 0, 0.125, 0.45, 0.75, 1.0 – indicated by three-character strings (CLR, FEW, SCT, BKN, OVC, respectively) and rough averages of those values where more than one value was observed per hour (e.g. a listing of FEW, BKN, OVC). Three-digit numeric strings were attached to each character string, indicating the cloud base height (in feet, from the terrestrial surface); however, only cloud cover was considered for the longwave radiation calculation.

While some have ignored cloud fractions below 0.3 and labeled them as clear-sky (Reed 1976; Beardsley et al. 1998), the author followed protocol by Kruk et al. (2010) and used a fraction of 0.05 as the threshold value for clear-sky conditions. This agrees with the supplementary cloud data provided by NCDC, as the first cloud term, FEW, corresponds to 0/8-2/8 (average of 0.125) of the sky being covered in clouds. Under the 0.3 threshold, these cloud values would be wrongly assumed to be clear sky.

The latent and sensible heat flux, Q_E and Q_H, respectively, were calculated using the measured variables air temperature (T_a, ˚C), water surface temperature (T_s, ˚C), relative

humidity (RH, %), wind speed (U_z, m s^{-1}), and air pressure (P, hPa) and the bulk aerodynamic methods from Verburg and Antenucci (2010):

$$Q_E = p_a L_v C_E U_z (q_s - q_z) \quad (7)$$

$$Q_H = p_a C_a C_H U_z (T_s - T_a) \quad (8)$$

where C_E and C_H are the transfer coefficients for latent and sensible heat, respectively, C_a is the specific heat of air (1005 J kg^{-1} K^{-1}) and

$$p_a = \frac{100P}{R_a(T_a+273.16)} \quad \text{air density, kg } m^{-3} \quad (9)$$

$$R_a = 287(1 + 0.608q_z) \quad \text{gas constant for moist air, J kg } K^{-1} \quad (10)$$

$$L_V = 2.501 \times 10^6 - 2370T_s \quad \text{latent heat of vaporization, J } kg^{-1} \quad (11)$$

$$q_s = \frac{0.622e_{sat}}{P} \quad \text{specific humidity at saturation, kg } kg^{-1} \quad (12)$$

$$q_z = \frac{0.622e_a}{P} \quad \text{specific humidity, kg } kg^{-1} \quad (13)$$

$$e_{sat} = 6.11\, exp^{\left[\frac{17.27T_s}{(237.3+T_s)}\right]} \quad \text{saturated vapor pressure at } T_s\text{, hPa} \quad (14)$$

$$e_a = \frac{RHe_s}{100} \quad \text{vapor pressure, hPa} \quad (15)$$

$$e_s = 6.11\, exp^{\left[\frac{17.27T_a}{(237.3+T_a)}\right]} \quad \text{saturated vapor pressure at } T_a\text{, hPa} \quad (16)$$

Total evaporation (E*) from the surface waters to the overlying atmosphere during the observed period can be estimated as

$$E^* = \frac{Q_E}{p_w L_V}, \text{ m } s^{-1} \quad (17)$$

Water density (p_w , in kg m^{-3}) is given by Henderson-Sellers (1986)

$$p_w = 10^3 \times [1 - 1.9549 \times 10^{-5}|T_s - 3.84|^{1.68}] \quad (18)$$

The transfer coefficients for latent and sensible heat were assumed to be the same (Zeng et al. 1998). While the ideal method for determining the bulk aerodynamic transfer coefficient is to measure the necessary variables at two heights and to then parameterize the turbulent flux from this data, the buoy used only had one meteorological station at a

1.5m height above the water surface. There are several methods to determine the value of the transfer coefficient without calculating turbulent flux directly. Verburg and Antenucci (2010) offer a method that involves multiple iterations, starting with values for air shear velocity and roughness lengths (momentum and vapor) under neutral conditions. The Matlab code written by Verburg and Antenucci (2010) and used in their analyses of latent and sensible heat fluxes over Lake Tanganyika was translated into the program R and run with the appropriate input data (Appendix B).

Advection terms for each station were calculated based upon the net heat flux calculated for Station 17. Advection was calculated using the equation

$$Q_{adv} = Q_{NET} - d\theta$$

where Q_{adv} is the advection term and $d\theta$ is the change in temperature of the water column. The mean temperature of the water column for a given day was calculated using the mean water temperature of the water column at each sample point between all functioning thermistors at the site. This value was then converted into $W \cdot m^{-2}$ by multiplying the heat storage term, θ, by the specific heat of water, the density of water, the depth of the site, and the number of seconds in a day. $d\theta$ was then calculated using the equation

$$d\theta = \theta_2 - \theta_1$$

where θ_2 is the daily heat storage term ($W \cdot m^{-2}$) subsequent to θ_1. Due to sign conventions when calculating the net flux, $d\theta$ is assigned a negative value in the equation for calculating advection.

2.3 Light Extinction

Light extinction (or attenuation) coefficients (k_d) were determined from monthly profiles using a HOBO pendant. Profiles were conducted at various sites from July through September throughout the bay, with 4 common sites for each month and a maximum of 17

sites and a minimum of 10 sites in one month (August and September, respectively). K_d values are calculated using the general equation

$$I_z = I_o exp^{-k_d z} \quad (19)$$

where z is the depth, I_z is the observed irradiance at depth, I_o is the surface observed irradiance, and k_d is the light extinction coefficient. With this general equation in mind, k_d values were determined by plotting the depth versus the natural log (ln) of the irradiance values. The negative slope of the linear regression of the plotted data is the value of k_d for that particular site.

Processing the profile data was relatively complex when considering: 1) the HOBO pendants are not equipped with depth sensors and 2) considering the response of the HOBO pendants to light levels. The HOBO pendants were lowered with an YSI 6600 series multi-parameter sonde, at an exact height of 0.47m above the depth sensor of the sonde. The internal times of each instrument were calibrated using the same laptop, with an expected accuracy of <2 seconds (the coined "click-time uncertainty"). This expected accuracy corresponded well with the first irradiance reading by the HOBO pendant across data sets. Irradiance values were recorded every one second during the profile by the HOBO pendant, and depth (and other parameter) values were recorded every two seconds by the sonde. The HOBO pendant data were fitted with corresponding and interpolated depth values from the sonde using a custom script in the program R (Appendix C). Near-surface values were considered for the calculation of k_d.

When considering HOBO pendant response to light levels, it was acknowledged that the peak response by the instrument occurred within the light range that is expected to extinguish the fastest in surface waters (red and near infrared, 600-1000nm) (Kirk 1994; Effler et al. 2010). When analyzing the irradiance profiles, it was noted that many with relatively uniform data reflected a steeper slope (LEC) in the first 1-2m than for the rest of

the profile. This could be considered as a more turbid surface layer, likely due to algal biomass, as turbid waters attenuate greater in the range for which the sensor is less sensitive. However, considering the response of the sensor to light levels, the strength of this trend, and the inaccuracies associated with it, there was uncertainty that this was an artifact of the HOBO pendant response to light levels, and not an observation of increased turbidity in surface waters. Once below this surface layer, however, the k_d value is expected to be accurate, as the HOBO pendant responses are much more consistent beyond the surface region across profiles and the light which the sensor is most sensitive to is significantly diminished past 1-3m and rapidly extinguished thereafter (Kirk 1994).

By determining k_d, an optical depth can be determined for the water column. Typically, optical depths of 10 and 1% of surface irradiance are of interest. An optical depth of 10% corresponds to the mid-point of the photic zone and an optical depth of 1% corresponds to the depth at which light becomes limiting for photosynthesis (photic depth). Optical depth is calculated by

$$\zeta = k_d z \tag{21}$$

where ζ is the optical depth and z is the depth of interest. To determine the depth at which ζ is equal to 10 % and 1%, ζ is set equal to 2.3 and 4.6, respectively (Kirk 1994).

When the optical depth for 1% is calculated, the volume of water within which phytoplankton can photosynthesize at a particular point in the bay can be calculated. The amount of energy required to fix one molecule of carbon into one molecule of carbohydrate can be calculated, using the chemical reaction

$$CO_2 + 2\,H_2O \xrightarrow{\sim 8hv} (CH_2O) + H_2O + O_2 \qquad \text{(Kirk 1994)} \tag{22}$$

if the frequency of light is known. The expression

$$E = hv \tag{23}$$

where E is energy (Joules), h is Planck's constant (6.63 x 10^{-34} J s^{-1}), and *v* is the frequency of the monochromatic light when converting between energy and frequency accounts for the frequency of light when considering the energetics of a monochromatic wavelength. Monochromatic light data were not available, but the spectral range, in wavelength, is known. Using the equation

$$E = \frac{hc}{\lambda} \tag{24}$$

where c is the speed of light constant (3 x 10^{8} m s^{-1}) and λ is the wavelength of light (converted from nm to m), the energy used to photosynthesize one molecule of carbon can be calculated using the wavelength of light. The average wavelength of light used by phytoplankton can be approximated by taking the mid-point of the spectral range, 400-700nm, or the average between the two spectral peaks within chlorophyll-a, 430nm and 670nm, both of which result in a value of 550nm. While chlorophyll-a does not absorb consistently between these two peaks, this is a rough method. When using a wavelength of 550nm, the equation to calculate energy use for photosynthesis is

$$E = \frac{8hc}{\lambda} \tag{25}$$

where 8 is the approximate multiplier when using Equation (22) from Kirk (1994). Using this value over the photic depth allows for a rough calculation of the amount of light energy within the water column that is converted to biochemical, rather than heat, energy by following the procedure outlined in Appendix D. While different algal groups display varying degrees of photosynthetic efficiencies depending on the environment and physiological characteristics, the method was deemed adequate for a rough estimate of the algal energetic "sink" within the context of a heat budget.

2.4 Short Term Analyses and Diel Warming Trends

Periods of several days to a few weeks were plotted to look more closely at trends. Thermal profile data were visually observed and compared to meteorological forcing

variables and flux terms over the same period to better account for the behavior observed within the water column. Bottom water temperatures were plotted for specific periods over the season, determined by looking at a season long plot of bottom temperatures, to better understand the behavior of cold water intrusions in the lower bay and to look for a consistent pathway in this distinct water mass.

Additionally, to determine the effect of water clarity on radiant heat absorption by the water column, the difference between the maximum and minimum surface temperature was calculated for applicable stations over the study period. These values were also compared to meteorological forcing variables and flux terms over specific periods in an attempt to determine the cause of particular trends. Sub-surface values were also considered using the HOBO logger at the sub-surface float, typically 3-4 meters below the surface of the water. A similar process as described for the surface temperature data was used on this data set.

Finally, bottom water temperatures were tracked across moorings to determine the pathway of cold water intrusions into southern Green Bay. Minimum temperatures at each station as well as the time at which stations encountered the same cool temperature (treated as the warmest minimum temperature across stations) were used to determine the pathway of the cool water masses.

Chapter 3: Results

3.1 Mooring & Buoy Temperature Profiles

Contour plots of temperature over depth and time were plotted using Surfer 9 (Fig. 3.1a-j). The Kriging method was used for interpolation with approximately 30-minute spacing used for the horizontal axis and 0.5m spacing used for the vertical axis, except Chambers Island West which utilized 0.25m spacing due to a smaller set of data (Fig. 3.1j). Intrusions of cold water from northern Green Bay, and presumably Lake Michigan proper, were evident in all temperature profile plots throughout the study period (Fig. 3.1a-j). For shallow, southerly sites, these intrusions represented the only periods of defined thermocline formation for the entire summer (Fig. 3.1a-f). As sites became deeper and displayed season-long, semi-stable thermoclines, such as Station 31 (Fig. 3.1i), intrusions resulted in a thicker hypolimnetic layer for much of the study period. Large thermocline oscillations at sites with stable thermoclines were temporally correlated with cold-water intrusions into shallow southerly sites when visually inspecting the data. Surface waters remained near 25˚C (or warmer) until Julian day 220 (August 7), at which point surface waters began to gradually cool. Full water column mixing, resulting in isothermal conditions, began at all sites (excluding Station 13-19, depth=7.7m) from Julian days 260-270 (September 26), with 15˚C isothermal conditions occurring at all sites on Julian day 279. Specific periods throughout the summer are examined in more detail for select sites in Section 3.6.

To better determine how 2012 thermal profiles compare to previous years, data from Station 9 were compared between years 2011 and 2012. When considering data from the NCDC, divisional climate ranks were determined for three of the four divisions that share coastline with Green Bay (the fourth division in the Upper Peninsula of Michigan was not considered as it shares only a small amount of coastline with Green Bay and is west of

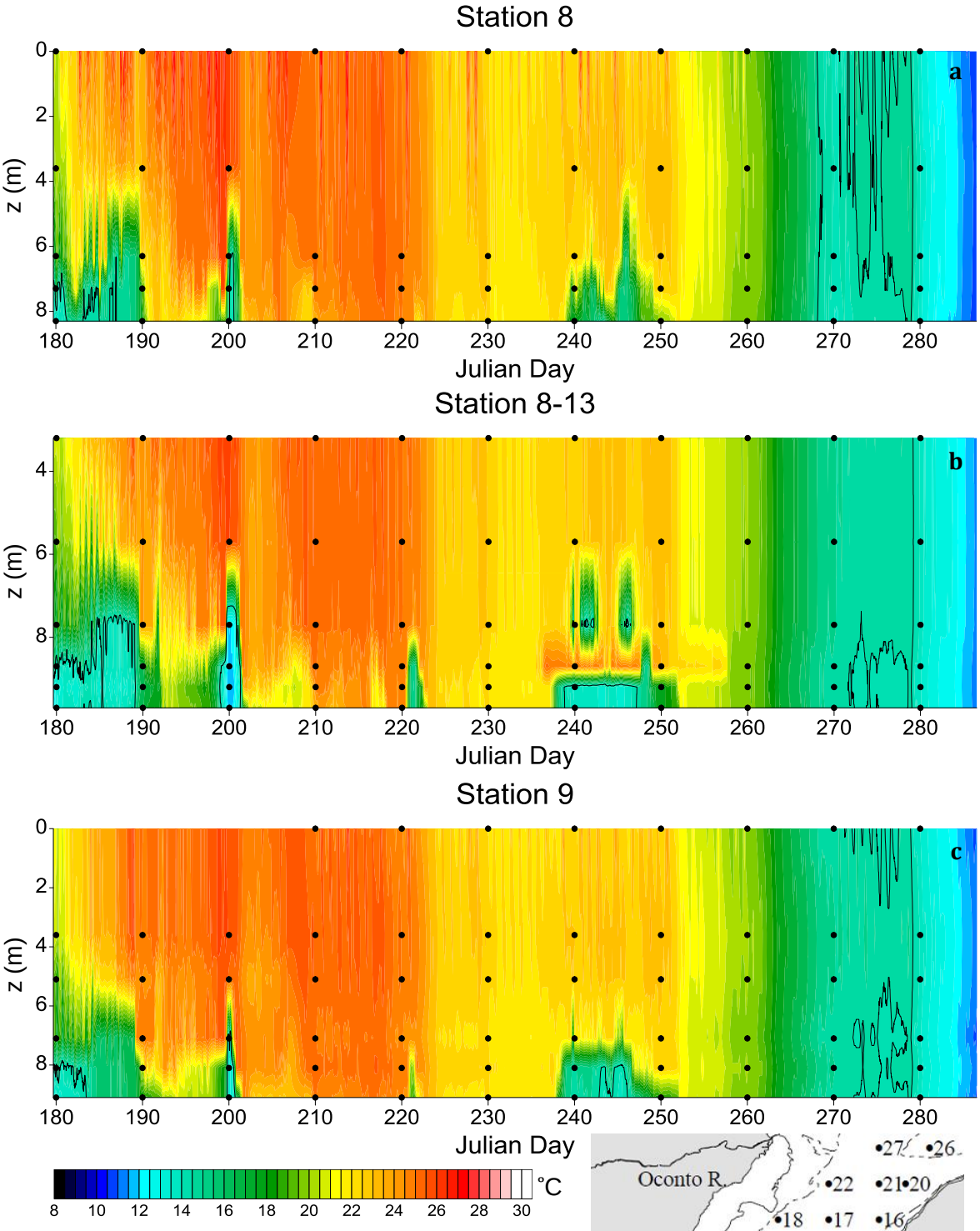

Figure 3.1a-c. Horizontal axis is Julian day, vertical axis is depth in meters, with 0 equal to the surface. Depth for each site is a season average. Color contours are based on the color legend, with temperatures in ˚C. The 15˚C isotherm is marked as the black line. a) Station 8, depth =8.3m b) Station 8-13, depth = 9.7m c) Station 9, depth = 9.1m

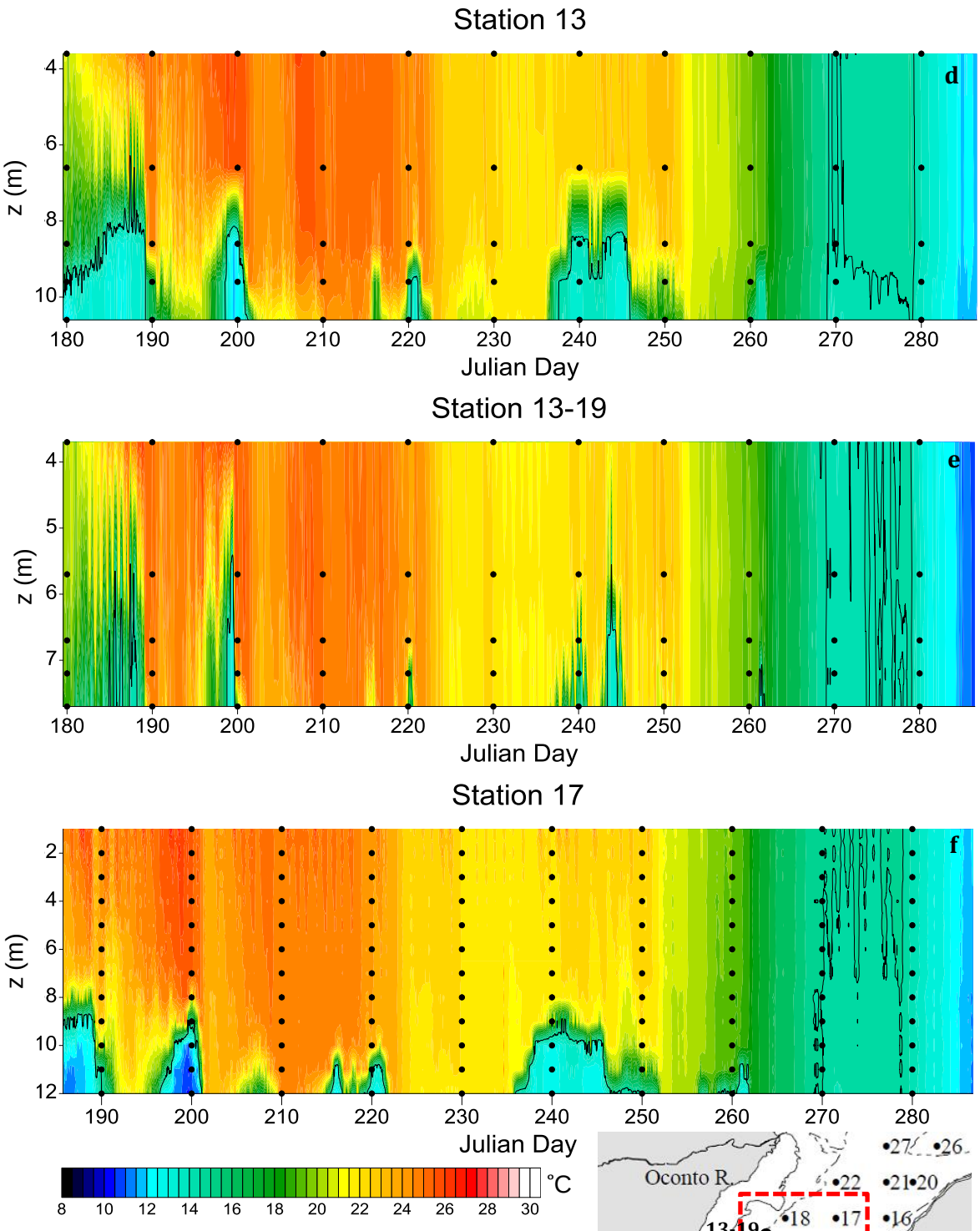

Figure 3.1d-f. Horizontal axis is Julian day, vertical axis is depth in meters, with 0 equal to the surface. Depth for each site is a season average. Color contours are based on the color legend, with temperatures in ˚C. The 15˚C isotherm is marked as the black line. d) Station 13, depth =10.6m e) Station 13-19, depth = 7.7m f) Station 17, depth = 13m

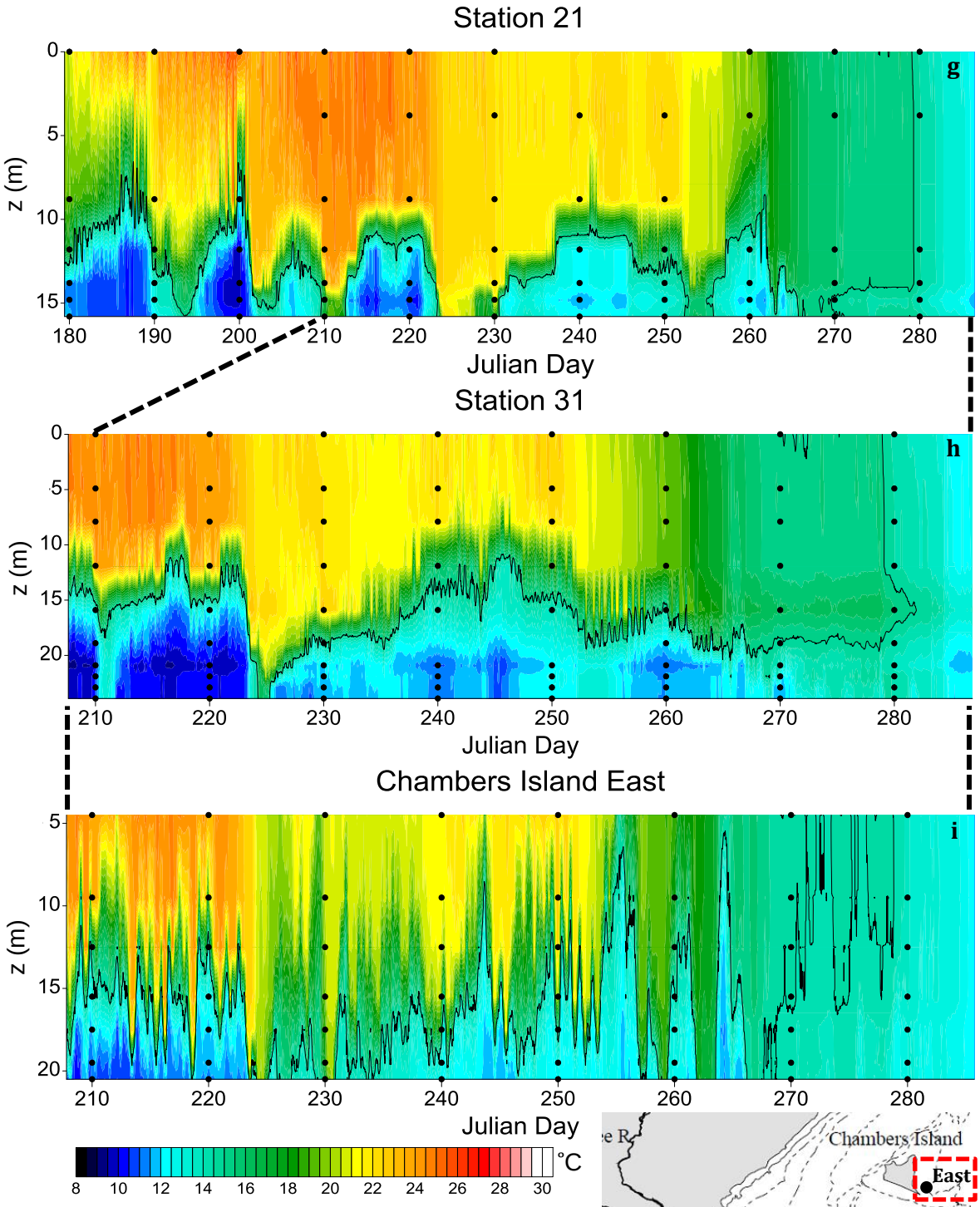

Figure 3.1g-i. Horizontal axis is Julian day, vertical axis is depth in meters, with 0 equal to the surface. Depth for each site is a season average. Color contours are based on the color legend, with temperatures in ˚C. The 15˚C isotherm is marked as the black line. g) Station 21, depth =15.8m h) Station 31, depth = 23.9m i) Chambers Island East, depth = 20.5m

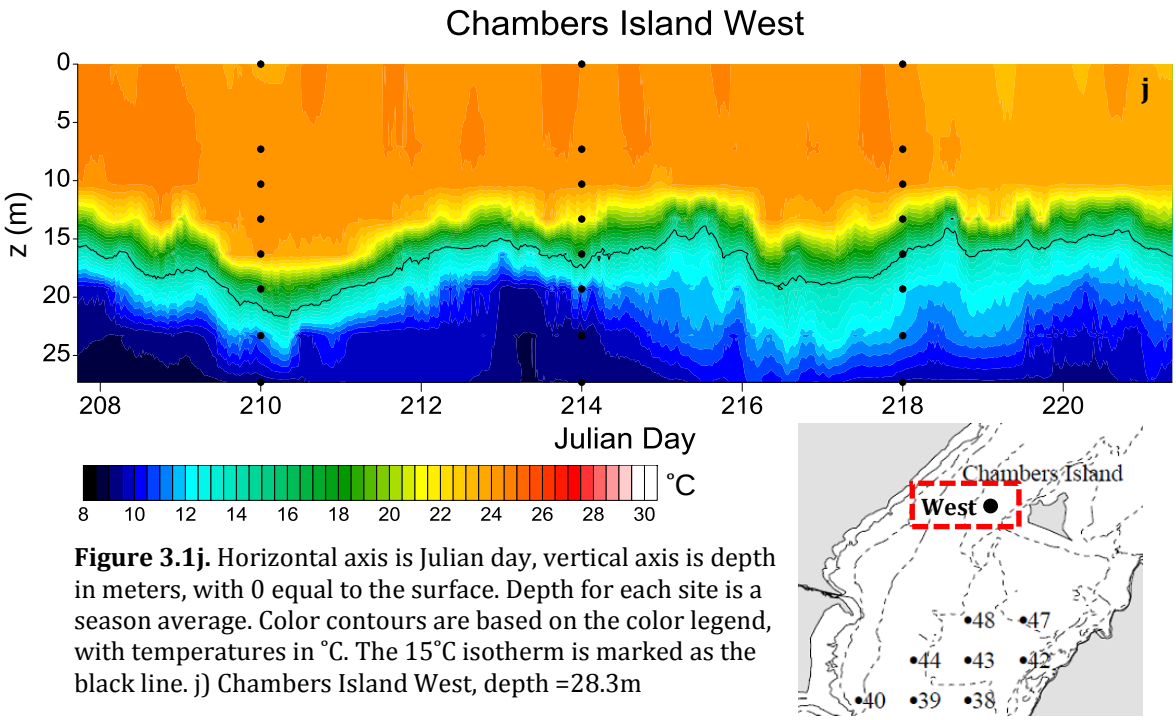

Figure 3.1j. Horizontal axis is Julian day, vertical axis is depth in meters, with 0 equal to the surface. Depth for each site is a season average. Color contours are based on the color legend, with temperatures in ˚C. The 15˚C isotherm is marked as the black line. j) Chambers Island West, depth =28.3m

the majority of the bay). Ranks for the spring and summer periods of these two years indicated that 2012 had a much warmer spring and that 2011 displayed a warmer summer overall, with 2012 exhibiting a warmer July (Table 3.1).

Table 3.1. Summary of monthly climate rankings, taken as an average of monthly rankings from each of three divisions sharing coastline with Green Bay.

Year	March	April	May	June	Spring Avg.	July	August	Summer Avg.	September
2011	0.50	0.35	0.31	0.31	0.40	**0.91**	0.74	0.82	0.37
2012	**1**	0.65	0.88	0.86	0.80	**0.96**	0.55	0.75	0.29

While data for 2012 did not begin until the end of June, comparing the two years indicates that 2012 was slightly advanced in its warming in comparison by an estimated 5-10 days (Fig. 3.2). More significantly, the water column at Station 9 in 2012 maintained warmer temperatures into the fall, reaching similar isothermal conditions approximately two weeks later than in 2011. This is likely due to the warmer overall temperatures throughout the summer and the enhanced entrapment of heat throughout the water column which had remained well-mixed throughout the summer of 2012, which also contrasts the

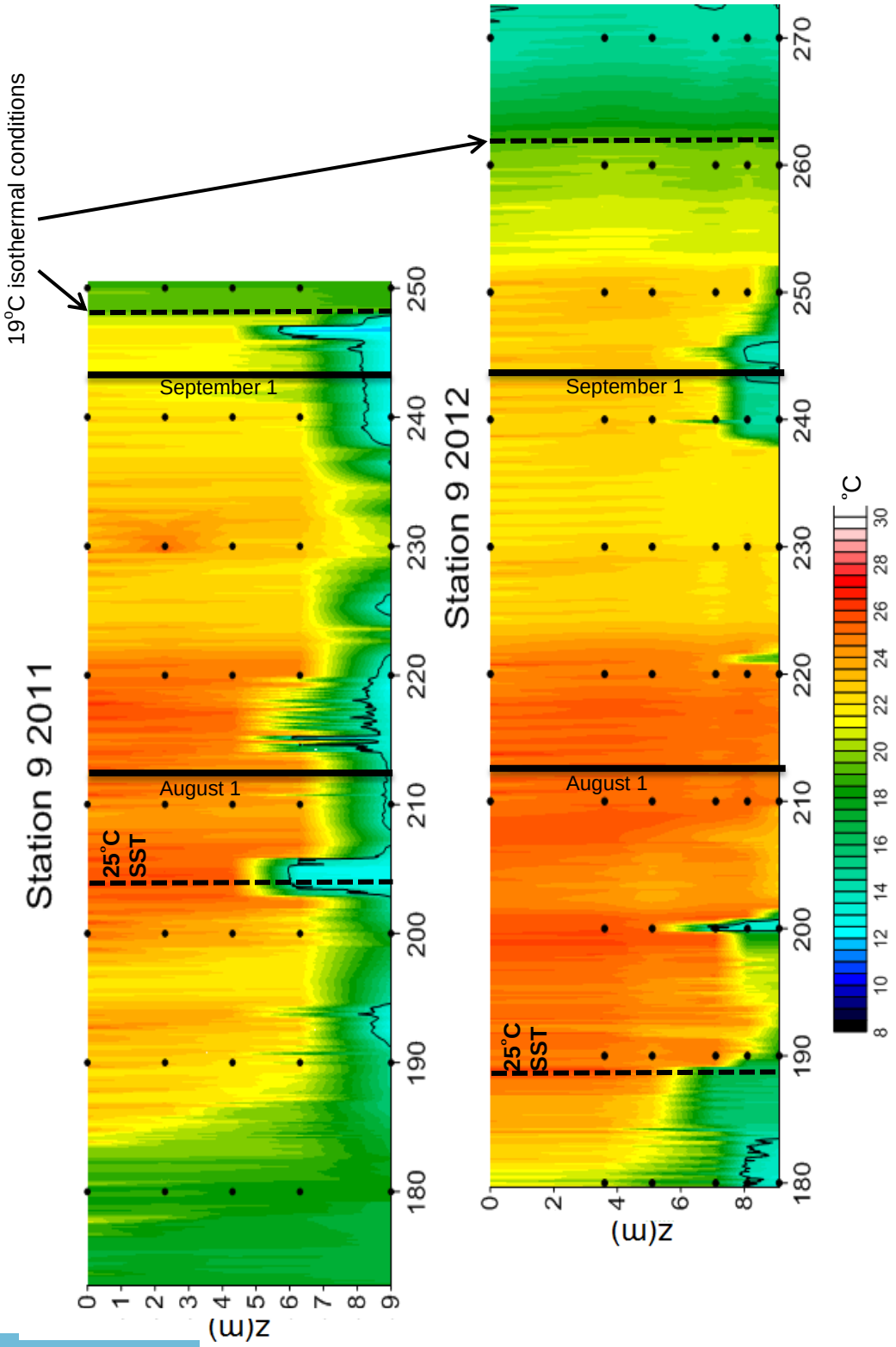

Figure 3.2. Interannual comparison of temperature plots for Station 9

2011 season where cooler waters were observed for much of the study period. These findings agree well with the findings in the THERMOS experiment conducted in Lake Breisjøen, southern Norway (Lydersen et al. 2008).

3.2 Heat Flux

The overall heat flux was calculated as daily averages from the sum of total shortwave and longwave radiation inputs and outputs and the sensible and latent flux terms (Fig. 3.3). Advection through precipitation was considered non-influential, especially considering the abnormally dry summer experienced over much of the bay in 2012. Thus, the advection term was considered as representing the movement of thermally distinct water masses within the bay. This assumption was supported by correlated trends between the arrival of cold water masses across the sites and a strongly negative advection term within the same period (Fig. 3.4a-i).

As expected, net shortwave radiation (the sum of irradiance and reflectance, with irradiance being positive and reflectance being negative) was always positive, with a high of approximately 700 $W \cdot m^{-2} day^{-1}$, but more typically fluctuating around 200 $W \cdot m^{-2} day^{-1}$. Net longwave radiation (the sum of atmospheric inputs considering cloud cover and emissions by water, assuming an emissivity of 0.97) was essentially zero throughout the season, with fluctuations of ±25 $W \cdot m^{-2} day^{-1}$ common, primarily due to cloud cover. Sensible heat flux was small throughout the study period, fluctuating between positive and negative values that rarely exceeded ±100 $W \cdot m^{-2} day^{-1}$. Latent heat flux was negative for nearly all of the study period with peak values approaching -400 $W \cdot m^{-2} day^{-1}$. Net heat flux was typically positive until the end of August, when it became primarily negative. There were many periods of fluctuating values, primarily due to variance in incoming shortwave radiation, varying rates of evaporation, and unstable water column temperatures due to the large advection terms. The advection of distinct water masses throughout the bay resulted in occasional

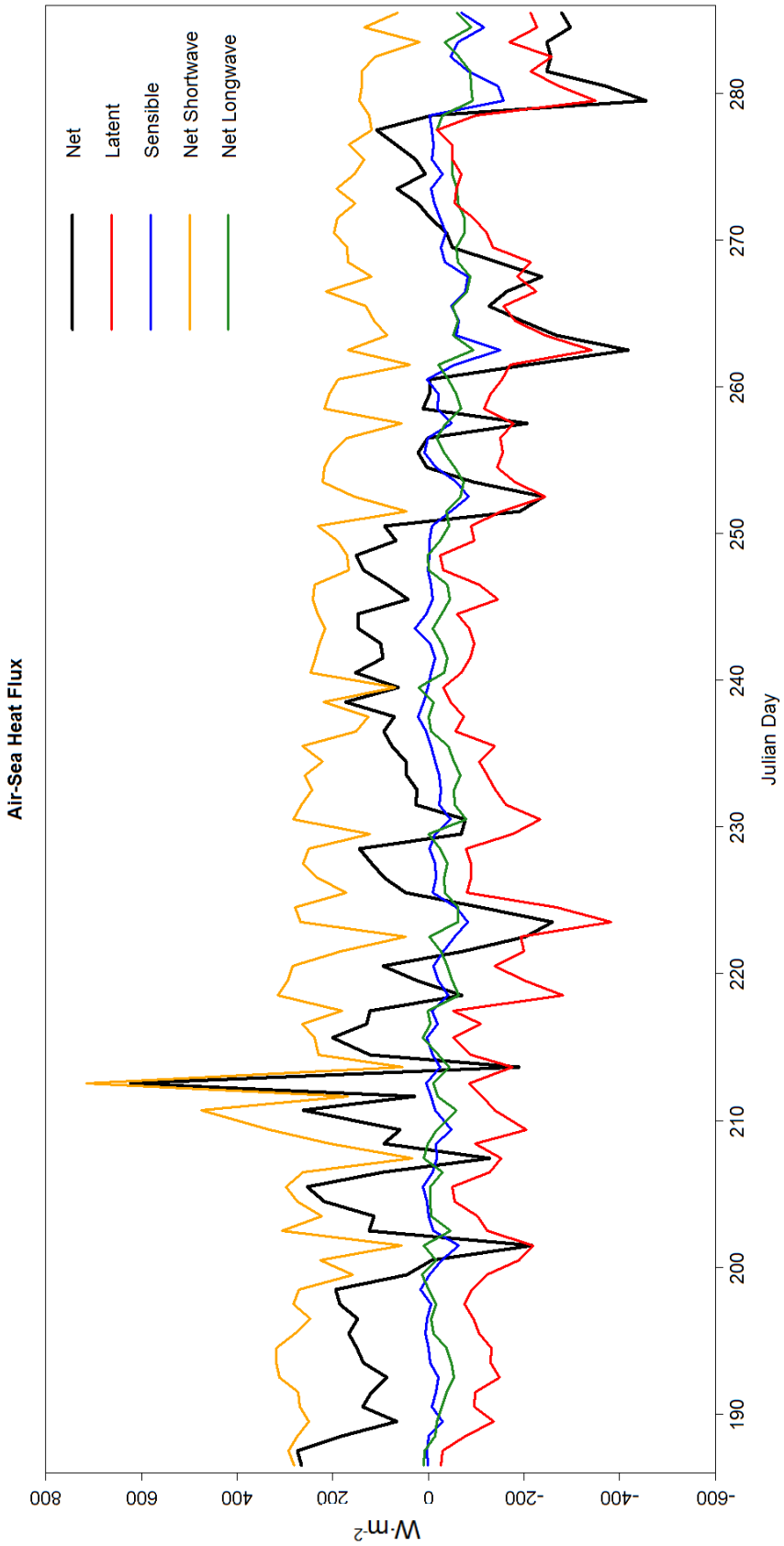

Figure 3.3. Air-sea heat flux for Green Bay over the study period, relevant for the region south of Chambers Island. Values are daily averages (e.g. 200 $W \cdot m^{-2}$ of shortwave flux indicates a constant contribution of that quantity over the 24 hour period).

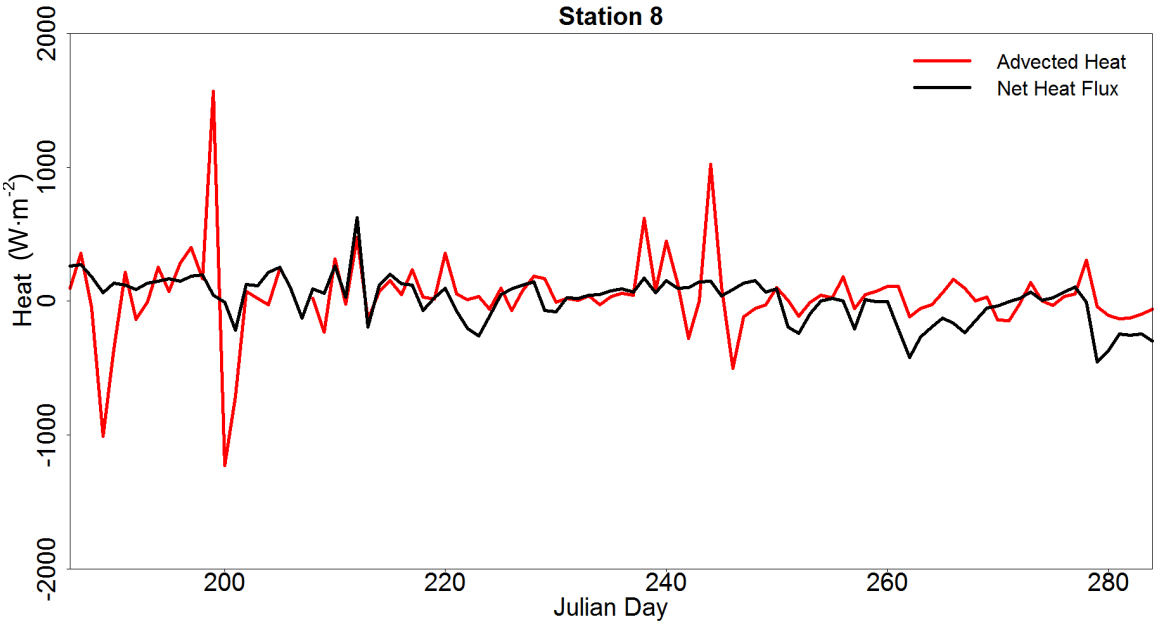

Figure 3.4a. Daily average advected heat for Station 8 (red) and net air-sea heat flux (daily average) calculated for Station 17 (black).

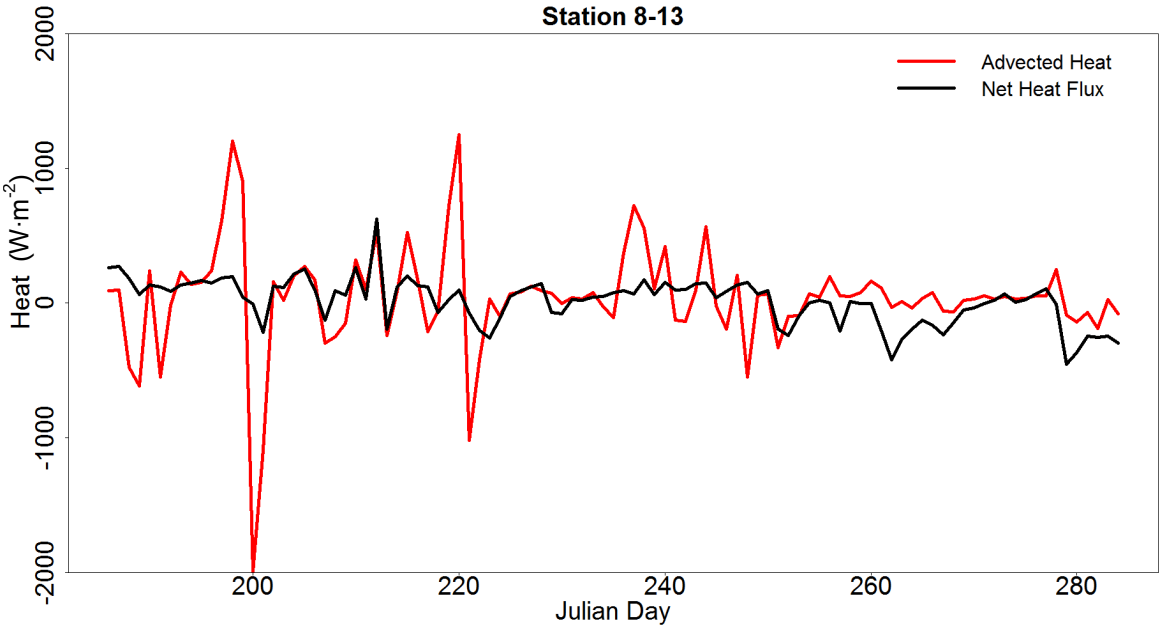

Figure 3.4b. Daily average advected heat for Station 8-13 (red) and net air-sea heat flux (daily average) calculated for Station 17 (black).

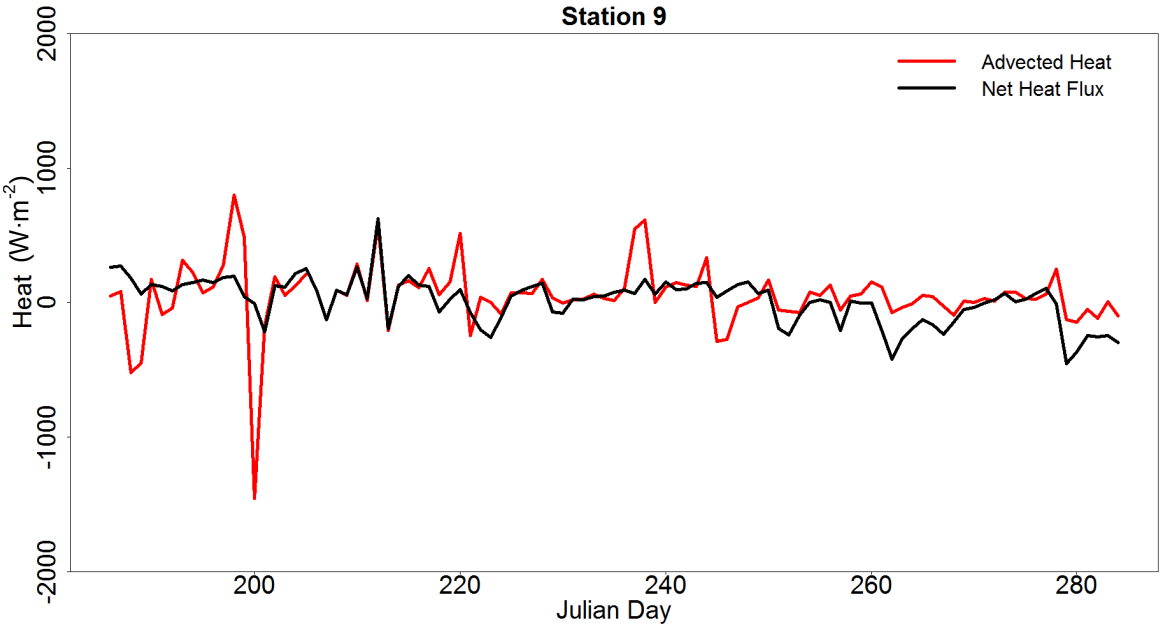

Figure 3.4c. Daily average advected heat for Station 9 (red) and net air-sea heat flux (daily average) calculated for Station 17 (black).

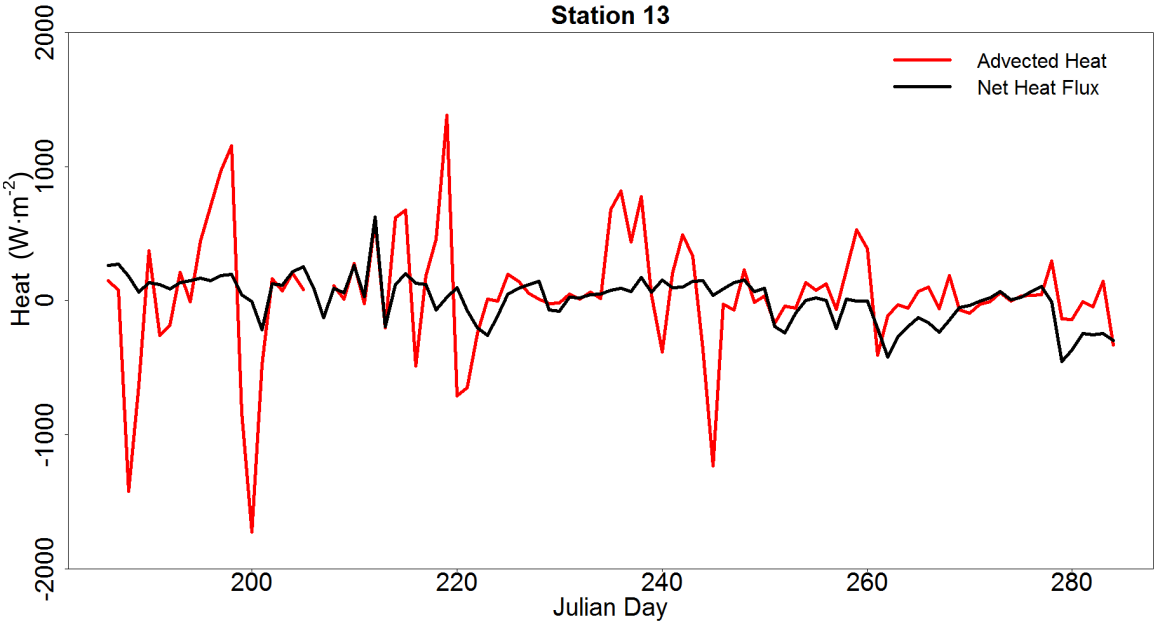

Figure 3.4d. Daily average advected heat for Station 13 (red) and net air-sea heat flux (daily average) calculated for Station 17 (black).

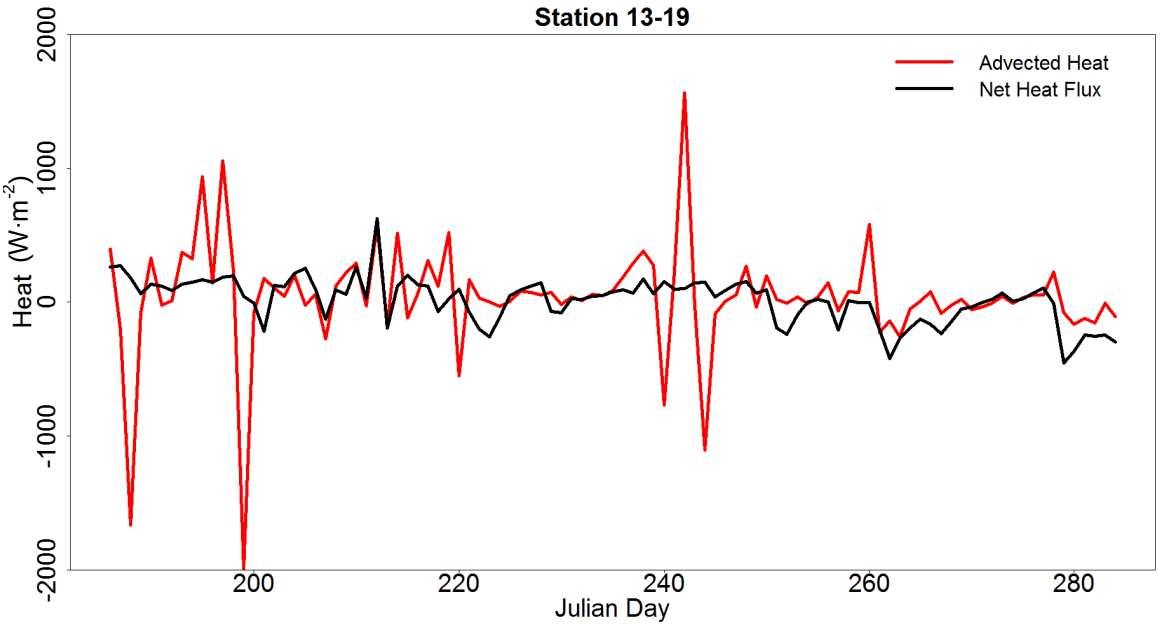

Figure 3.4e. Daily average advected heat for Station 13-19 (red) and net air-sea heat flux (daily average) calculated for Station 17 (black).

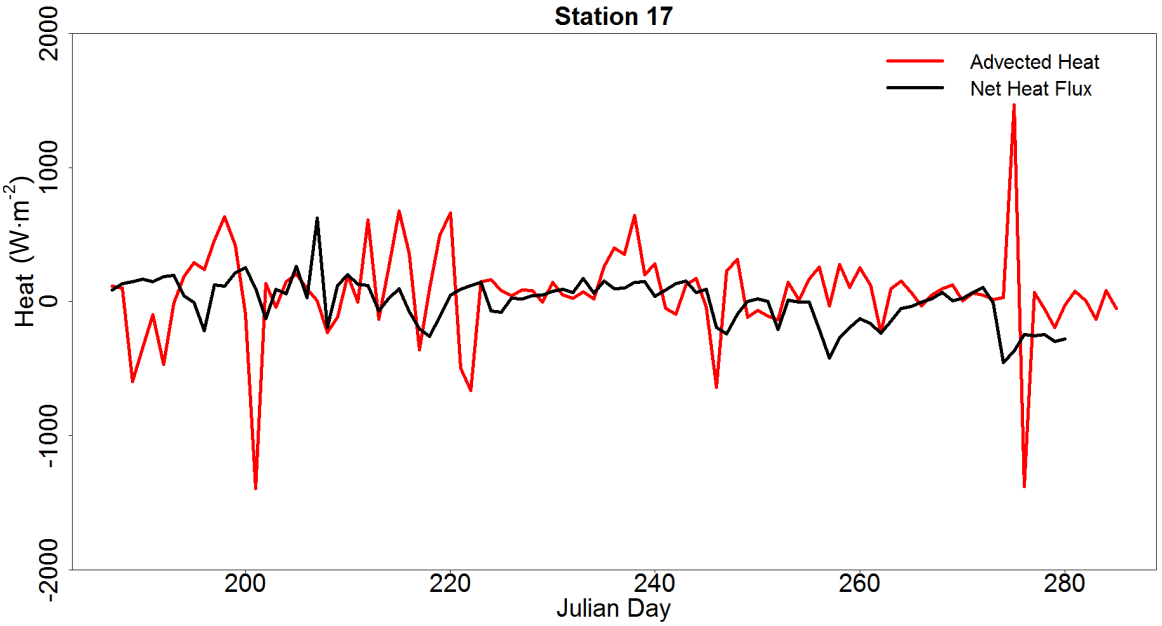

Figure 3.4f. Daily average advected heat for Station 17 (red) and net air-sea heat flux (daily average) calculated for Station 17 (black).

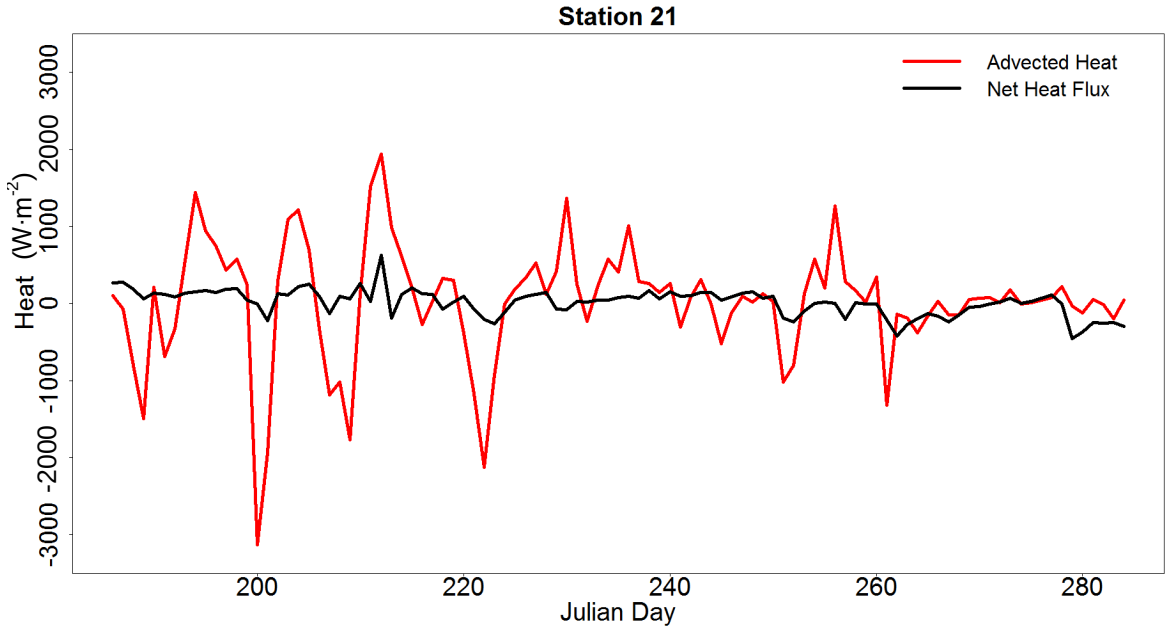

Figure 3.4g. Daily average advected heat for Station 21 (red) and net air-sea heat flux (daily average) calculated for Station 17 (black).

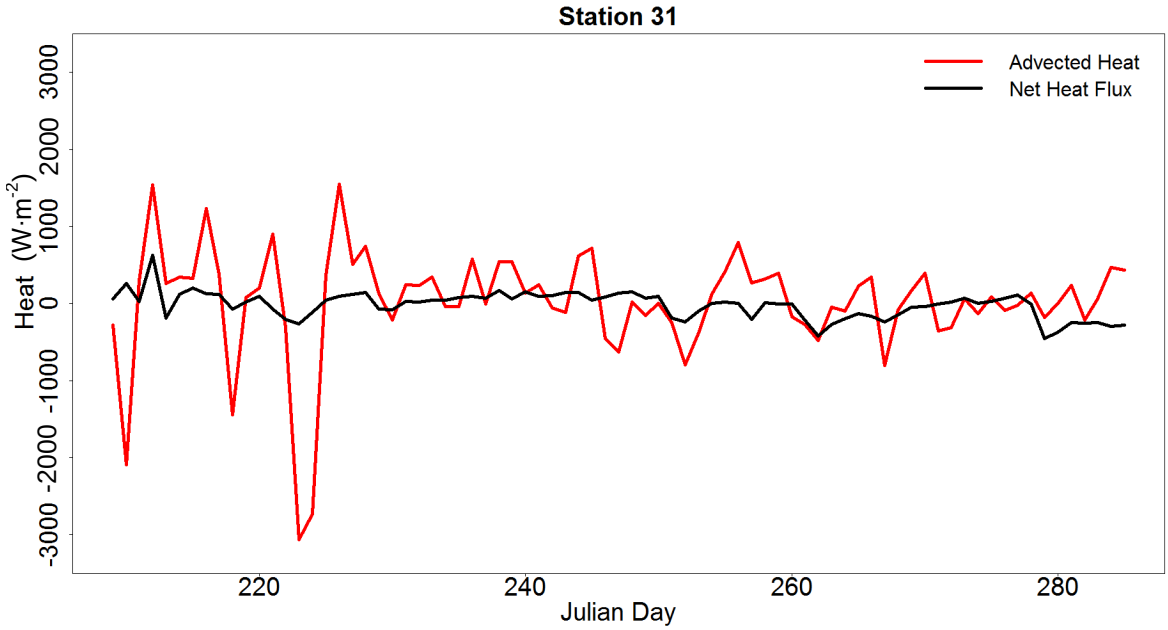

Figure 3.4h. Daily average advected heat for Station 31 (red) and net air-sea heat flux (daily average) calculated for Station 17 (black).

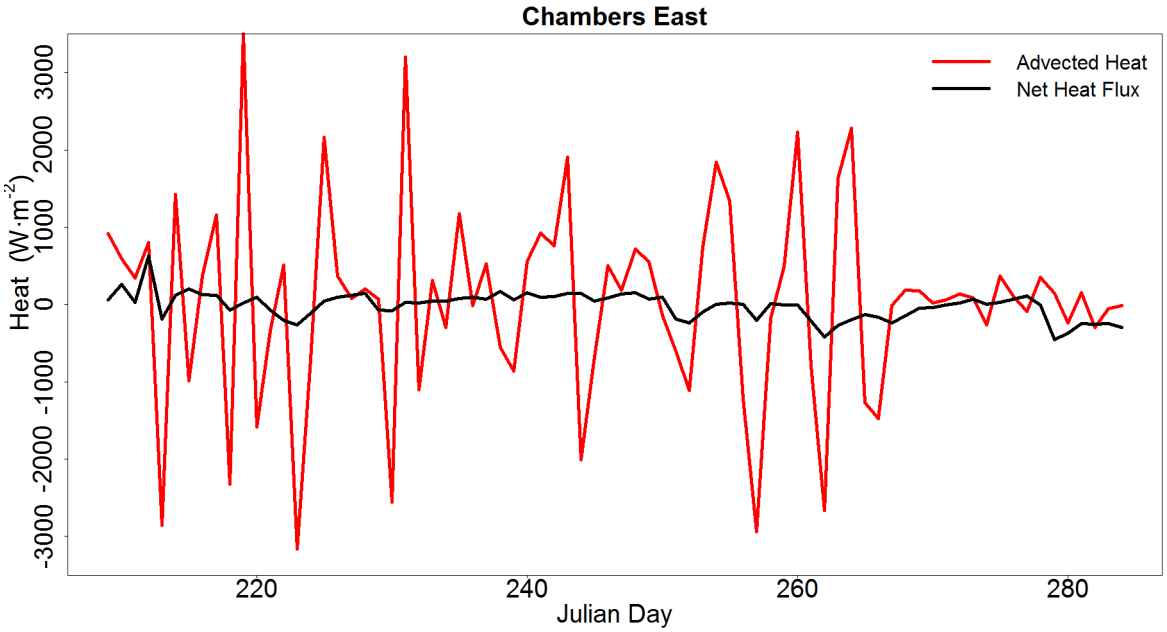

Figure 3.4i. Daily average advected heat for Chambers East (red) and net air-sea heat flux (daily average) calculated for Station 17 (black).

disconnects between water column temperatures and the net heat flux across the air-water interface. As expected, shortwave radiation was the primary driver of the heat flux early in the season, with its effect diminishing through the season, and latent heat flux became the dominant flux term as the year progressed.

3.3 Light Extinction Coefficients

K_d was calculated for each HOBO pendant profile conducted on monthly cruises (Fig. 3.5-3.7; Table 3.2). In general, light extinction coefficients were larger for shallow, southerly sites and smaller for deeper, northerly sites (Fig. 3.8). This trend agrees well with known attributes of Green Bay, notably the trophic gradient from hypereutrophic at the mouth of the Lower Fox River to mesotrophic north of Chambers Island, where waters mix more readily with Lake Michigan (Kennedy 1982; Miller and Saylor 1985; others). Occasional profiles exhibited curious behavior, particularly in the upper 1 to 2 meters (Fig. 3.6k). Some researchers have disregarded the top 1 meter due to highly variable data; however, this is the most influential layer for eutrophic waters. While some profiles, such as Figure 3.7a

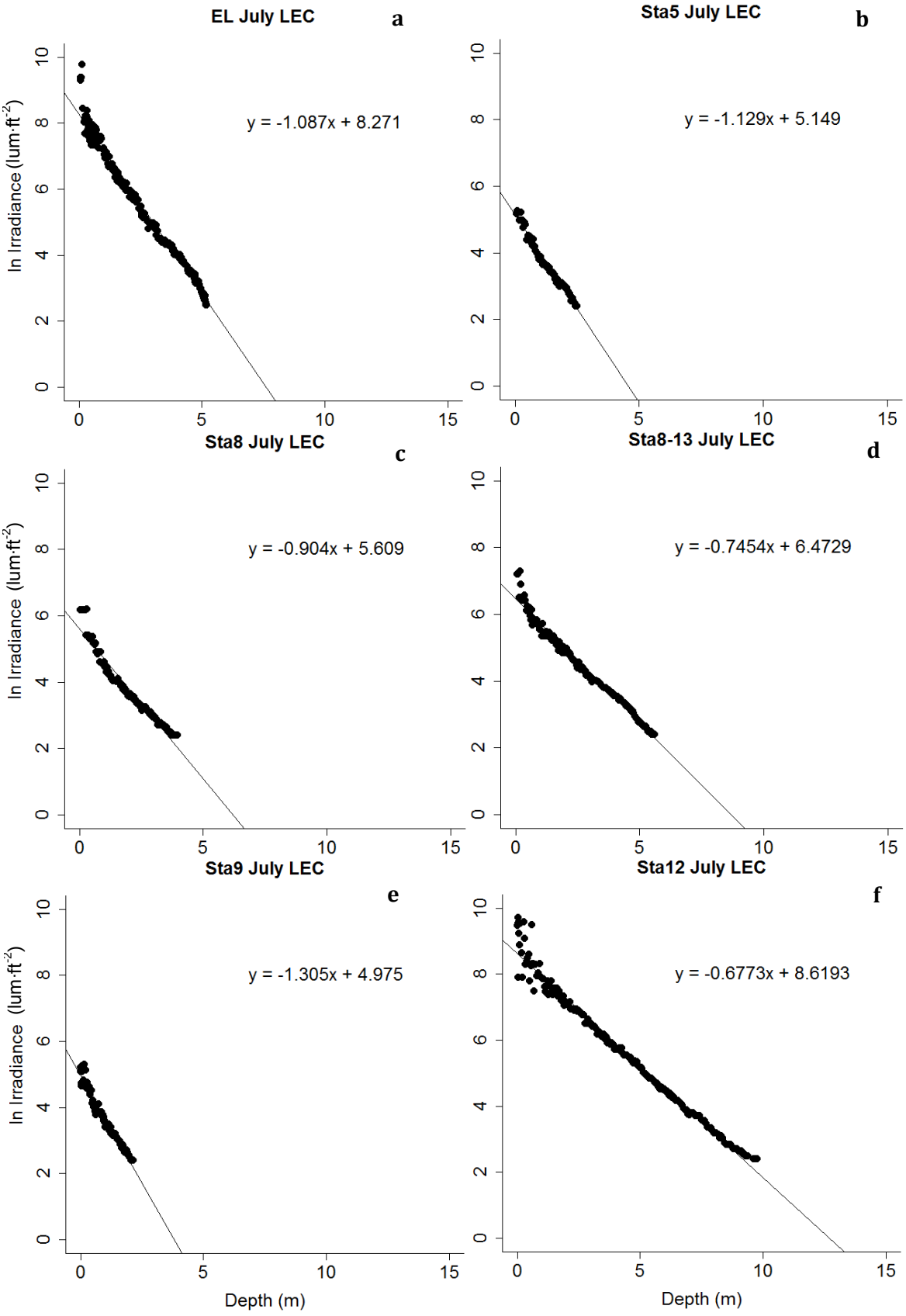

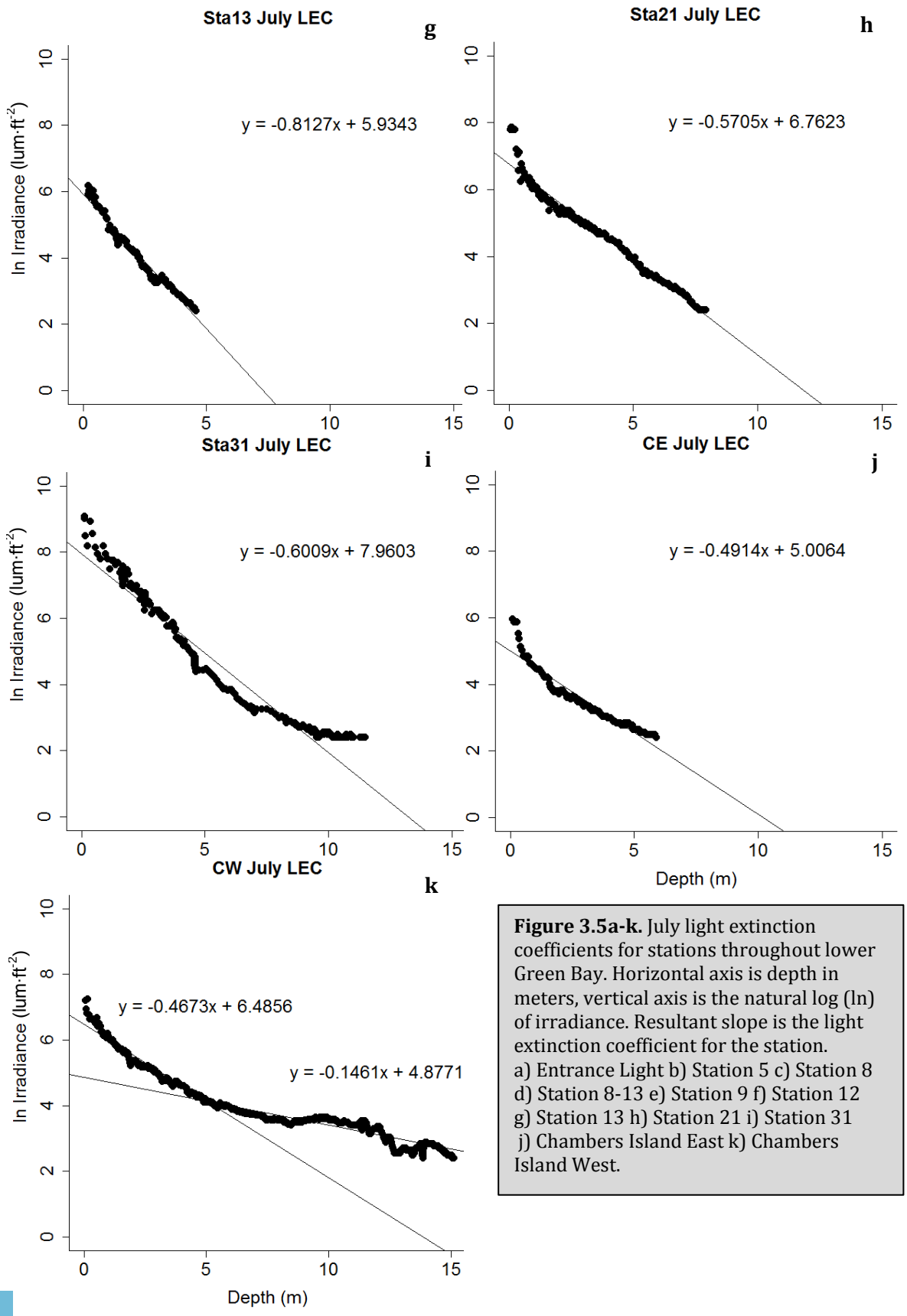

Figure 3.5a-k. July light extinction coefficients for stations throughout lower Green Bay. Horizontal axis is depth in meters, vertical axis is the natural log (ln) of irradiance. Resultant slope is the light extinction coefficient for the station.
a) Entrance Light b) Station 5 c) Station 8 d) Station 8-13 e) Station 9 f) Station 12 g) Station 13 h) Station 21 i) Station 31 j) Chambers Island East k) Chambers Island West.

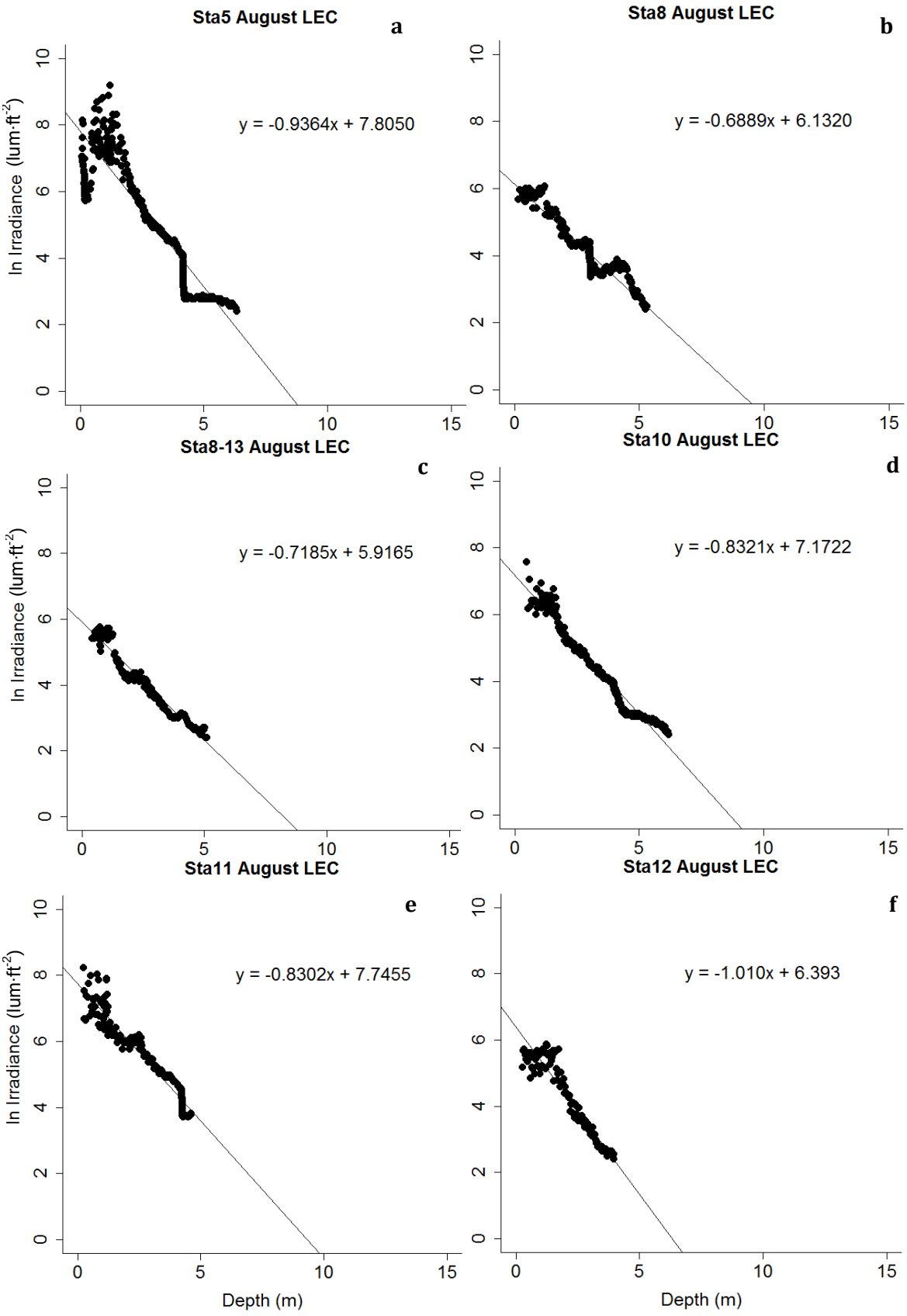

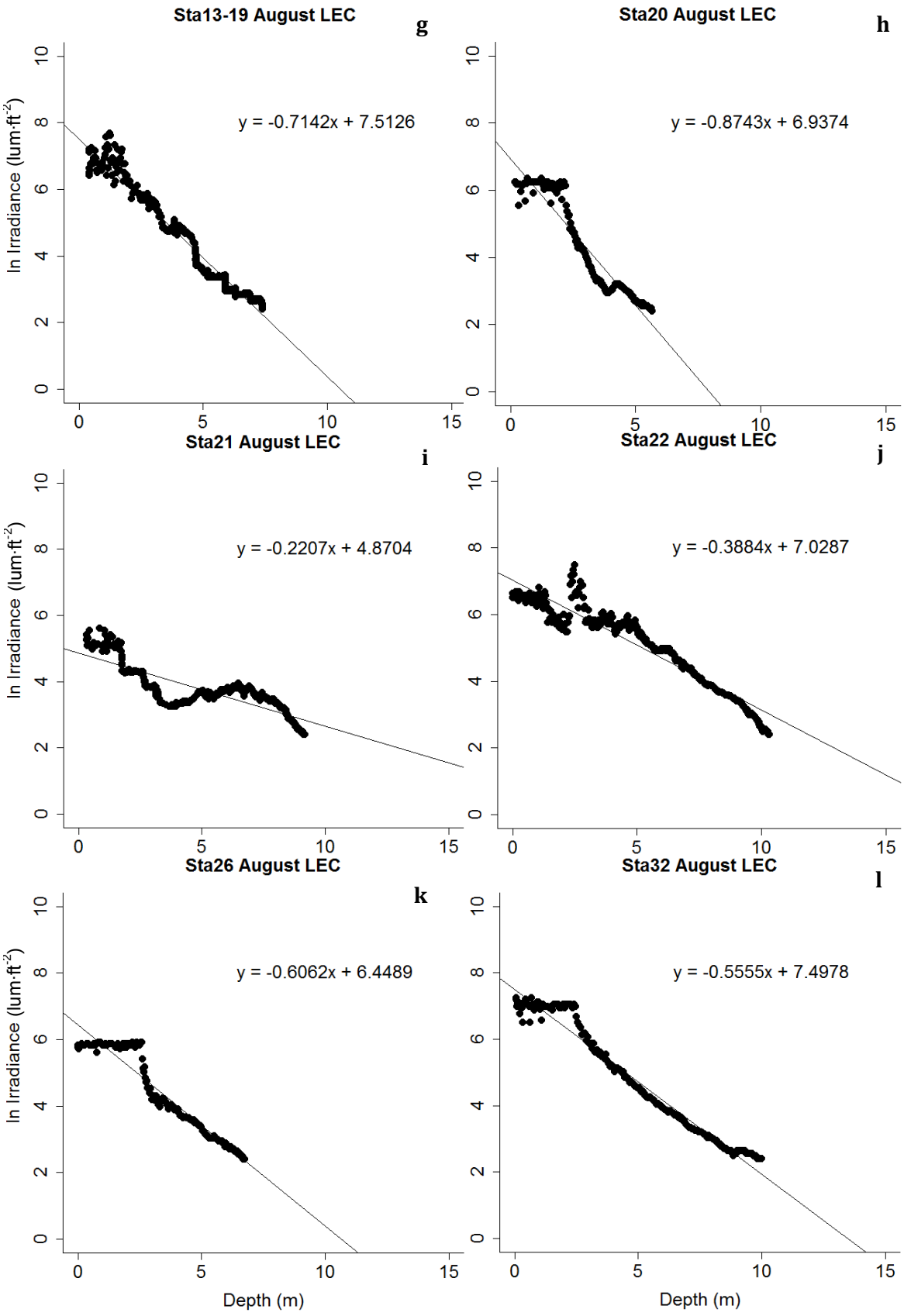

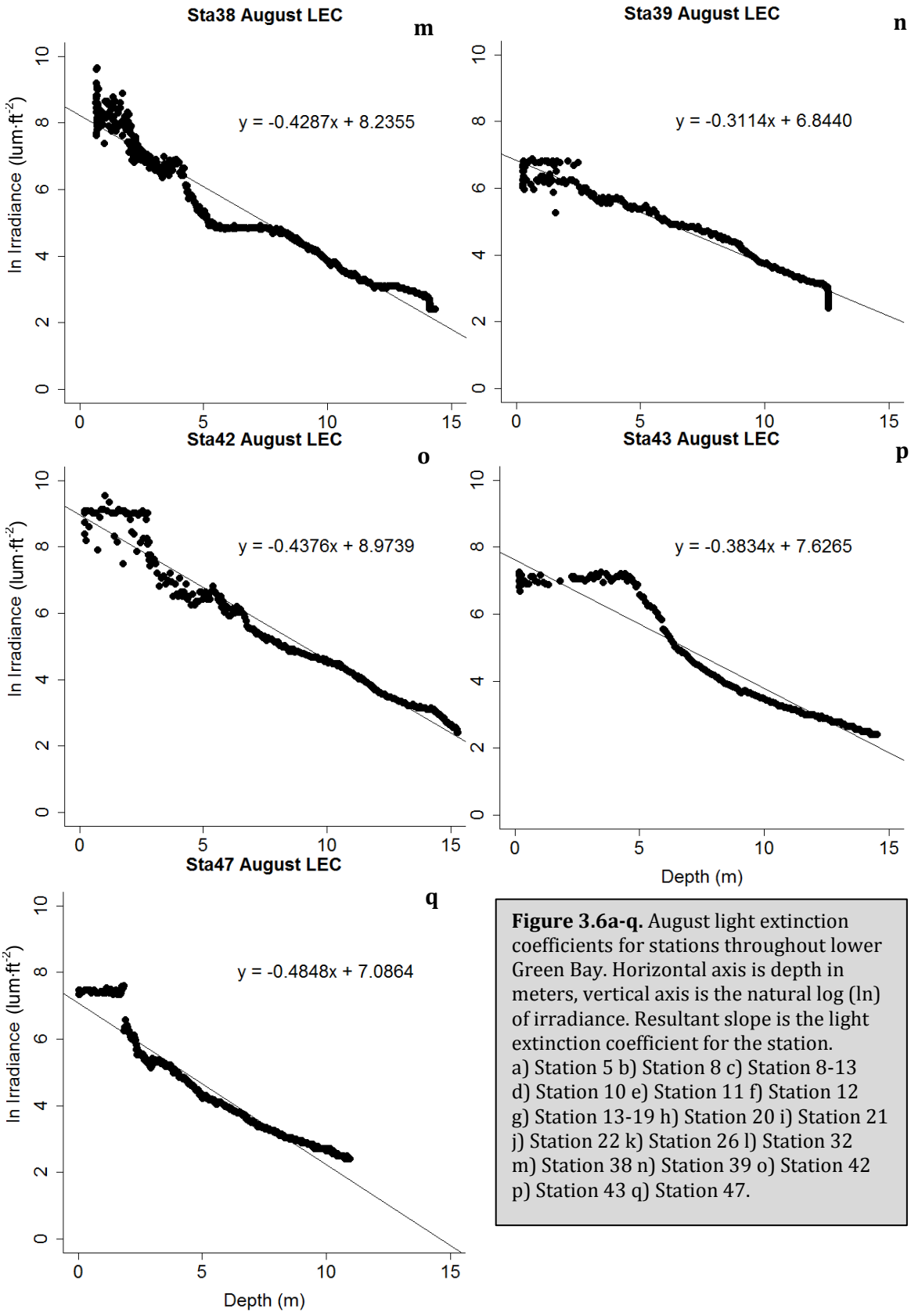

Figure 3.6a-q. August light extinction coefficients for stations throughout lower Green Bay. Horizontal axis is depth in meters, vertical axis is the natural log (ln) of irradiance. Resultant slope is the light extinction coefficient for the station.
a) Station 5 b) Station 8 c) Station 8-13
d) Station 10 e) Station 11 f) Station 12
g) Station 13-19 h) Station 20 i) Station 21
j) Station 22 k) Station 26 l) Station 32
m) Station 38 n) Station 39 o) Station 42
p) Station 43 q) Station 47.

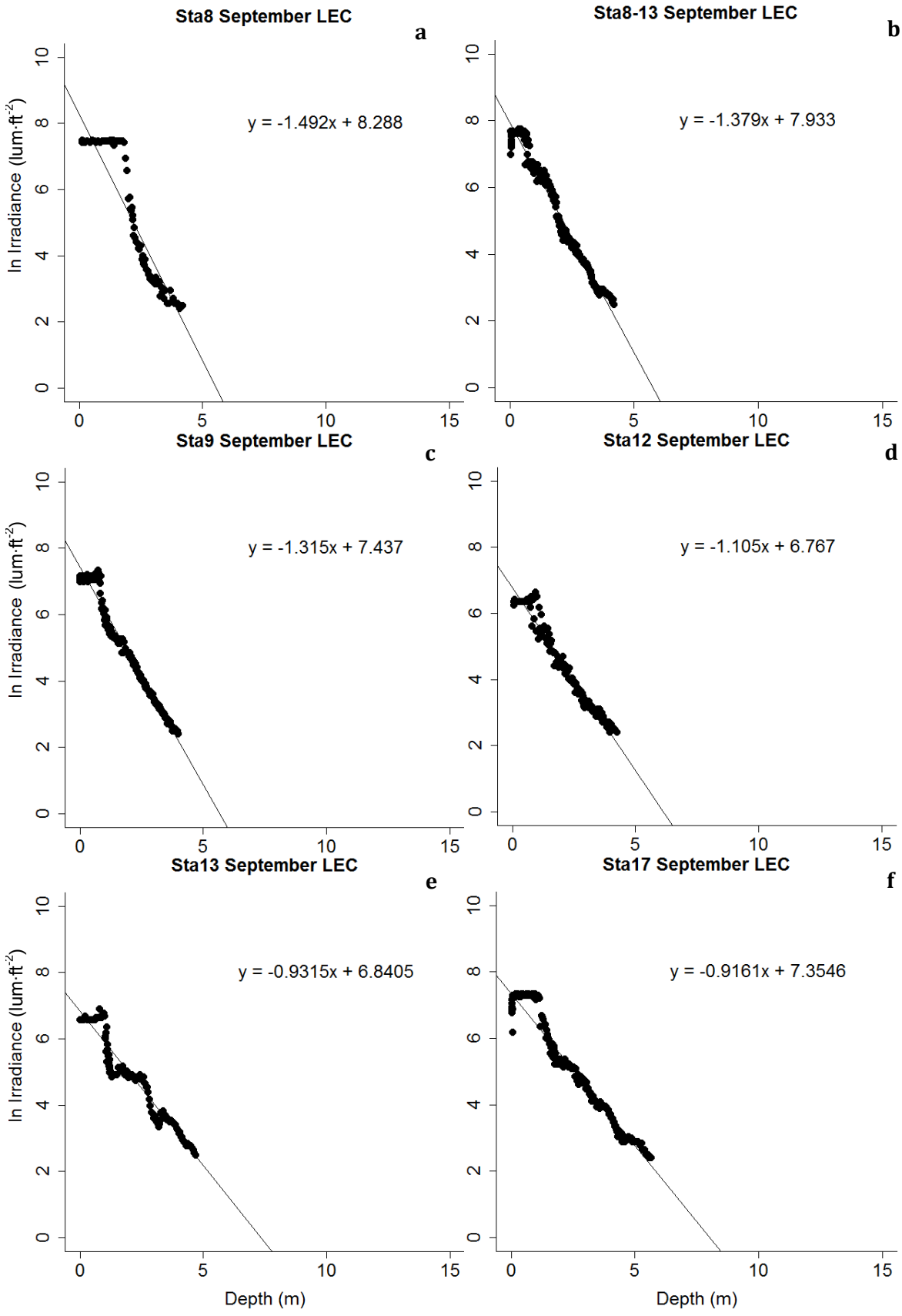

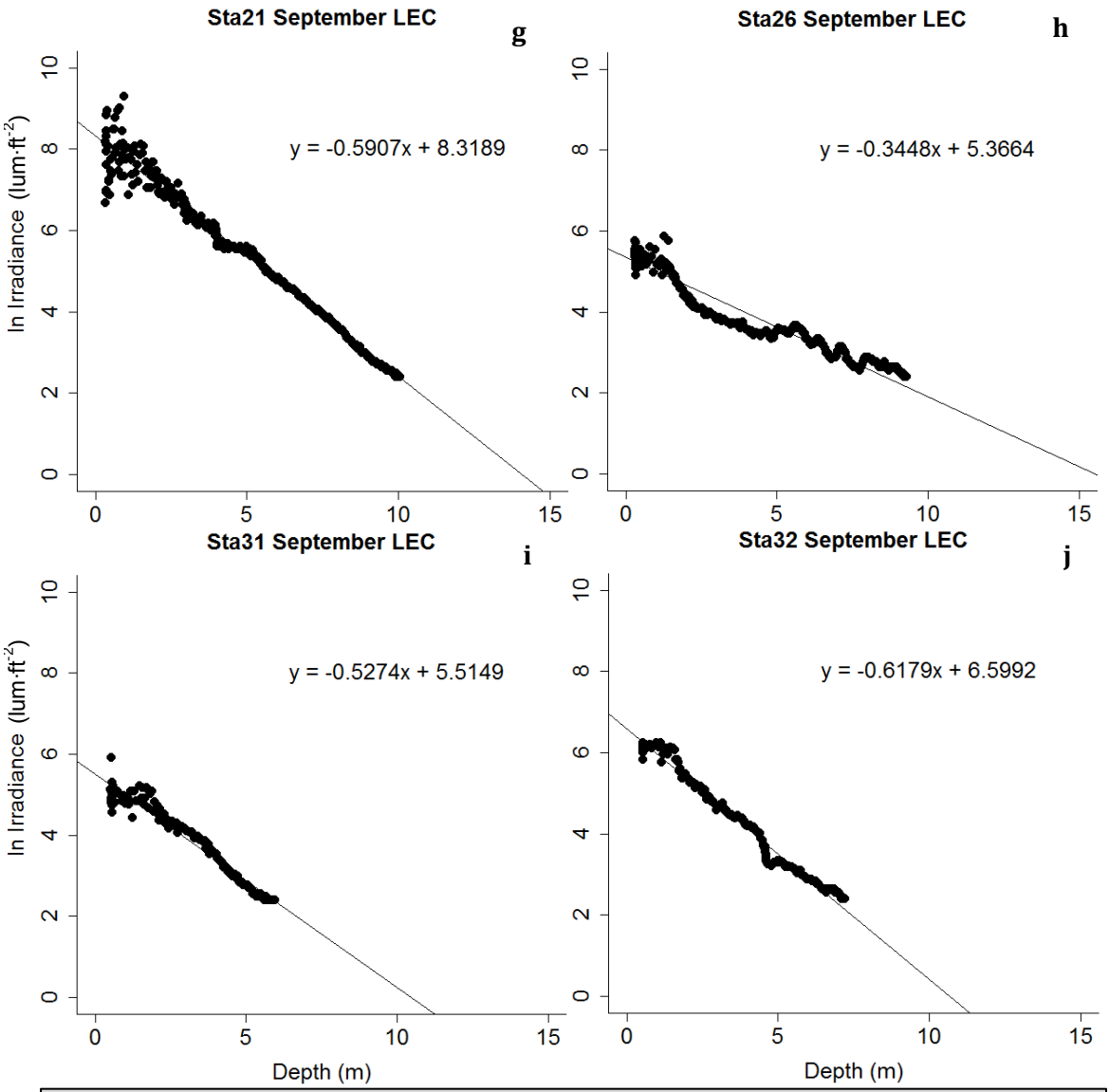

Figure 3.7a-j. September light extinction coefficients for stations throughout lower Green Bay. Horizontal axis is depth in meters, vertical axis is the natural log (ln) of irradiance. Resultant slope is the light extinction coefficient for the station. a) Station 8 b) Station 8-13 c) Station 9 d) Station 12 e) Station 13 f) Station 17 g) Station 21 h) Station 26 i) Station 31 j) Station 32.

(Station 8), indicate potential sensor irregularity (abnormal lag) due to irradiance values holding through the top two meters, the same sensor was used for all profiles and the rapid drop off in irradiance through the next few meters suggest that the overall trend line is reflective of light attenuation through the whole water column, on average.

Conversely, the sole profile for Chambers Island West (Fig. 3.5k) indicates two

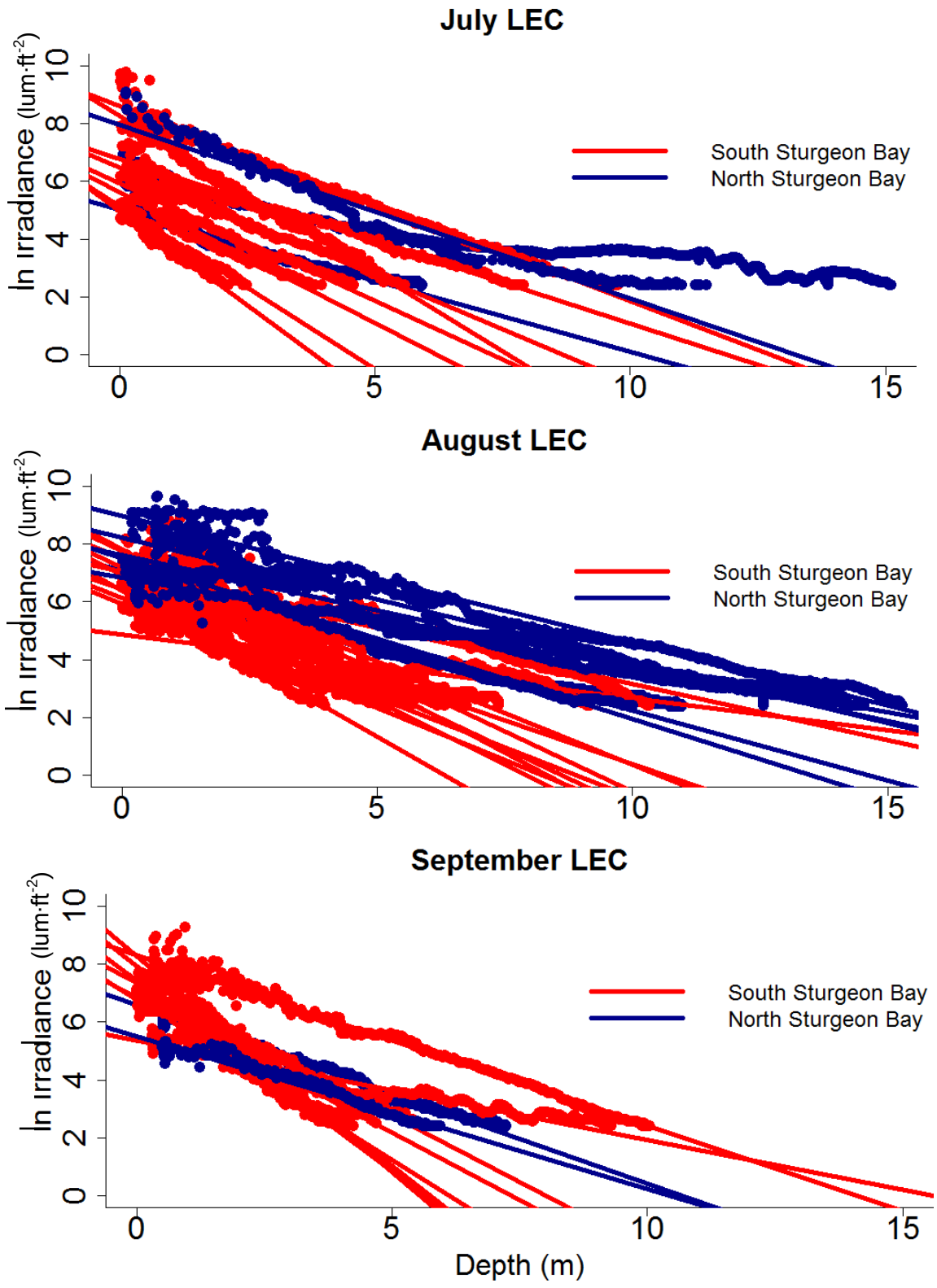

Figure 3.8a-c. K_d for all sampled stations by month. Red points are individual data points from stations south of Sturgeon Bay with red lines indicating the k_d value for individual stations south of Sturgeon Bay. Blue points are individual data points from stations north of Sturgeon Bay with blue lines indicating the k_d value for individual stations north of Sturgeon Bay.

Table 3.2. Light extinction coefficients from profiled stations in July, August, and September. "–" indicates the station was not sampled that month.

Station	July LEC	August LEC	September LEC
Entrance Light	1.087	–	–
5	1.129	0.9364	–
8	0.904	0.6889	1.492
8-13	0.7454	0.7185	1.379
9	1.305	–	1.315
10	–	0.8321	–
11	–	0.8302	–
12	0.6773	1.010	1.105
13	0.8127	–	0.9315
13-19	–	0.7142	–
17	–	–	0.9161
20	–	0.8743	–
21	0.5705	0.2207	0.5907
22	–	0.3884	–
26	–	0.6062	0.3448
31	0.6009	–	0.5274
32	–	0.5555	0.6179
38	–	0.4287	–
39	–	0.3114	–
42	–	0.4376	–
43	–	0.3834	–
47	–	0.4848	–
Chambers Island East	0.4914	–	–
Chambers Island West	0.4673/0.1461	–	–

distinct slopes, with the top five meters of the water column significantly more turbid than the remainder of the water column (k_d of 0.4673 and 0.1461, respectively). This suggests that the water mass between the surface and five meters is lower Green Bay water with either higher particulate content and/or higher nutrient levels, an observation that is supported by current meter data from previous years (Hamidi et al., in prep). However, hypolimnetic Lake Michigan water intrudes via cold water intrusions. While this water is expected to be much lower in both turbidity and nutrient content, it is also located below the thermocline and near the boundary of the photic zone at this site. Further investigation of both the western Chambers Island channel and the bay north of Chambers Island is necessary to elucidate these preliminary findings.

After plotting k_d values from profile data using a Kriging interpolation of the bay, two trends were noticed (Fig. 3.9a-c). The first trend was that, for stations with profiles taken every month, k_d tended to be highest in September, with most of these sites exhibiting lower k_d in August than in July. While only a few sites were consistently profiled on each cruise due to time limits with other cruise activities, time of day at the station and occasional sensor failure (e.g. data transfer to computer failed), the spatial coverage of the bay and the proximity of sites sampled provides considerable support for spatial and temporal trends, namely that southern bay sites exhibited k_d values that were much higher than northern sites. Higher k_d values in September were attributed to full water column mixing throughout the bay during the September cruise (Julian days 256-257), which is supported by the near isothermal and weakly stratified thermal profile data from this period. These mixing events are known to cause significant resuspension of bottom sediments (Klump et al. 2009). The second trend was that k_d trended higher within the region that previous studies have shown is the Lower Fox River plume and depositional zone (Kennedy 1982; Lathrop et al. 1990; Hamidi et al., in prep) (Fig. 3.9b).

3.4 Optical Depth

Optical depths were calculated for each sampled station for the months of July, August, and September (Table 3.3). Optical depth is essentially a reflection of k_d, but is a more pragmatic way of visualizing the photic depth, or depth at which the amount of visible light is no longer conducive for primary productivity. Optical depth corresponds to different depths in the water column but represents the same diminution of the light between different water bodies or regions within the same water body. Typically, two optical depths are of concern: the 10% and 1% optical depths, with the former corresponding to the mid- point of the photic zone and the latter synonymous with the photic depth (Kirk 1994). The photic depth indicates the depth in the water column in which gross primary productivity and

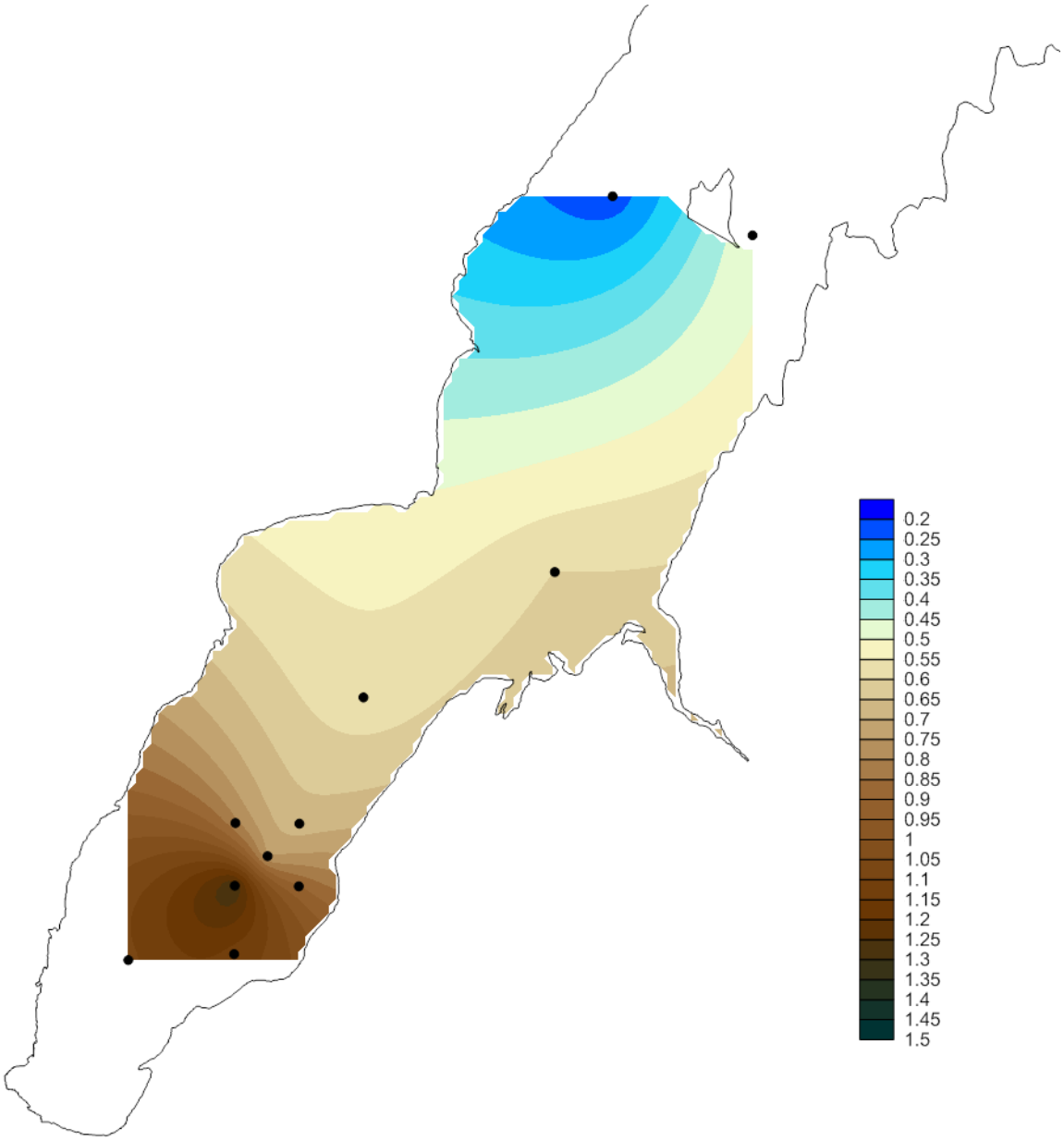

Figure 3.9a. July light extinction coefficients for profiled stations, taken from July 24-26. Data interpolated and extrapolated using the Kriging method.

respiration are equal. The photic depth can also be used as a tool to suggest which genera of phytoplankton one can reasonably expect within the water column. In waters with a small photic depth, phytoplankton genera that are more adept at maintaining their position within the water column, such as cyanobacteria, can be expected (Graham et al. 2009). This, in turn, further suggests what the ecosystem status of the waters are for that

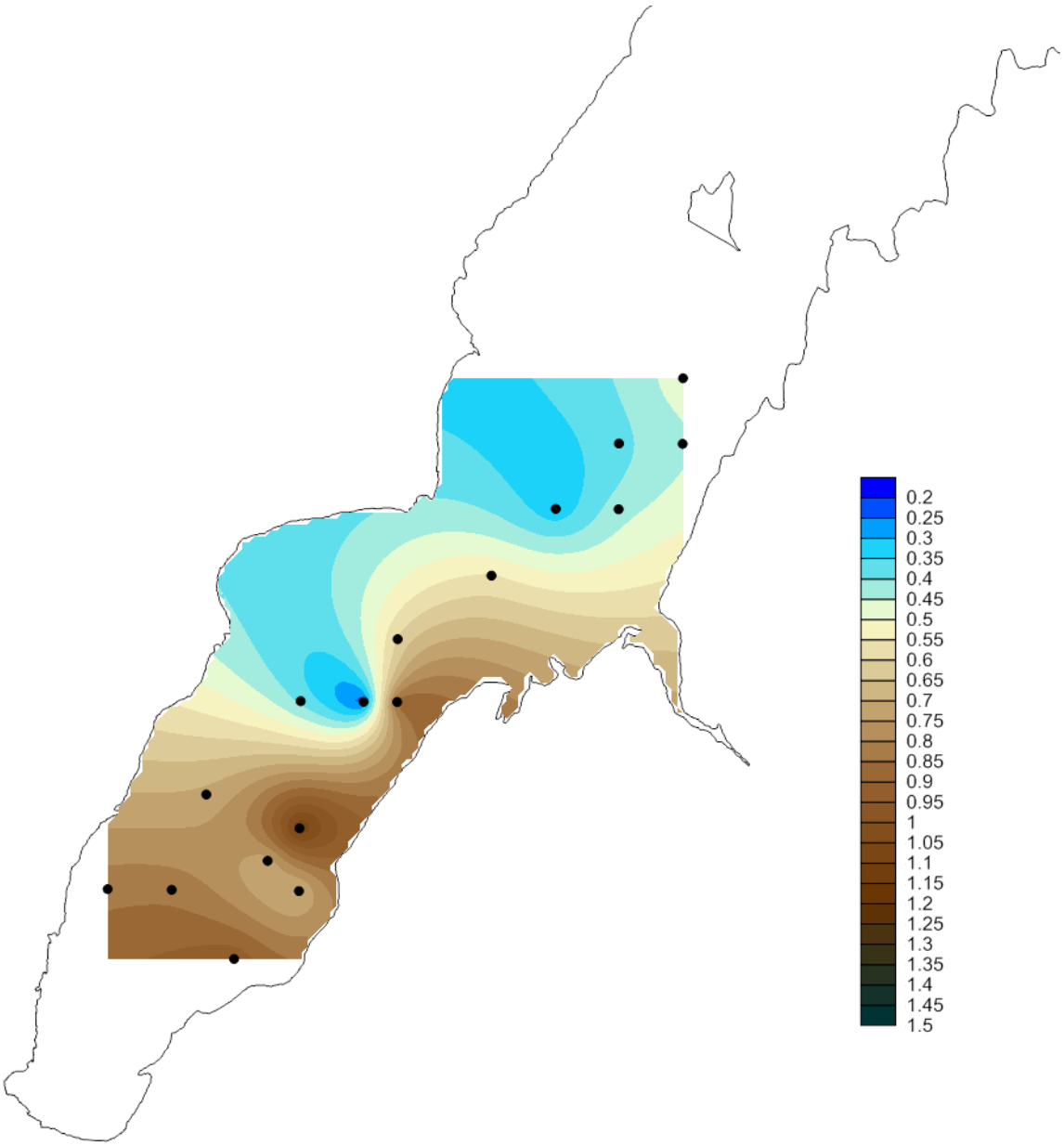

Figure 3.9b. August light extinction coefficients for profiled stations, taken from August 21-23. Data interpolated and extrapolated using the Kriging method.

region. However, sampling of the water is required to ascertain which phytoplankton genera are actually present.

3.5 Primary Productivity and Solar Irradiance

Primary productivity estimates for the lower bay were produced from light-dark bottle experiments conducted on cruises over the study period with water taken from Station 17 at a depth of 4m. Productivity was taken as the concentration of oxygen after the incubation

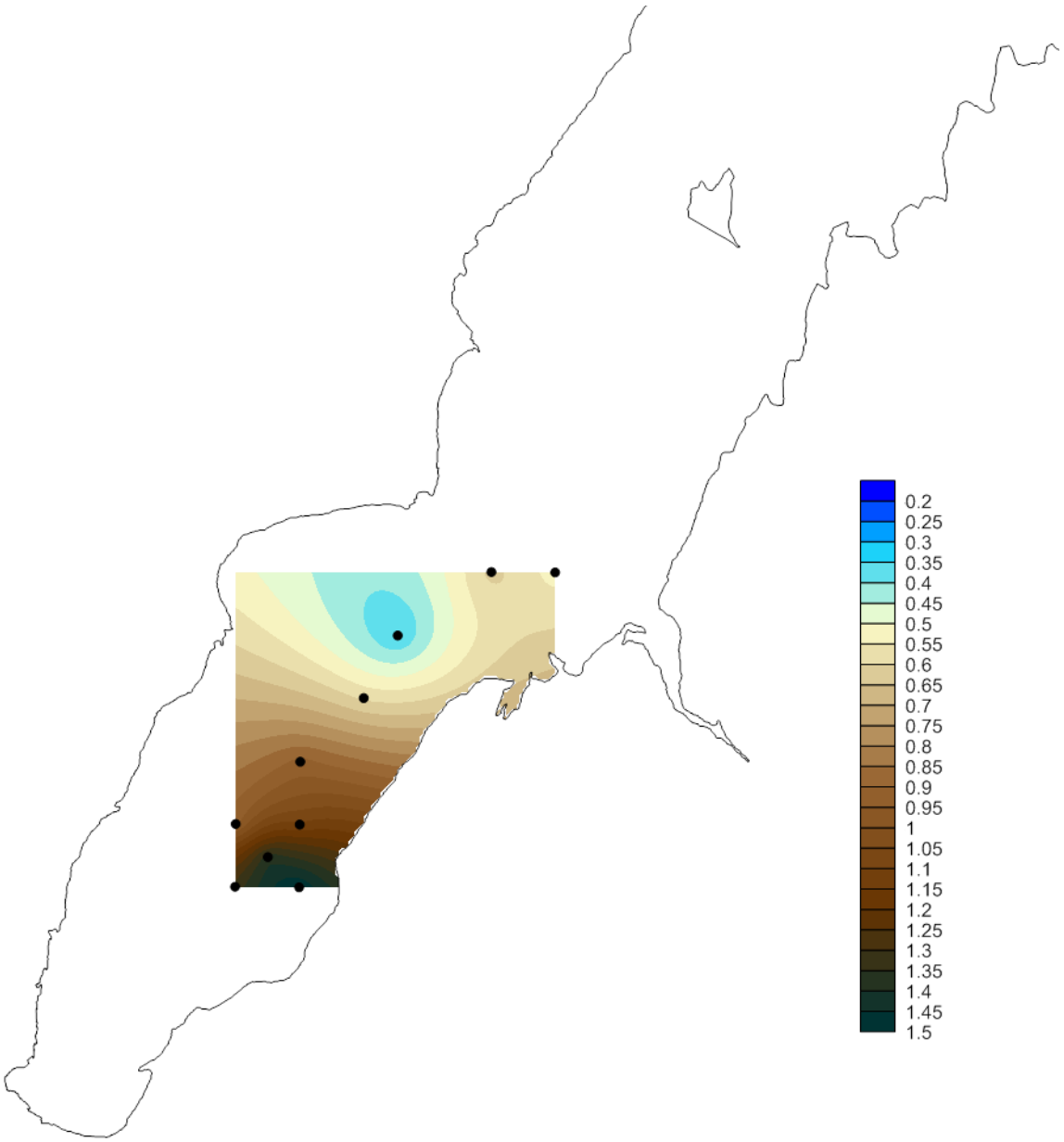

Figure 3.9c. September light extinction coefficients for profiled stations, taken from September11-13. Data interpolated and extrapolated using the Kriging method.

period minus the initial concentration of oxygen. Varying levels of shading (using screen wrapped around the incubating bottles at levels of no wraps, two wraps, and four wraps) were used to produce different light levels resulting in approximately 70% and 90% reductions in incident irradiance (Appendix D). Clear bottles indicated photoinhibition and reduced productivity rates, while the bottles with shading produced productivity rates that

Table 3.3. Optical depth (OD) in meters for sampled stations, with 1% OD synonymous with photic depth. "–" indicates the station was not sampled that month.

Station	July 10% O.D.	July 1% O.D.	August 10% O.D.	August 1% O.D.	September 10% O.D.	September 1% O.D.
EL	2.1	4.2	–	–	–	–
5	2.0	4.1	2.5	4.9	–	–
8_13	3.1	6.2	3.2	6.4	1.7	3.3
8	2.5	5.1	3.3	6.7	1.5	3.1
9	1.8	3.5	–	–	1.7	3.5
10	–	–	2.8	5.5	–	–
11	–	–	2.8	5.5	–	–
12	3.4	6.8	2.1	4.2	2.1	4.2
13	2.8	5.7	–	–	2.5	4.9
13_19	–	–	3.2	6.4	–	–
17	–	–	–	–	2.5	5.0
20	–	–	2.6	5.3	–	–
21	4.0	8.1	10.4	20.8	3.9	7.8
22	–	–	5.9	11.8	–	–
26	–	–	3.8	7.6	6.7	13.3
31	3.8	7.7	–	–	4.4	8.7
32	–	–	4.1	8.3	3.7	7.4
38	–	–	5.4	10.7	–	–
39	–	–	7.4	14.8	–	–
42	–	–	5.3	10.5	–	–
43	–	–	6.0	12.0	–	–
47	–	–	4.7	9.5	–	–
CE	4.7	9.4	–	–	–	–
CW	10.7	21.4	–	–	–	–

were assumed to be more accurate for the aquatic environment, especially when compared to values found for the clear and dark bottles (Appendix D). These values were also within the bounds described for Green Bay by Sager et al. (1984).

Using these productivity values as estimates of the amount of light energy converted to biochemical energy and unavailable for heat transfer into the water column, the significance of algal absorbance of incoming solar irradiance on the overall heat budget was estimated. Considering that the purpose of this calculation was to determine the extent to which primary productivity "steals" heat from the net heat budget (the heat budget assumes

that all incident solar irradiance that is not reflected is converted to heat energy within the water column), rough values were used to approach the subject on a magnitude scale as it was assumed that the overall value would be small in comparison to the total solar irradiance absorbed by the abiotic components of the water column. Thus, an average photic depth of 6 meters was assumed for the region south of Chambers Island due to inconsistency of sampled stations between months.

The primary productivity for the bay was estimated at 375-1200 mg $C \cdot m^{-3} day^{-1}$, which falls within the volumetric-based range described by Sager et al. of 7-1382 mg $C \cdot m^{-3} day^{-1}$ for the whole bay (1984). Considering this value converted into mol $C \cdot m^{-3} day^{-1}$ (0.031 –0.100) and multiplied by the energy (in W) incident upon the bay within the wavelengths of 400-700nm results in an estimate of 0.63-3.15 $W \cdot m^{-3}$. Considering an average photic depth of 6 meters results in a range of values between 3.78-12.08 $W \cdot m^{-2}$ within the photic zone of the bay (the upper 6m of the bay) (Appendix D). These values are, on average, an order of magnitude less than the incident solar irradiance that is absorbed by the bay. Thus, while the values are not small, they are also not significant.

3.6 Short Term Analyses

Diel cycles, and thus short-term heating and cooling trends, can be garnered from short term analyses of mooring data. Coupled with meteorological data for the period and flux terms, a better understanding of the driving forces in the heating, cooling, and distribution of different water masses within the water column can be ascertained. Temperature plots were produced using the Kriging method of interpolation.

Solar heating of the upper few meters of the water column was evident in all moorings where surface water temperature data were available. The depth of heating and magnitude of heating was noticeably different between stations of varying depths, which also corresponds to an extent with general trends in water clarity seen earlier (i.e. southerly

stations have more surface warming than northern stations, but there is significant variability amongst southern stations). Stations with a greater depth are farther north, and thus tend to have clearer waters. It is very evident across stations that there is nightly cooling of surface waters, with surface waters cooling much more after days of high solar irradiance (typically clear sky or partly cloudy days). It is also quite noticeable that overcast days experience reduced diel heating of surface waters, a feature that is again consistent across stations. Diel heating of the surface waters extends to a depth of approximately two meters below the surface at shallow stations (Station 8 and 9 considered here), and to a depth typically of 6-8 meters, but occasionally only 4 meters, at Station 31 (based on interpolated data). The variance is due to incident solar irradiance and depth of near isothermal conditions (the depth of the mixed layer, here considered the layer where thermal stratification is weak enough to be overcome by convective and wind mixing). Surface heating is considered across a temperature range of 1˚C, where the bottom of the surface heating is considered the depth at which the water temperature is 1˚C cooler than surface water temperatures.

The diel signal is most evident during periods of high solar irradiance (clear sky or partly cloudy conditions). However, warm air temperatures appear to suppress the extent of heat flux across the air-sea interface, resulting in exaggerated diel signals in the upper meter during days with high solar irradiance, high air temperatures, and minimal wind.

Diverse meteorlogical conditions were present between Julian day 197-203, resulting in significant changes within the water column (Fig. 3.10a-g). Station 8-13 illustrates the conditions required for full water column mixing over the period Julian day 197-203 (Fig. 3.10f). A cold water mass appears at the site around Julian day 200, during a period of moderately strong mean winds (>6 $m \cdot s^{-1}$, intermittently with occasional mean winds above 8 $m \cdot s^{-1}$) (Fig. 3.10c). Julian day 201 was overcast, with no diel warming signal.

This period also coincided with increased mean wind speeds above 10 $m \cdot s^{-1}$. This wind period proved strong enough to mix the cool bottom waters with the warmer overlying waters. In days prior to the cold water intrusion, diel warming of surface waters led to temperatures exceeding 26˚C, with peak temperatures of 27˚C. The intruding cold bottom waters had temperatures near 14˚C. During the intrusion, and likely due to the moderately strong mean wind speeds (Fig. 3.10c), only a small diel signal was seen on Julian day 200 (Fig. 3.10f). It is not clear whether the reduced diel warming signal is due to entrainment of cool bottom waters into the mixed layer or due to increased flux to the atmosphere due to moderately strong mean wind speeds, as air temperatures were cooler than surface water temperatures over this period (up to 1.5˚C cooler) (Fig. 3.10a). However, upon inspecting the depth-time temperature profile for Station 21 over this period, it is suspected that an emphasis should be placed on entrainment of cold waters, as the entire water column becomes significantly cooler at this period than it was in previous days (Fig. 3.10g).

During clear sky periods with high winds (above 8 $m \cdot s^{-1}$ or persistent winds above 5 $m \cdot s^{-1}$), surface heating is extended beyond the previously mentioned range, with surface

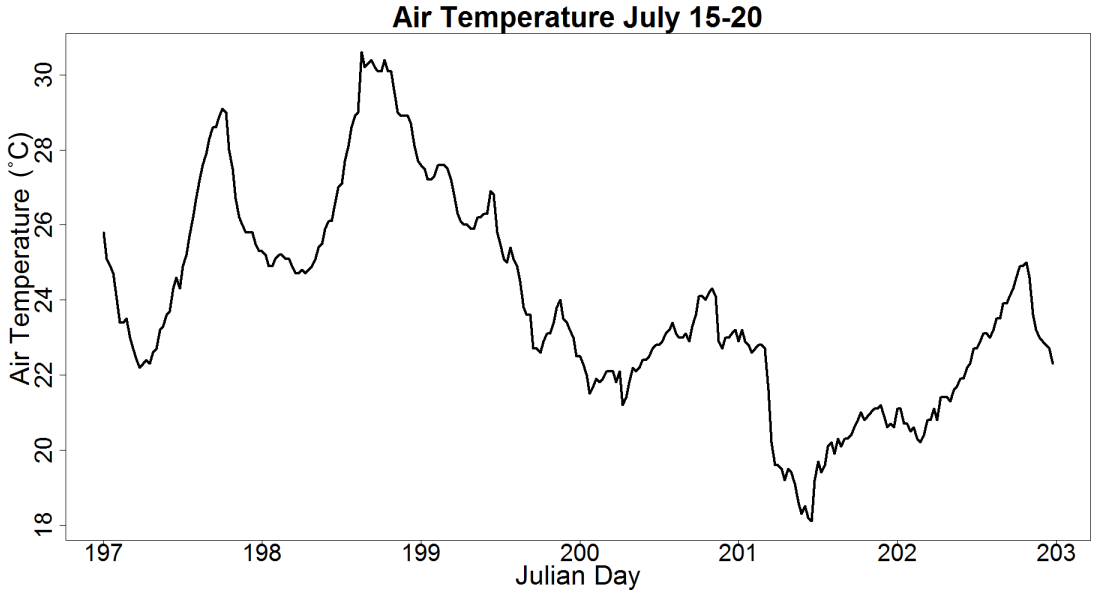

Figure 3.10a. Air temperature from the buoy meteorological station from July 15-20, 2012.

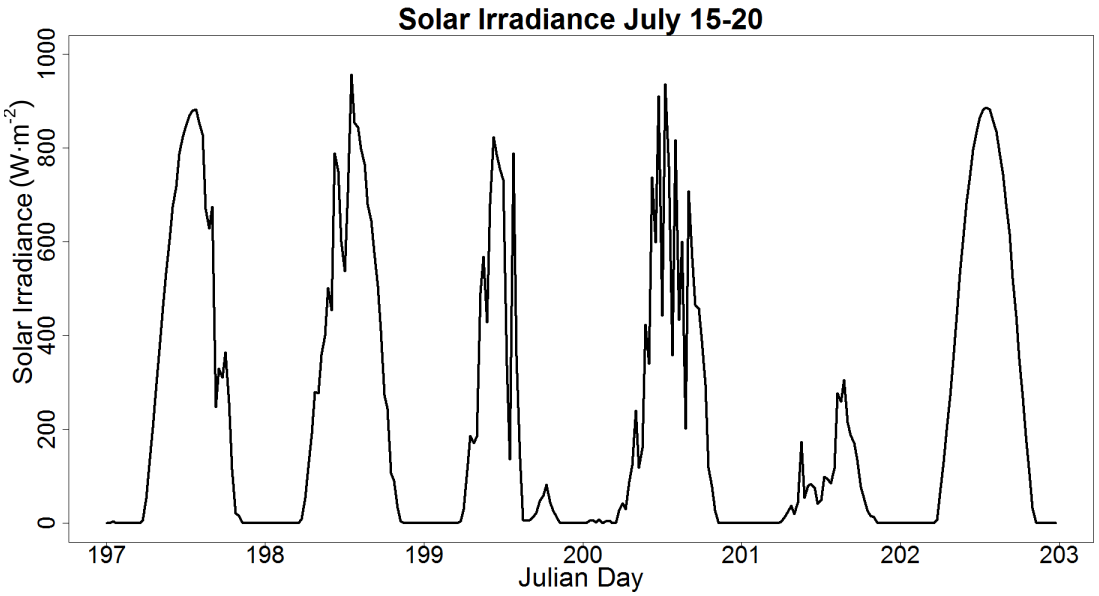

Figure 3.10b. Solar irradiance from the buoy meteorological station from July 15-20, 2012.

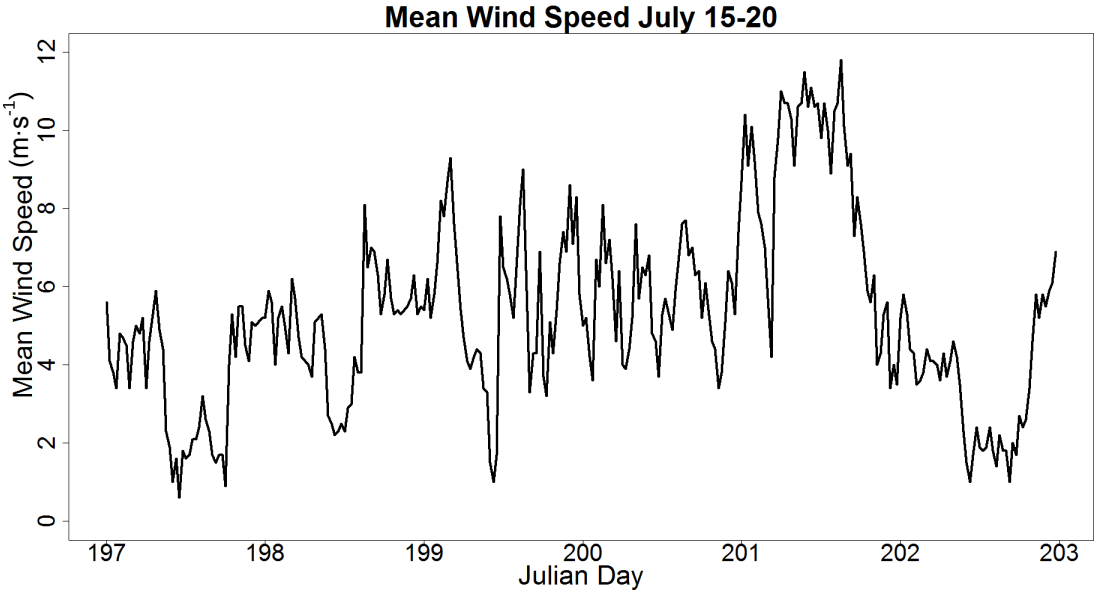

Figure 3.10c. Mean wind speed from the buoy meteorological station from July 15-20, 2012.

temperatures still heating more than underlying waters but to a lesser extent (Fig. 3.11a-j). Station 31, between noon on Julian day 228 and midnight on Julian day 229, experienced such conditions (Fig. 3.11j). The surface waters heated with a fairly typical diel signal, but mixing of the water column extended the base of the heated water mass two meters deeper, to a depth of approximately ten meters from the surface. Conditions during Julian day 229 were such that full mixing of the epilimnion occurred and no diel warming was seen.

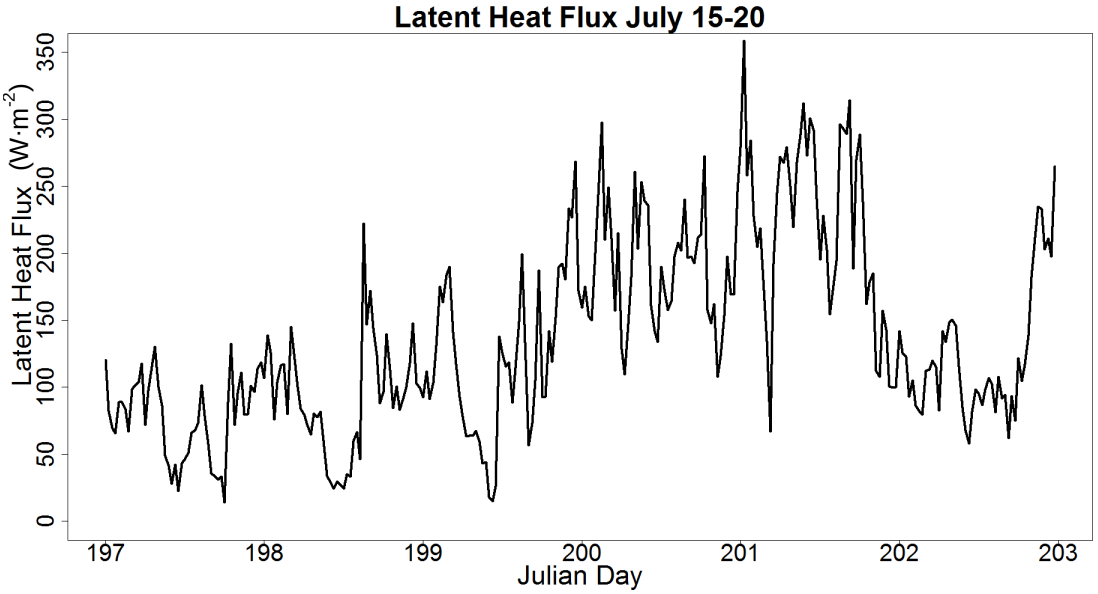

Figure 3.10d. Latent heat flux from July 15-20, 2012.

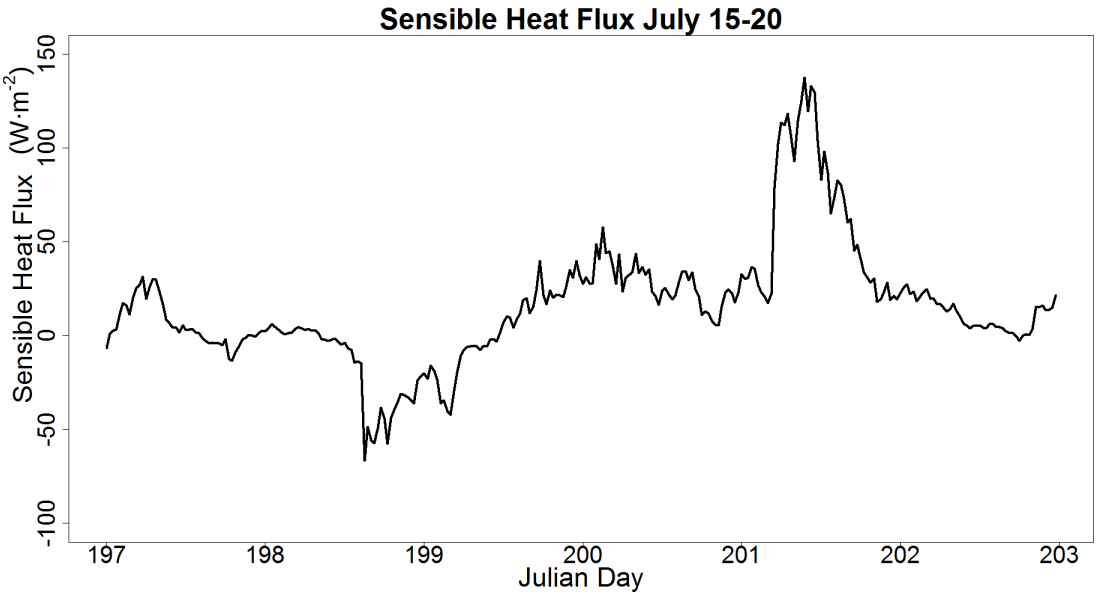

Figure 3.10e. Sensible heat flux from July 15-20, 2012.

Cooling of the surface waters overnight occurred, largely attributed to the significant drop in air temperatures to 16˚C in the early morning hours of Julian day 230 (Fig. 3.11a). Julian day 230 had a daytime high of 22˚ C, over 2˚C cooler than Julian day 228 (Fig. 3.11a). Julian day 230 experienced a small diel warming signal (approximately 0.5˚ C as opposed to the

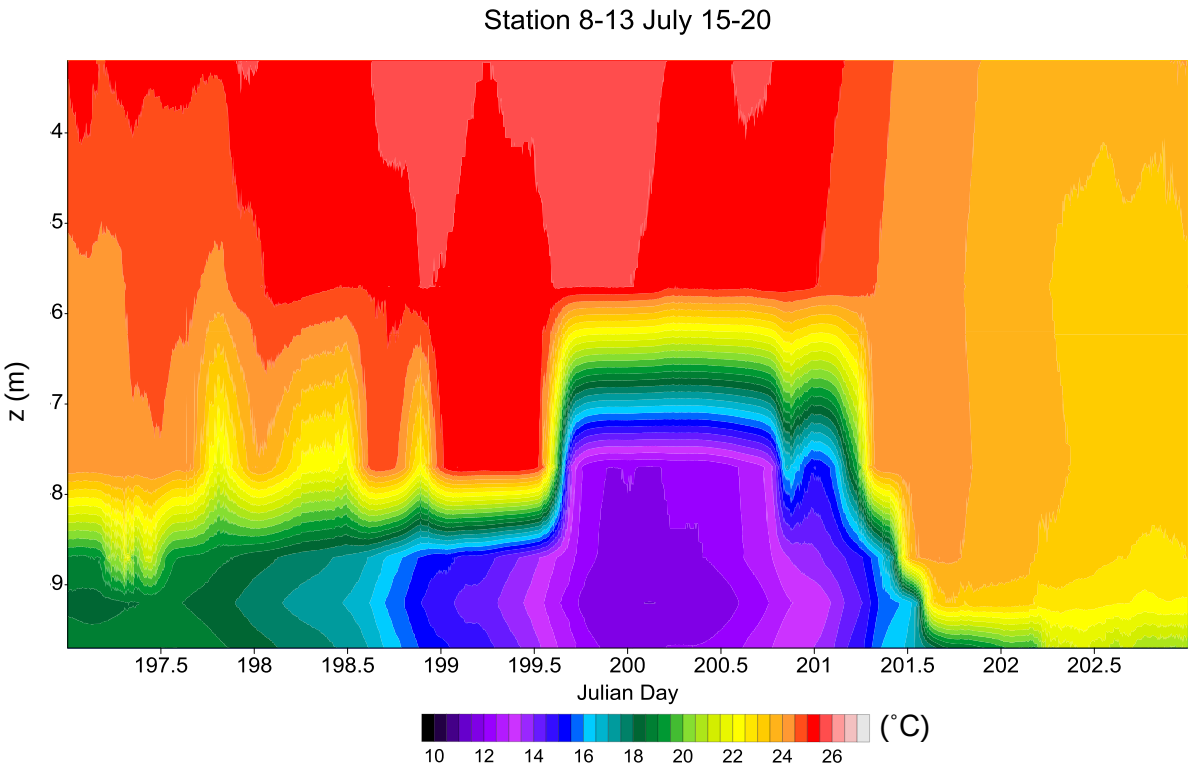

Figure 3.10f. Depth-time temperature plot for Station 8 from July 15-20, 2012.

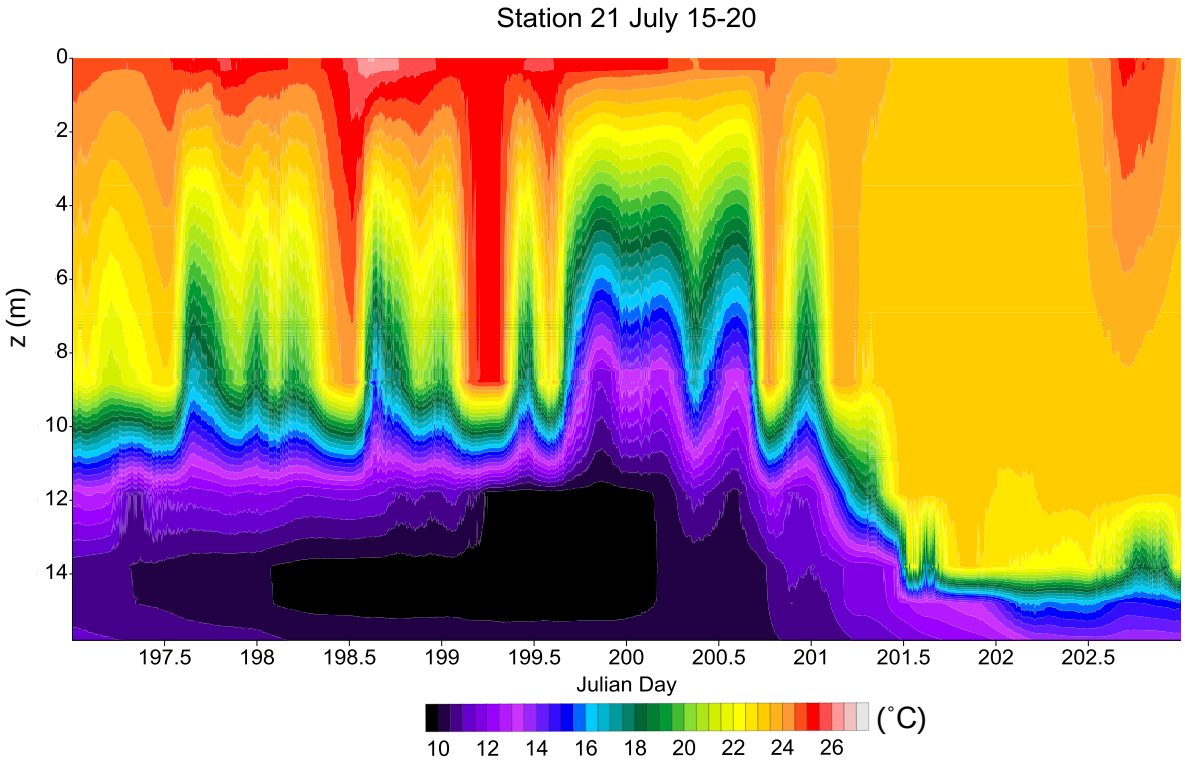

Figure 3.10g. Depth-time temperature plot for Station 21 from July 15-20, 2012.

typical warming of 1.5˚C) (Fig. 3.11j). It was hard to determine the primary cause of this, as the daytime air temperatures were much cooler, which could allow for increased heat exchange at the air-sea interface and a smaller diel warming signal. However, full mixing of the water column during a period of cool water intrusions and a shallower thermocline depth also suggest that this could significantly impact the diel warming signal. Analysis of other periods with a cooling of air temperatures but no cold water intrusions is required to better determine the cause.

Julian days 215-220 at Station 9 did not show any signs of a cold water intrusion (Fig. 3.11g). However, diel warming signals were quite variable, with water at depth warming to a similar extent as the surface waters during periods of high mean wind speeds (Fig. 3.11c). This period experienced high solar irradiance (the entire stretch of days included primarily clear sky conditions) (Fig. 3.11b). A decrease in daytime air temperatures occurred on Julian day 218, with a gradual increase each day after (initial drop in temperature of nearly 3˚C) (Fig. 3.11a). Mean wind speeds were above 6 $m \cdot s^{-1}$, with occasional speeds above 8 $m \cdot s^{-1}$, for much of the period between Julian day 218 and Julian day 220 (Fig. 3.11c). During this period, a warm layer of water occurred approximately four meters below the surface (generally 0.5˚C warmer than surface water temperatures), with waters nearly isothermal but cooler below this layer (Fig. 3.11g). This is near the accuracy of the HOBO loggers used and thus may not be representative of what is actually happening, as Station 8-13 did not exhibit a subsurface warm water mass (Fig. 3.11f).

Station 31 showed similar trends over the same period (Julian day 215-231) (Fig. 3.11j). It is evident that the cold water intrusion reached Station 31 prior to Station 9 by a few days, with Julian day 218 showing cooling of the surface layer and the entrainment of cooler, hypolimnetic waters into the mixed layer, likely due to convective mixing. Julian

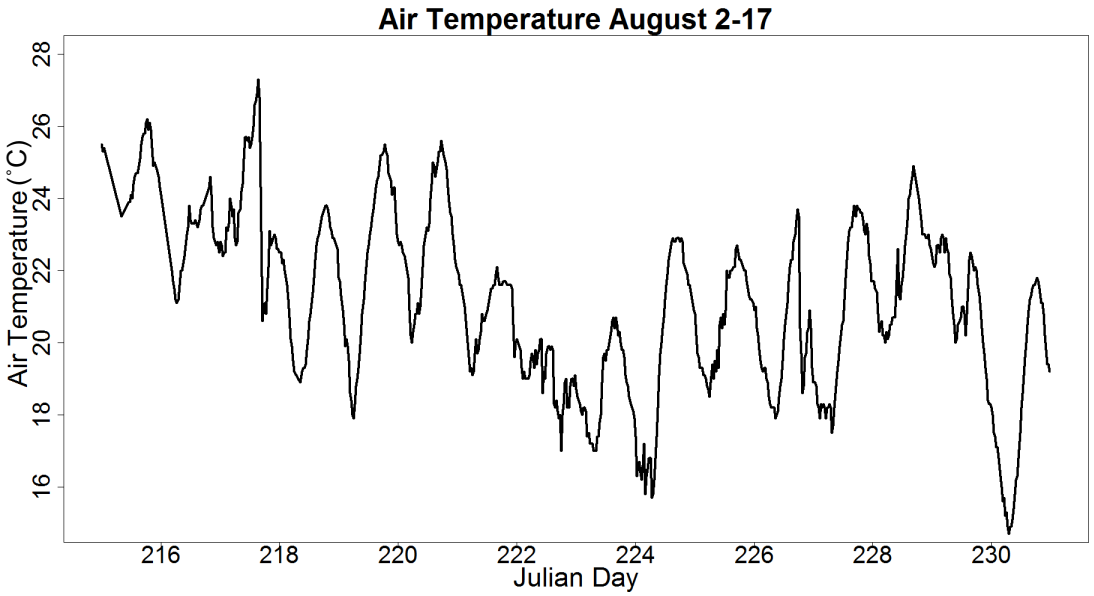

Figure 3.11a. Air temperature from the buoy meteorological station from August 2-17, 2012.

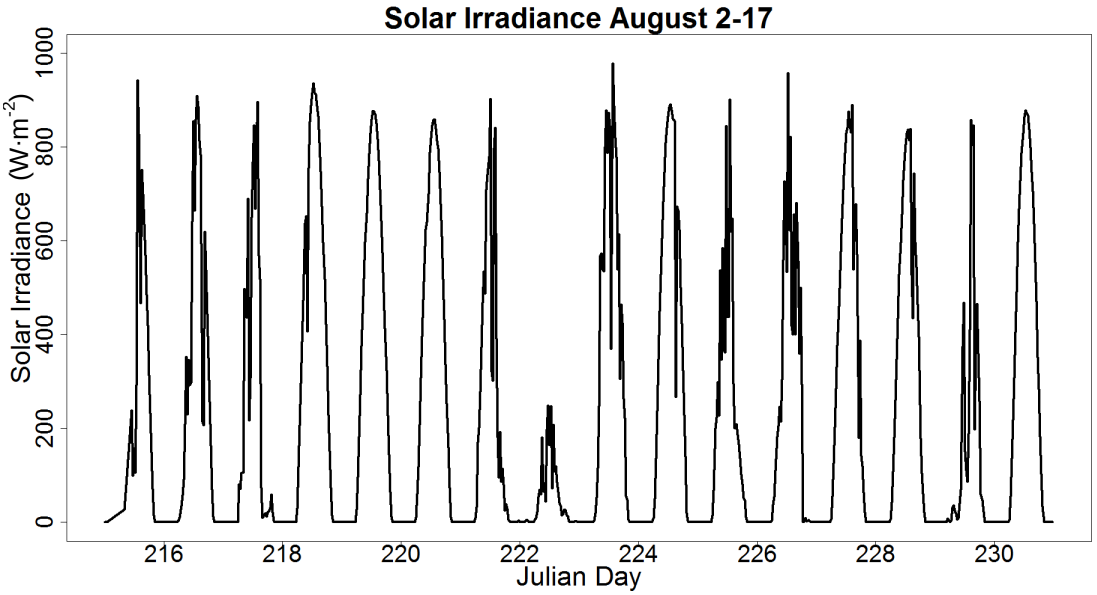

Figure 3.11b. Solar irradiance from the buoy meteorological station from August 2-17, 2012.

days 215-220 showed stable stratification at Station 21, with cold hypolimnetic waters and significant diel heating of the surface waters (>1.5˚C) (Fig. 3.11i). There was evidence of entrainment of hypolimnetic waters into the mixed layer on Julian days 223 to 224. The period at the end of the diel warming signal and the beginning of the cooling of surface waters consistently displayed a correlation with a peak in latent heat flux (Fig. 3.11d). These peaks in latent heat flux were generally short lived, likely coupled with the period

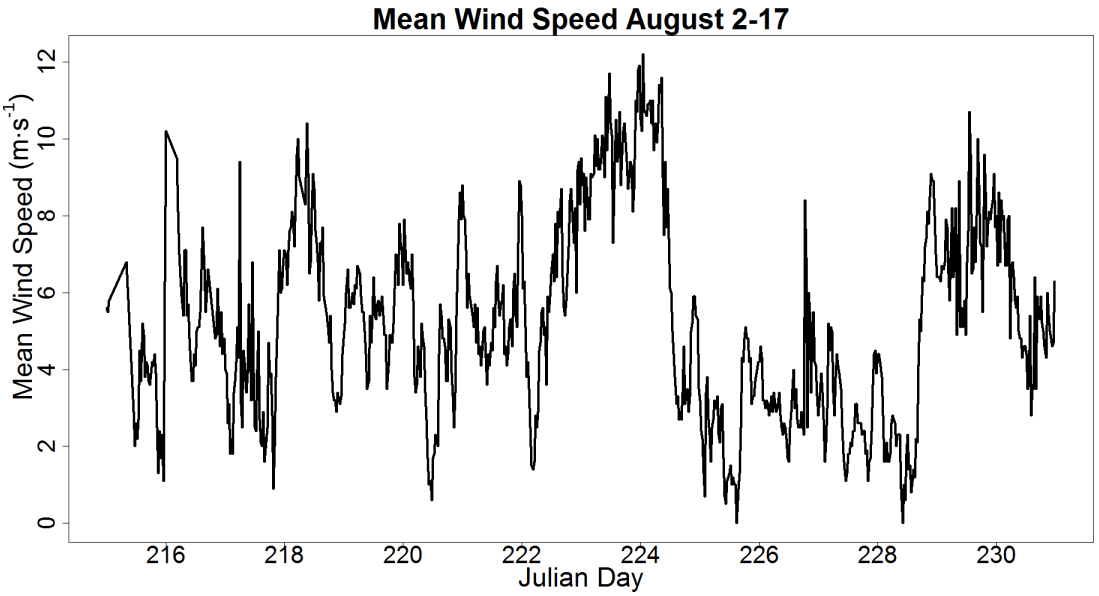

Figure 3.11c. Mean wind speed from the buoy meteorological station from August 2-17, 2012.

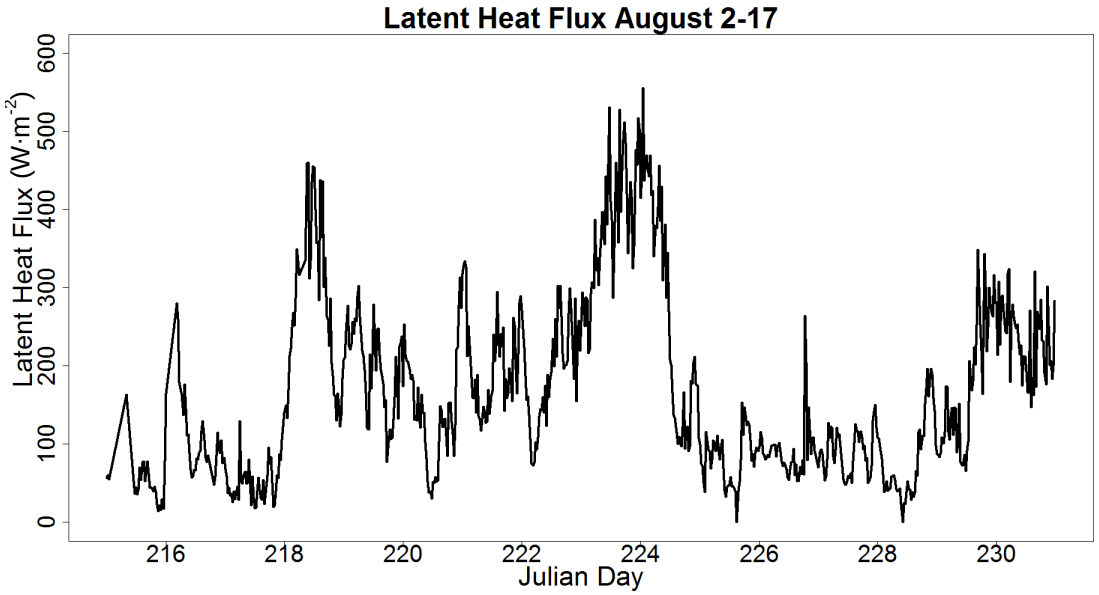

Figure 3.11d. Latent heat flux from August 2-17, 2012.

where heat gained during the day is rapidly lost to the atmosphere via evaporation. As seen with mixing of the water column, these processes tend to occur within an hour window, with the peak in latent heat flux corresponding to a typical drop in surface water temperature of 1˚C within the half-hour period, with the half-hour period generally around 21:00. Maximum surface temperatures typically occurred around 18:00 at shallow stations,

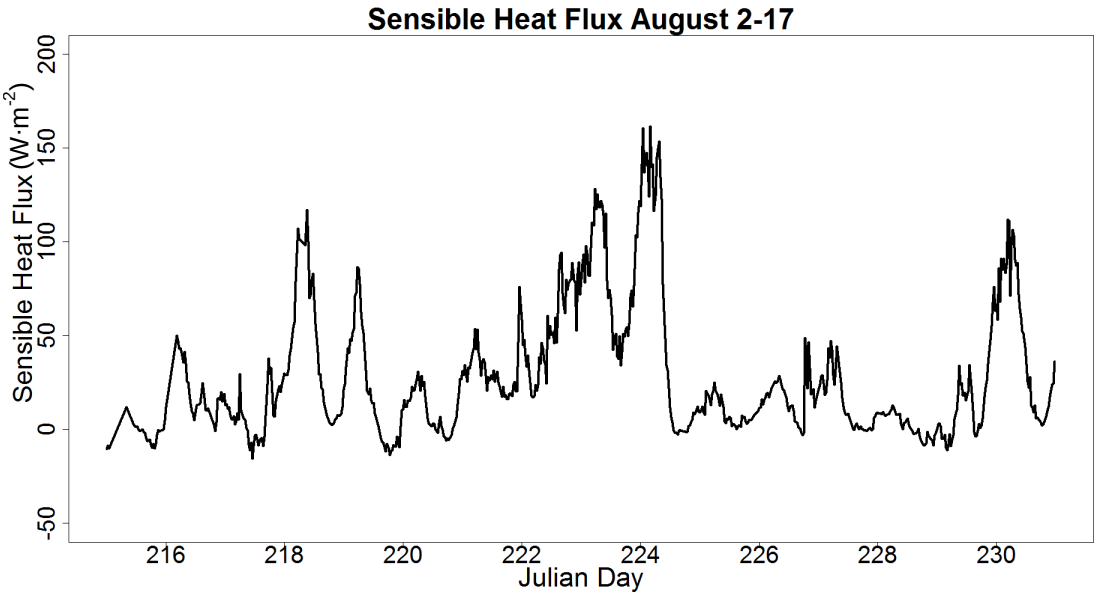

Figure 3.11e. Sensible heat flux from August 2-17, 2012.

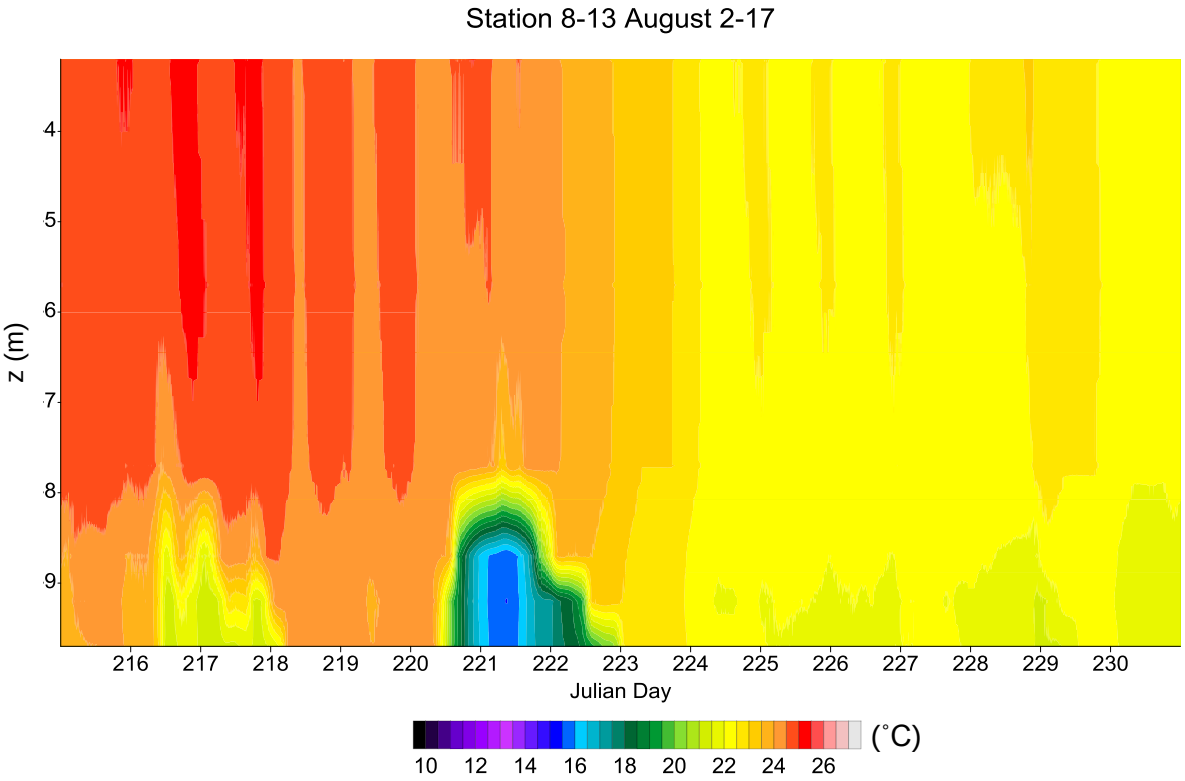

Figure 3.11f. Depth-time temperature plot for Station 8-13 from August 2-17, 2012.

with drops of 3˚C seen in 3.5 hour periods (e.g. Station 8, Julian day 240). Deeper stations (e.g. Station 31) typically experienced maximum surface temperatures between 16:00 and 17:00. These times did not fluctuate significantly between summer months (June, July, and

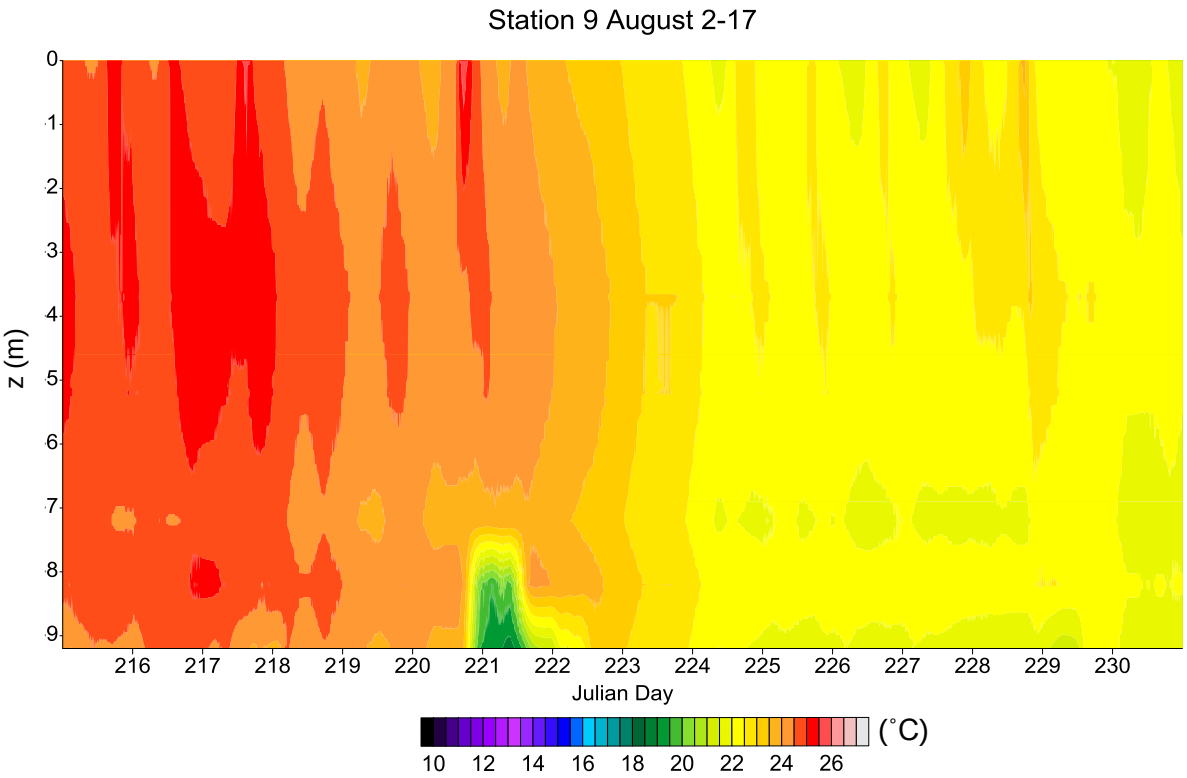

Figure 3.11g. Depth-time temperature plot for Station 9 from August 2-17, 2012.

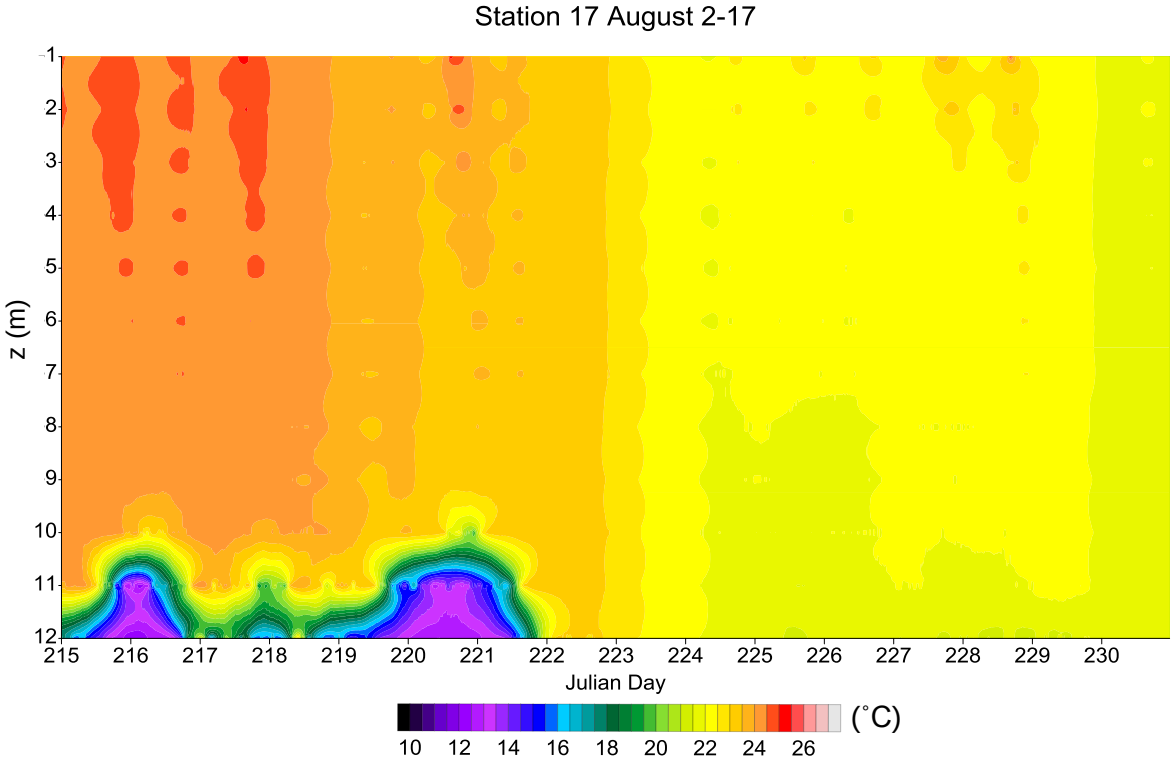

Figure 3.11h. Depth-time temperature plot for Station 17 (buoy) from August 2-17, 2012.

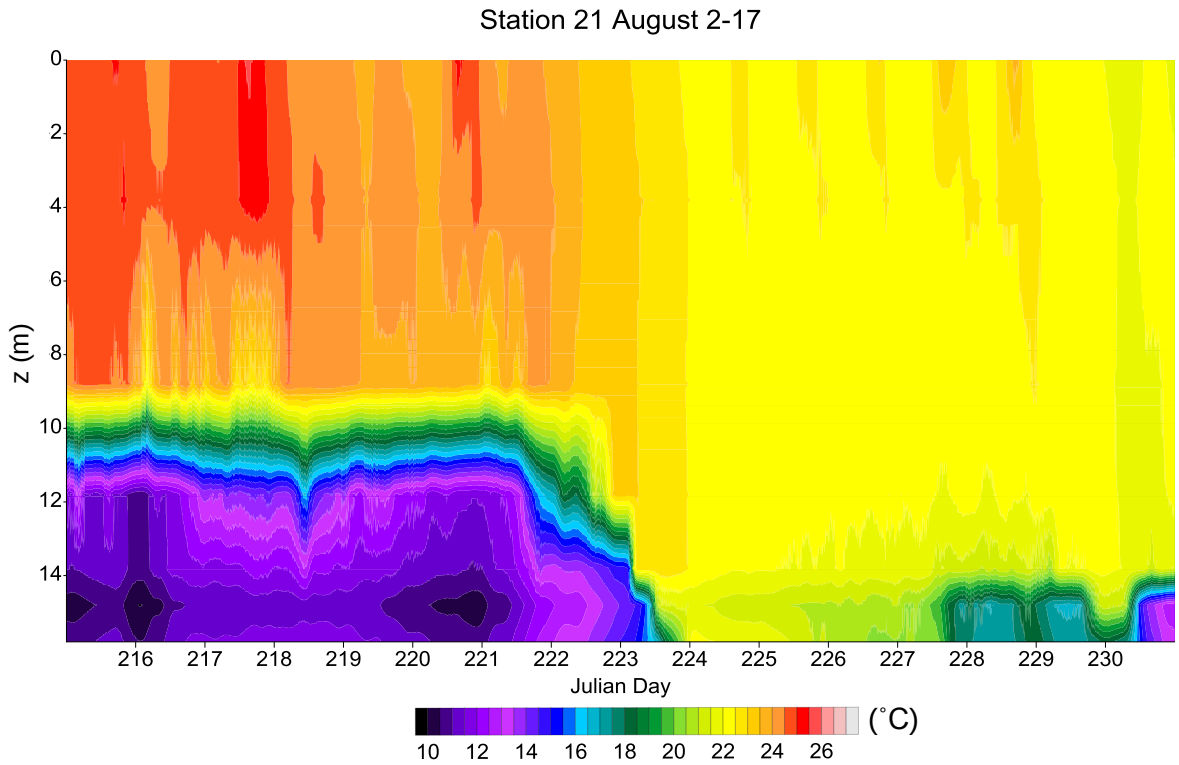

Figure 3. 11i. Depth-time temperature plot for Station 21 from August 2-17, 2012.

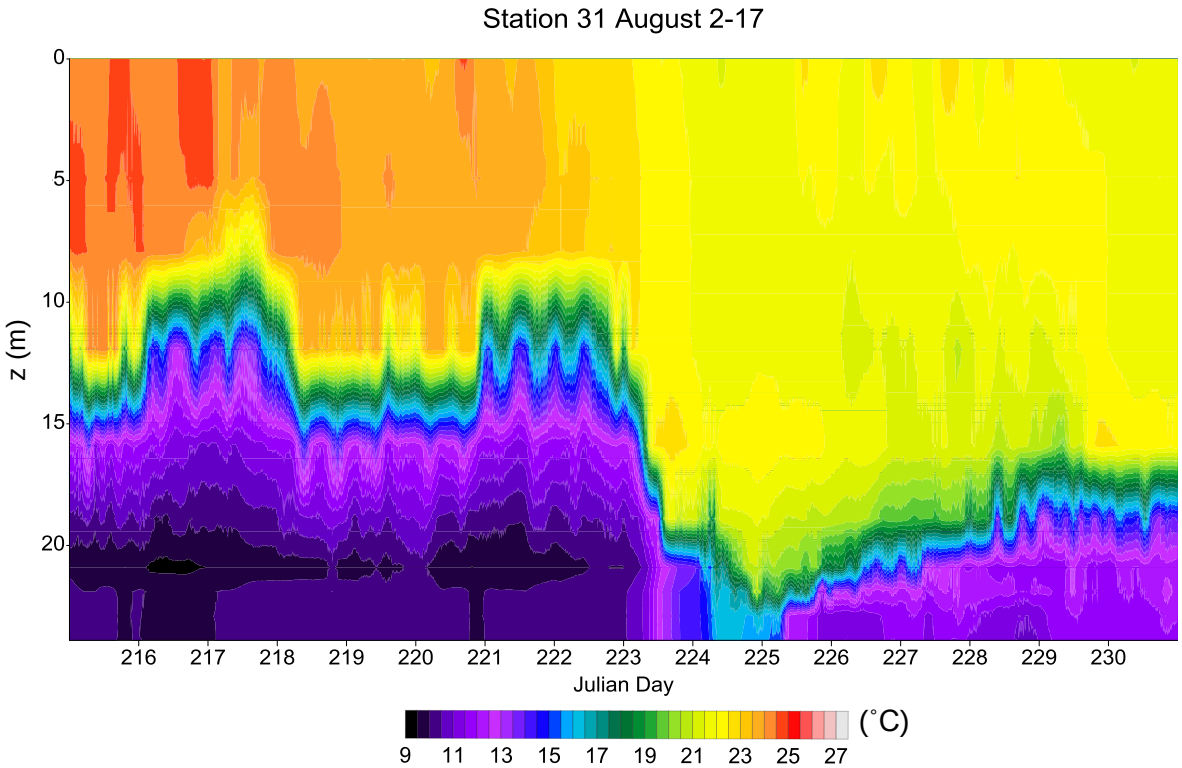

Figure 3.11j. Depth-time temperature plot for Station 31 from August 2-17, 2012.

August). These cycles are consistent after days of high solar irradiance, regardless of the time of year within the study period. Days which experienced variable cloud cover and still displayed a reduced diel warming signal typically exhibited rapid changes but of a smaller magnitude, approximately 0.5˚C within the hour period. These instances also displayed smaller peaks in latent heat flux for the period when compared to days exhibiting stronger diel warming signals. After the period of rapid cooling, surface water typically maintained the same temperature or cooled up to 0.5˚C, between 0:00 and 6:00.

Sensible heat flux was consistently negative during diel warming periods, as the surface waters absorbed solar irradiance more efficiently than the overlying air and thus heated at a quicker rate. Within these instances, sensible heat flux was typically small (<50 $W \cdot m^{-2}$). Sensible heat flux was significantly greater during evening cooling periods (>100 $W \cdot m^{-2}$), correlating with peaks in latent heat flux (Fig. 3.11e). Air temperatures cool quickly once the sun has set, while water retains heat due to the much higher specific heat of water. Thus, while latent heat flux is high due to evaporation of water, the direct heat transfer between water molecules and air molecules during these cooling periods is also high. However, sensible heat flux tends to be approximately one-fourth or less of the value of the latent heat flux during these periods (Fig. 3.11d-e).

Prior to seasonally permanent isothermal conditions, the contributing factors to breakdown of stratification and the onset of isothermal conditions are evident (Fig. 3.12a-i). In September, air temperatures were cooler than water temperatures, resulting in consistent loss of heat (Fig. 3.12a). Surface waters still showed a diel warming signal, but the amount of energy added to the water column by solar irradiance was approaching the point where it was offset by the latent, to the greatest extent, and sensible heat fluxes (Fig. 3.12d-e). Cold water intrusions continued to enter the southern bay, as they do year-round, resulting in two contributing cooling effects. Station 8-13, for a brief period beginning

before Julian day 255 and lasting to Julian day 257, displayed a warm water mass with cooler water both above and below it, with temperature differences >1˚C (Fig. 3.12f). While this is likely not typical, it also displays how mixing between water masses takes time. Ultimately entrainment of cooler bottom waters and the constant loss of heat at the water surface can, at times, rapidly lead to isothermal conditions.

Over the same period, Station 21 maintained stratification, despite a cooling of the water column (Fig. 3.12h). However, Julian day 261 exhibited both cloud cover (and thus no diel warming) and a significant decrease in air temperature (a drop of over 10˚C in 1 day) (Fig. 3.12b and 3.12a, respectively). Coupled with strong winds and the cold water intrusion, much of the cold water is entrained into the overlying waters, resulting in the top of the cold water mass occurring at a depth of approximately 7 meters to a depth of nearly 13 meters and the overlying waters cooling by >1˚C in one day (Fig. 3.12c and 3.12h, respectively). The winds during this period are stronger and more sustained than other periods throughout the summer. As expected, September shows stronger and more sustained winds throughout than July and August.

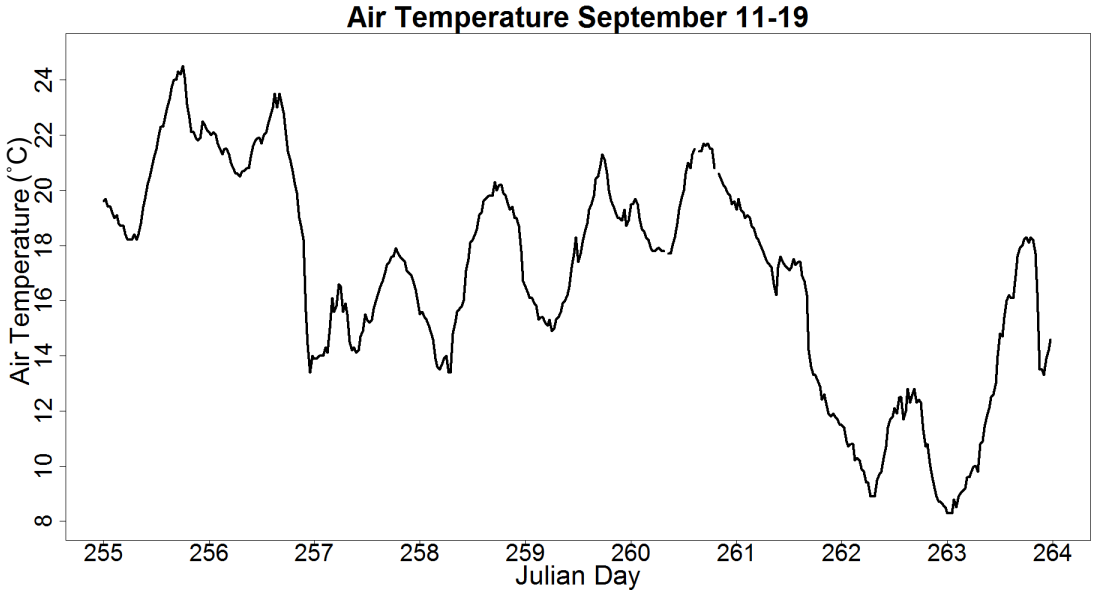

Figure 3.12a. Air temperature from the buoy meteorological station from September 11-19, 2012.

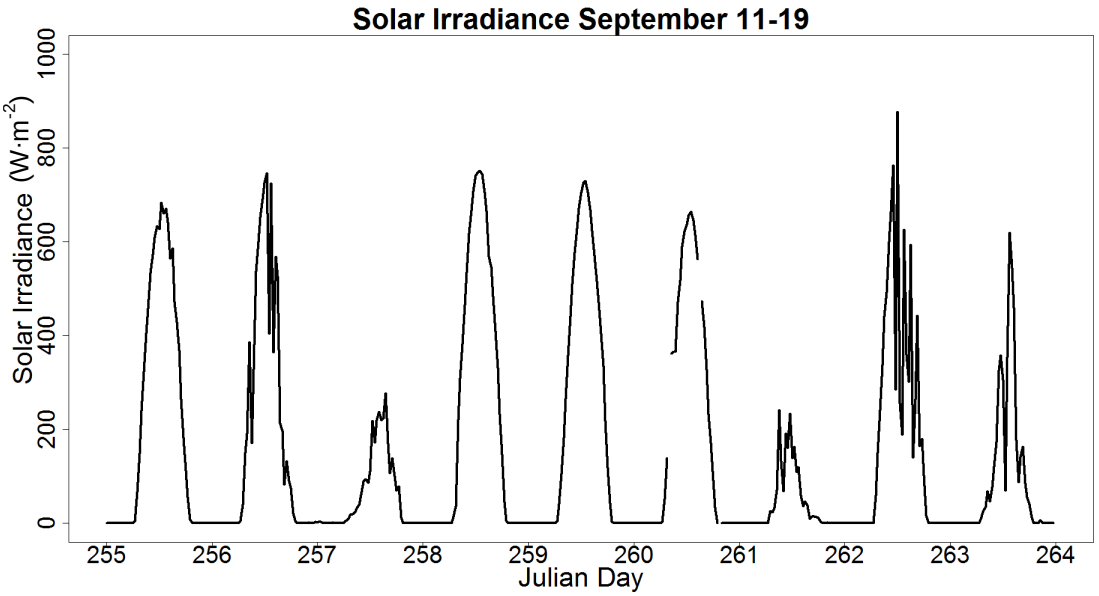

Figure 3.12b. Solar irradiance from the buoy meteorological station from September 11-19, 2012.

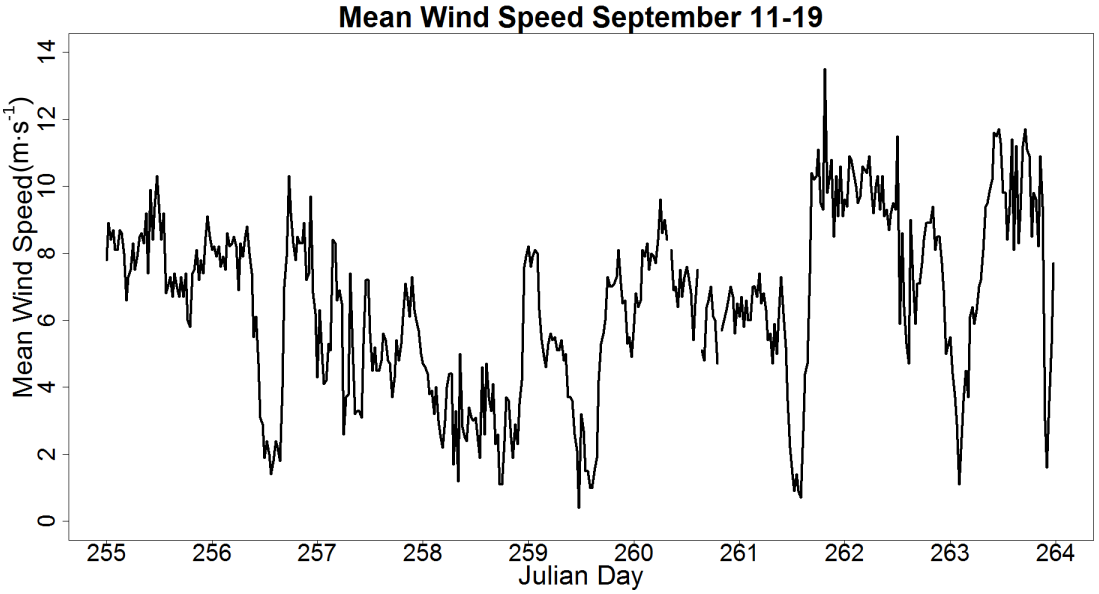

Figure 3.12c. Mean wind speed from the buoy meteorological station from September 11-19, 2012.

3.7 Daily Surface and Sub-surface Temperature Change

The differences between the maximum and minimum surface water temperatures were calculated for each day (Table 4; Fig. 3.13a). The maximum surface water temperature occurred around 16:00 and the minimum surface water temperature occurred around 5:00-6:00 across all data sets. Station 8 showed significantly higher warming trends when compared to the other stations (Fig. 3.13a). However, the significance cannot be attributed

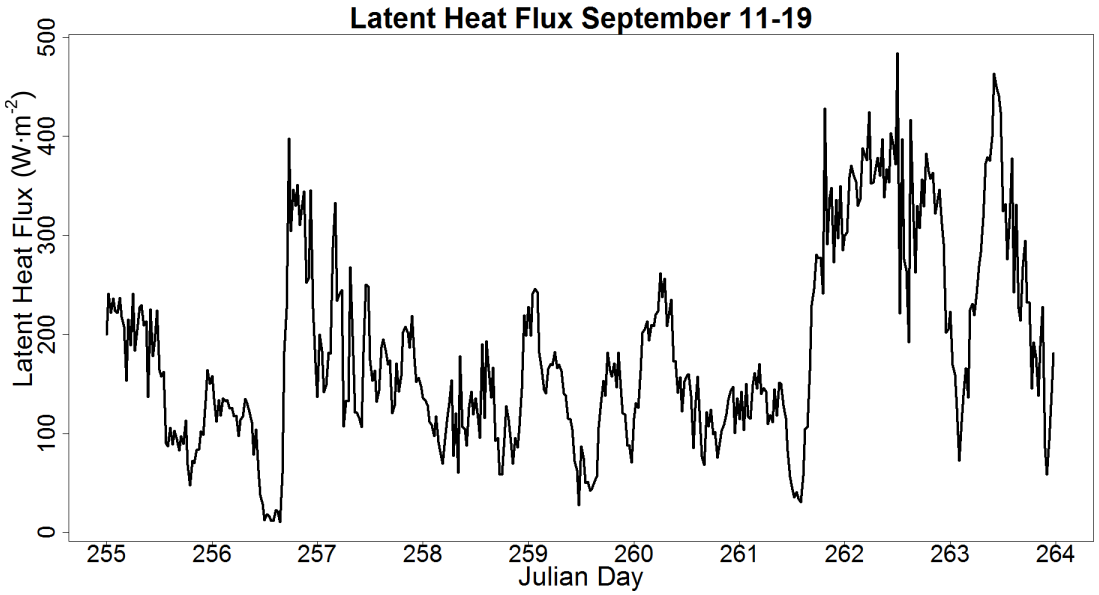

Figure 3.12d. Latent heat flux from September 11-19, 2012.

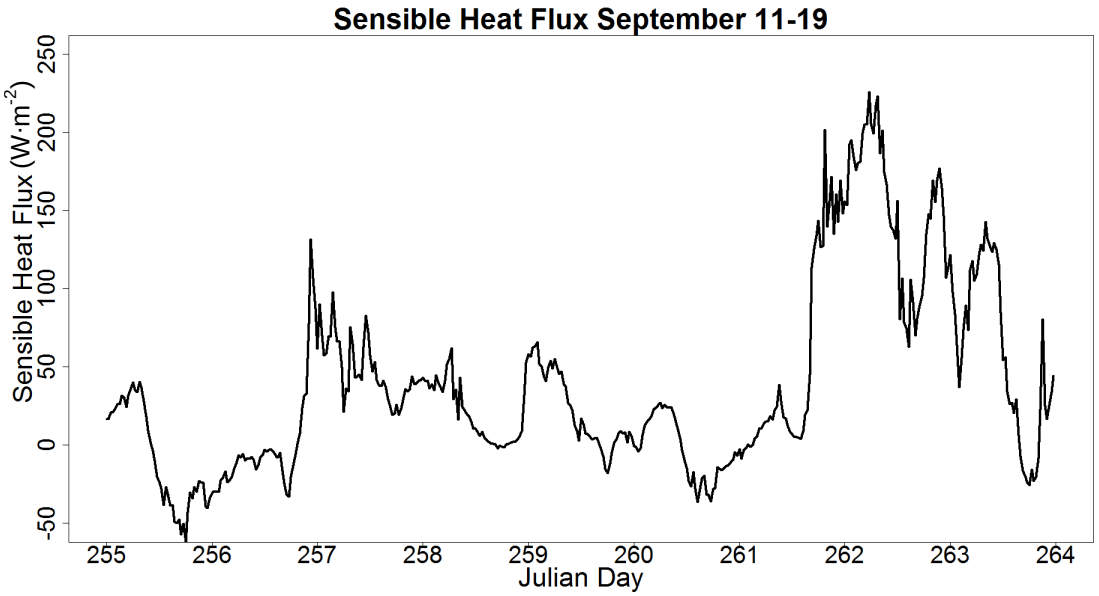

Figure 3.12e. Sensible heat flux from September 11-19, 2012.

to water clarity, as Station 8 and 9 displayed similar k_d values across sampling periods (Table 3.2). While the reason for the difference between Station 8 and the other stations cannot be determined, the cause in daily differences was investigated by comparing a short term data set for the period Julian day 208 to 222 (Fig. 3.13b). This period was chosen as it includes the mooring at Chambers Island West, which serves as a baseline for water clarity

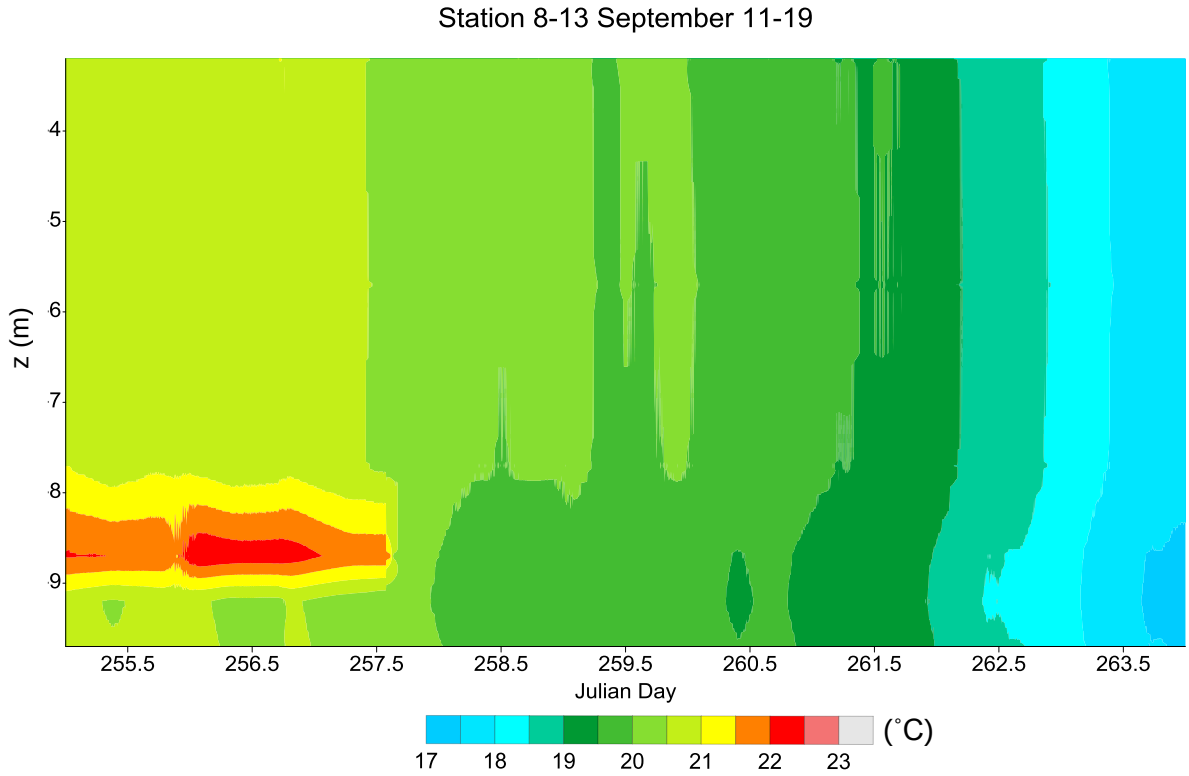

Figure 3.12f. Depth-time temperature plot for Station 8-13 from September 11-19, 2012.

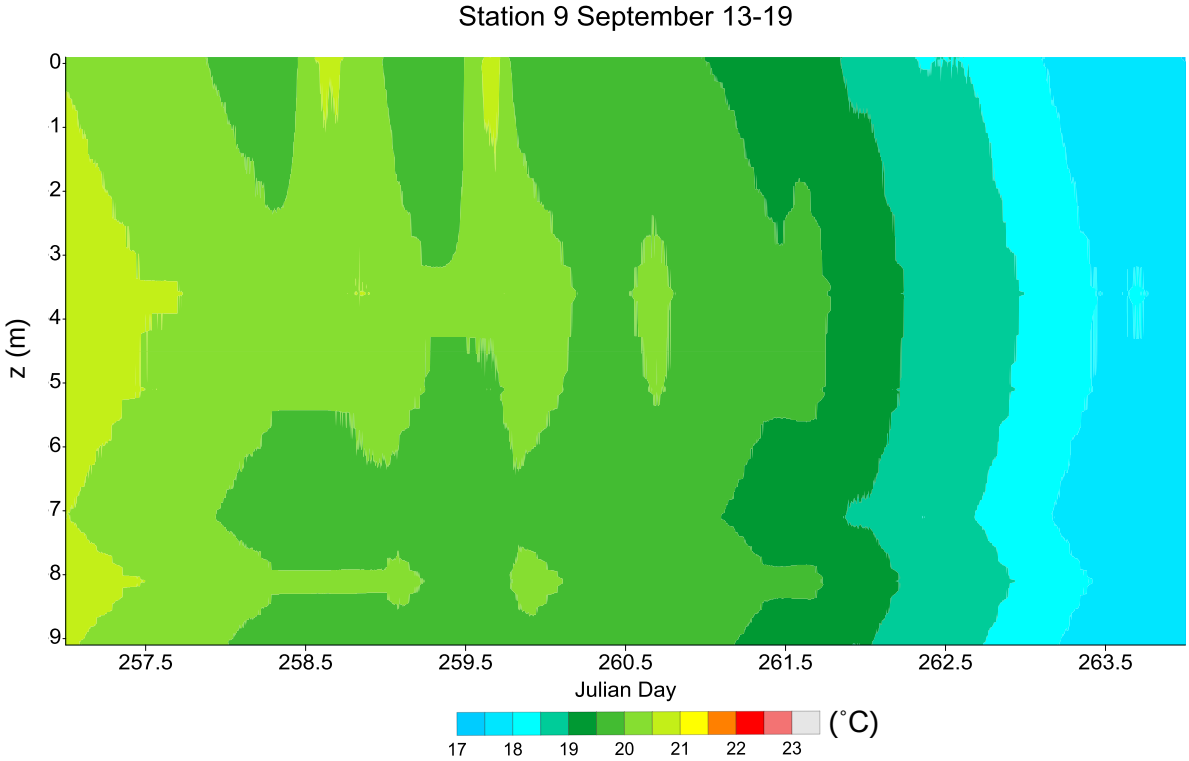

Figure 3.12g. Depth-time temperature plot for Station 9 from September 11-19, 2012.

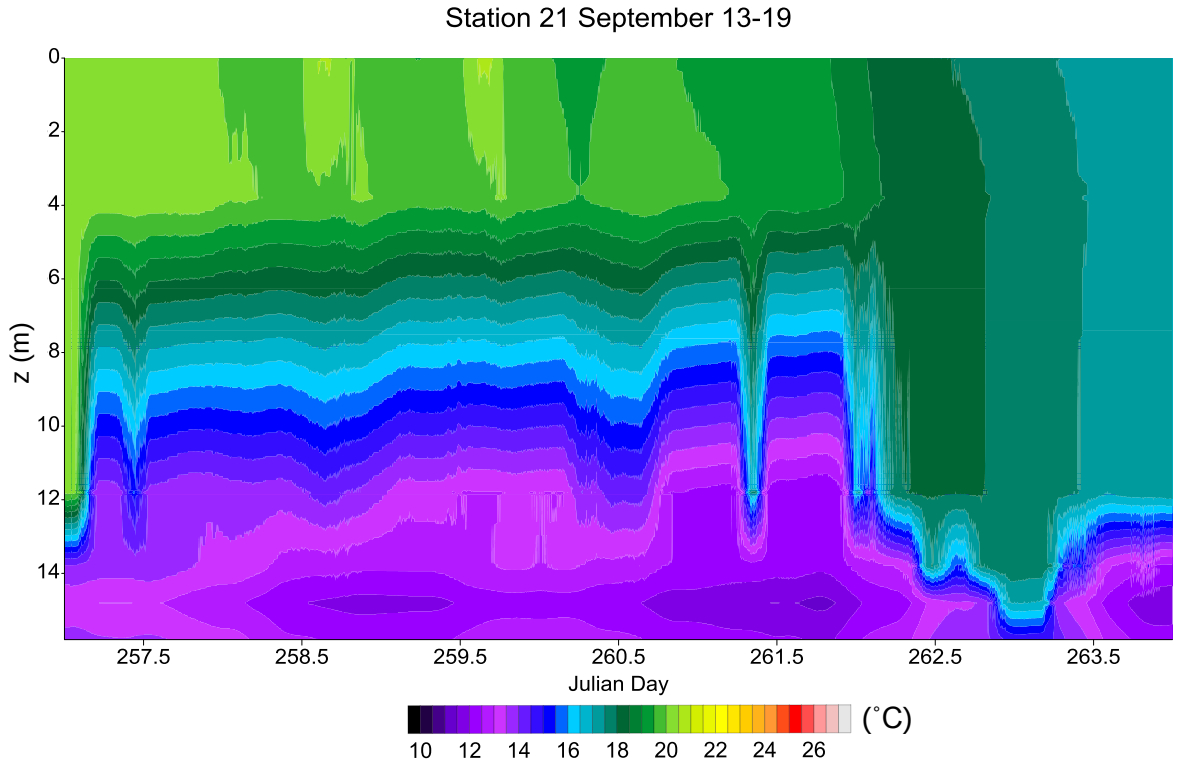

Figure 3.12h. Depth-time temperature plot for Station 21 from September 11-19, 2012.

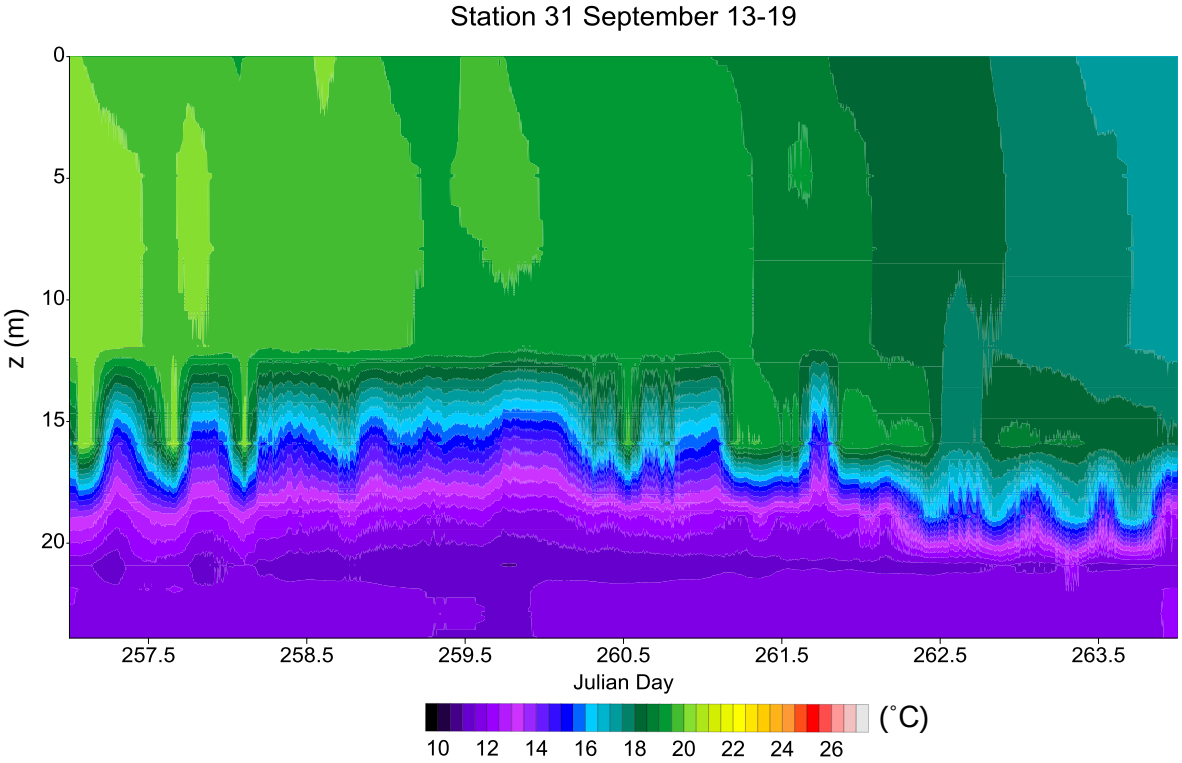

Figure 3.12i. Depth-time temperature plot for Station 31 from September 11-19, 2012.

Table 3.4. Examples of minimum and maximum sea surface temperatures (SST) for particular days at Stations 8, 9, and 31.

Julian day	Station	Min. SST (˚C)	Max. SST (˚C)	Difference (˚C)
197	8	25.016	29.414	4.398
201	8	23.93	25.234	1.304
215	31	24.219	24.871	0.652
216	31	24.122	24.798	0.676
217	9	24.702	25.866	1.164
220	9	23.833	25.914	2.081
220	31	23.4	24.677	1.277
225	9	22.011	22.992	0.981
226	9	21.867	22.872	1.005
227	9	21.867	23.593	1.726
228	9	22.298	24.002	3.704
230	9	21.7	22.178	0.478
238	8	21.915	25.817	3.902
238	9	21.772	24.122	2.35
238	31	21.294	23.28	1.986
239	9	22.13	22.25	0.12
240	8	22.058	26.109	4.051
240	9	21.915	24.171	2.256
240	31	21.652	23.256	1.604
242	31	20.889	22.513	1.624

as it displayed the smallest k_d value of all sampled stations (Table 3.2). Over this period, there was a period of five days which primarily displayed a warming trend (except for one day in the five) and a period of several days following this period where diel warming across all stations was smaller (Fig. 3.13c). Incident solar irradiance was consistent and did not adequately explain the variance (Fig. 3.13e). Air temperature displayed an inverse relationship from what would be expected, as the warmest period of air temperatures and the period for which it would be expected that the water surface was insulated and warmed the most correlates with the period for which surface water temperatures showed minimal surface warming (Fig. 3.13d). During this period, mean wind speeds were slightly stronger

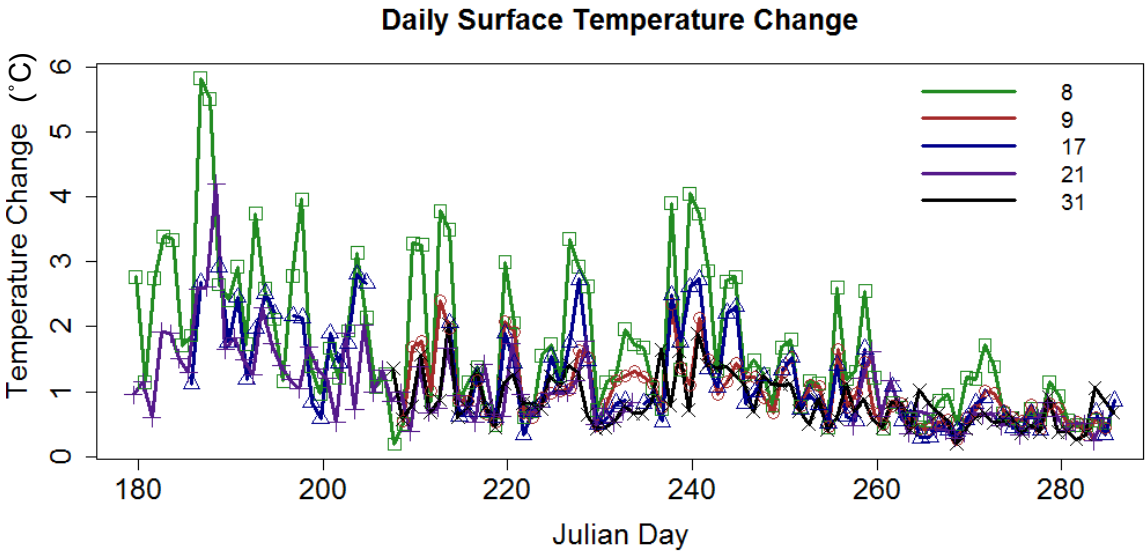

Figure 3.13a. Difference between the maximum and minimum surface temperatures by site and day.

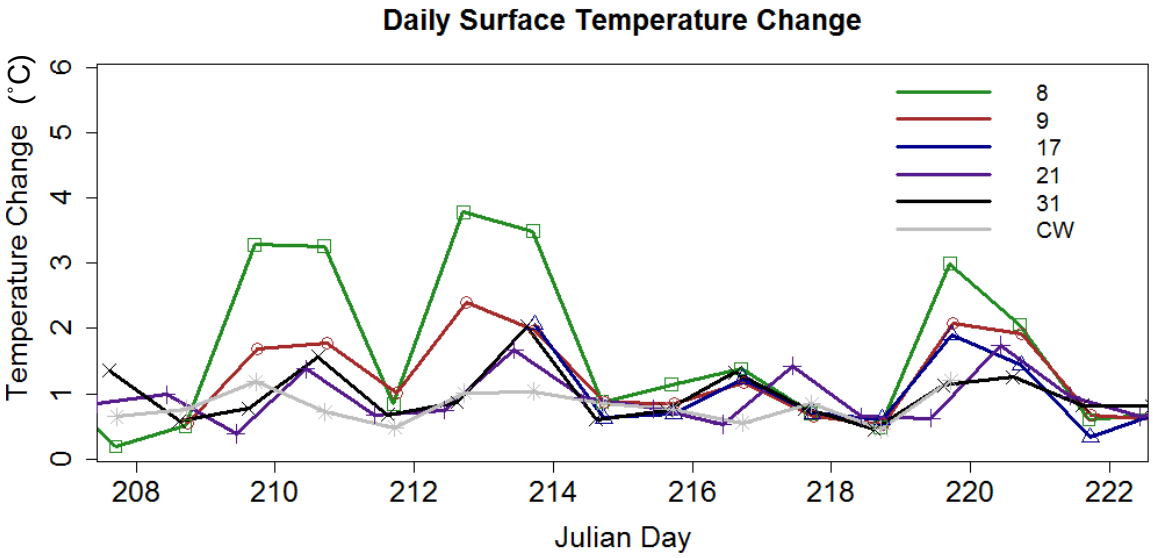

Figure 3.13b. Difference between the minimum and maximum surface temperatures for site and day for the period Julian day 208 to 222.

and sustained, with several mean wind speeds over 8 $m \cdot s^{-1}$ (Fig. 3.13f). This did not indicate much. However, when considering the sensible and latent heat fluxes over this period, both flux values gradually rose beginning on Julian day 215, when the minimal diel surface warming period began (Fig. 3.13g and 3.13h, respectively). The flux values peaked on Julian

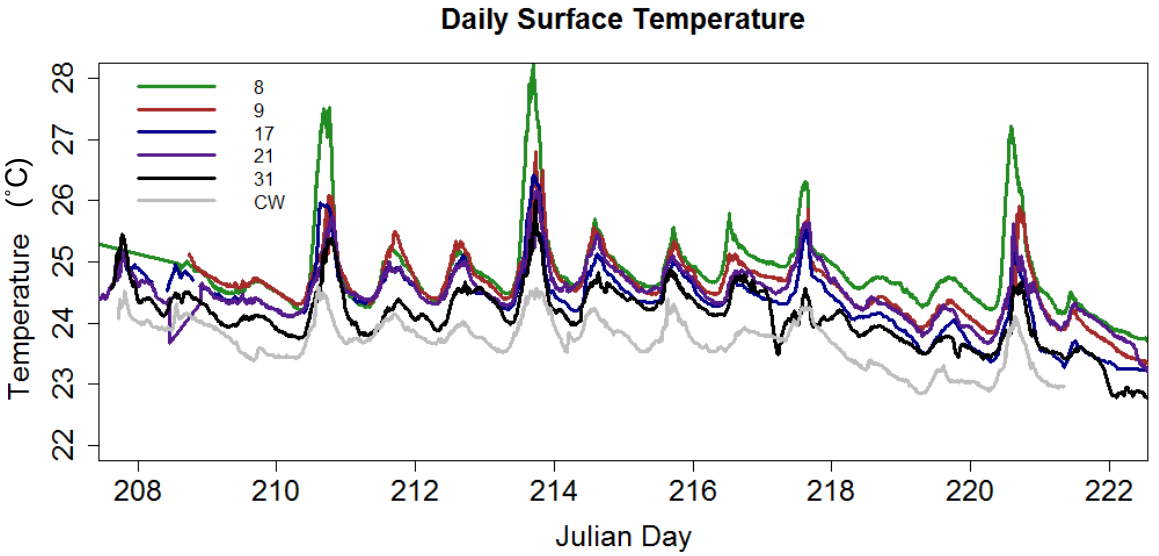

Figure 3.13c. Surface temperature for Stations 8, 9, 17, 21, 31 and Chambers West for the period Julian day 208 to 222.

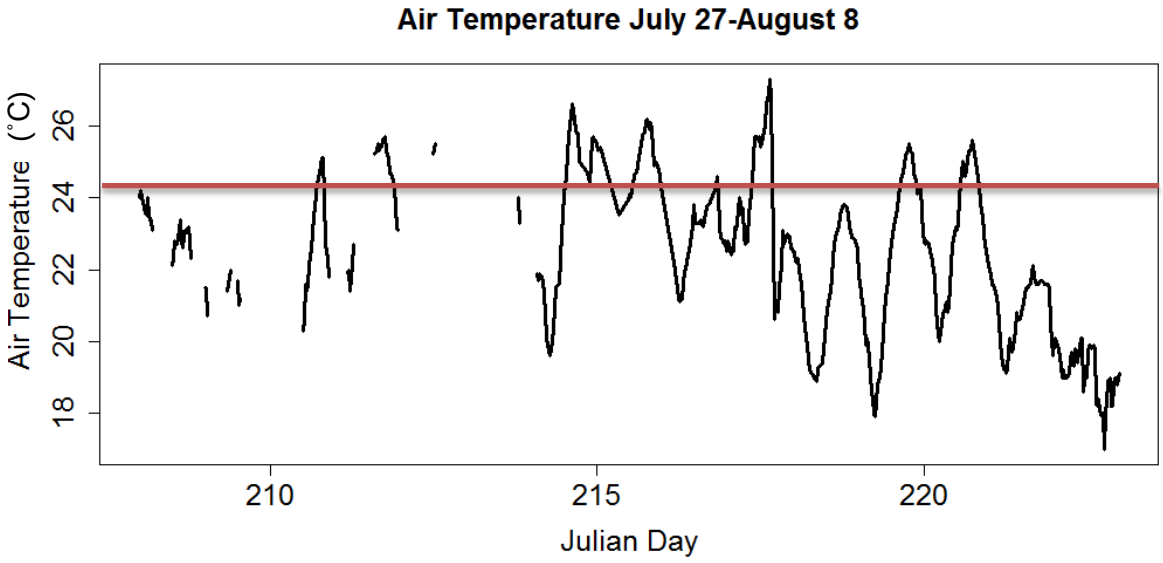

Figure 3.13d. Air temperature from the meteorological station at Station 17 (buoy) for the period Julian day 208 to 222. The red line indicates the average surface water temperature from all stations included in the above graph over the period.

day 219, with diel surface warming increasing on Julian day 220. This indicates that the wind played a role in the thermal structure prior to this period, mixing warmer surface waters down into the water column, allowing the entire water column to absorb more

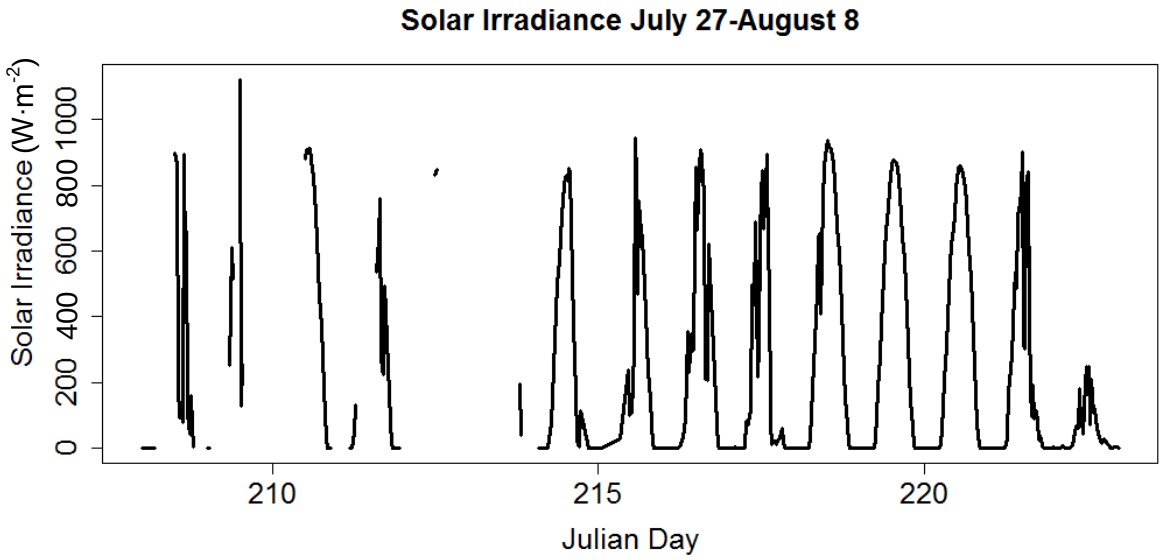

Figure 3.13e. Solar irradiance from the meteorological station at Station 17 (buoy) for the period Julian day 208 to 222.

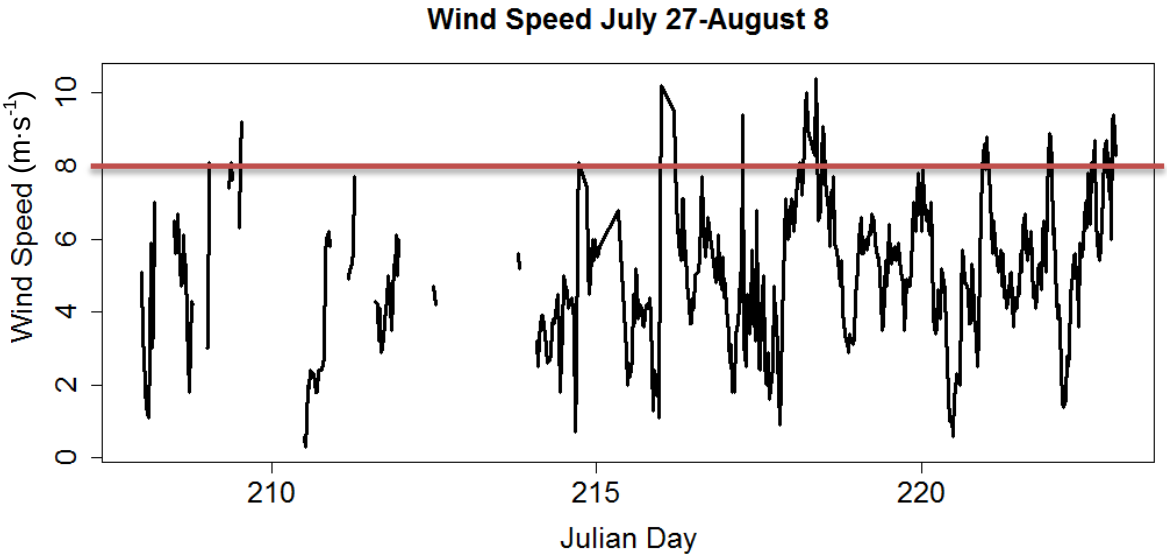

Figure 3.13f. Mean wind speed from the meteorological station at Station 17 (buoy) for the period Julian day 208 to 222. The red line indicates speeds above 8 $m \cdot s^{-1}$, the speed at which wind has been found to be the dominant variable dictating the depth of the mixed layer (Simpson and Dickey 1981; others).

energy. The average surface water temperature over this period (indicated by the red line) is much above the average air temperature for the period (Fig. 3.13d). Thus, it was expected that there would be a transfer of heat out of the water and into the atmosphere. The result

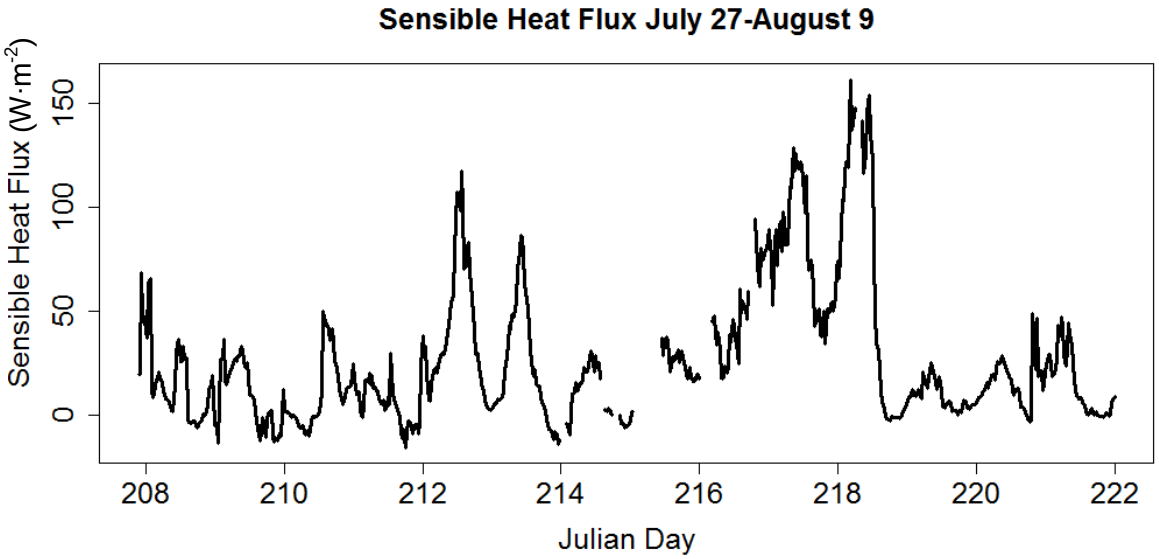

Figure 3.13g. Sensible heat flux for the period Julian day 208 to 222.

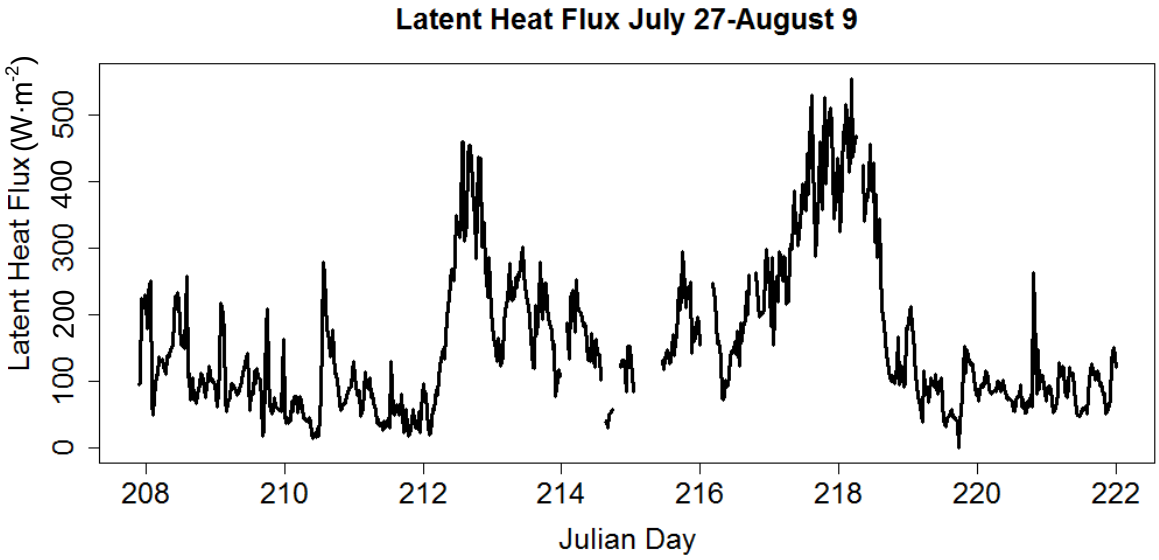

Figure 3.13h. Latent heat flux for the period Julian day 208 to 222.

was cooler surface waters as well as wind mixing providing a reduced diel warming signal in the surface waters.

To better determine whether water clarity played a role, the sub-surface heating was graphed over the study period (Fig. 3.13i). While Station 31 occasionally exhibits

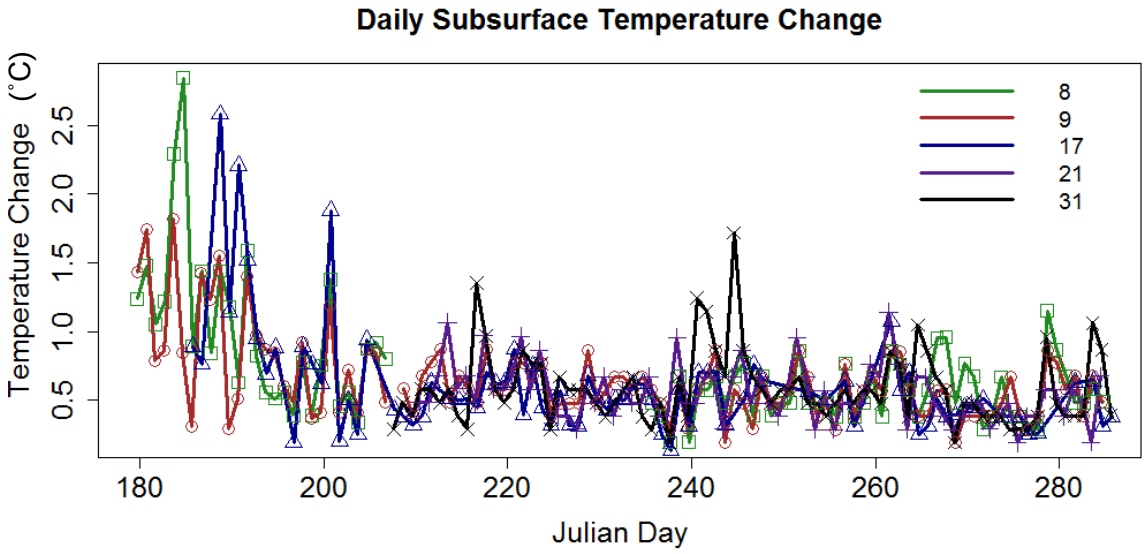

Figure 3.13i. Difference between the maximum and minimum sub-surface temperatures by site and day, using the first HOBO logger on the mooring line after the surface logger.

expected behavior with enhanced sub-surface heating in relation to other stations, this behavior is infrequent and overall the data show no significant trends.

3.8 Bottom Water Temperatures

Tracking the pathway of cold water intrusions can be done by observing when each station reaches a minimum temperature or by tracking when each station reaches the same temperature. When tracking cold water intrusions in such a way, two trends become evident. The first is that bottom temperatures cool first at northerly stations, following a trend of Station 31, Station 21, Station 17, and Station 13(Fig. 3.14a-c). This, however, is where the second trend becomes evident. The next station to reach a cooler temperature (when considering waters of the same temperature or warmer) is Station 13-19, which is the shallowest mooring deployed and is located along the western shore. From this point, cold water intrusions track from western stations to eastern stations, following a path of Station 13-19, Station 8-13, Station 9, and Station 8. A schematic of this process is illustrated in Appendix E.

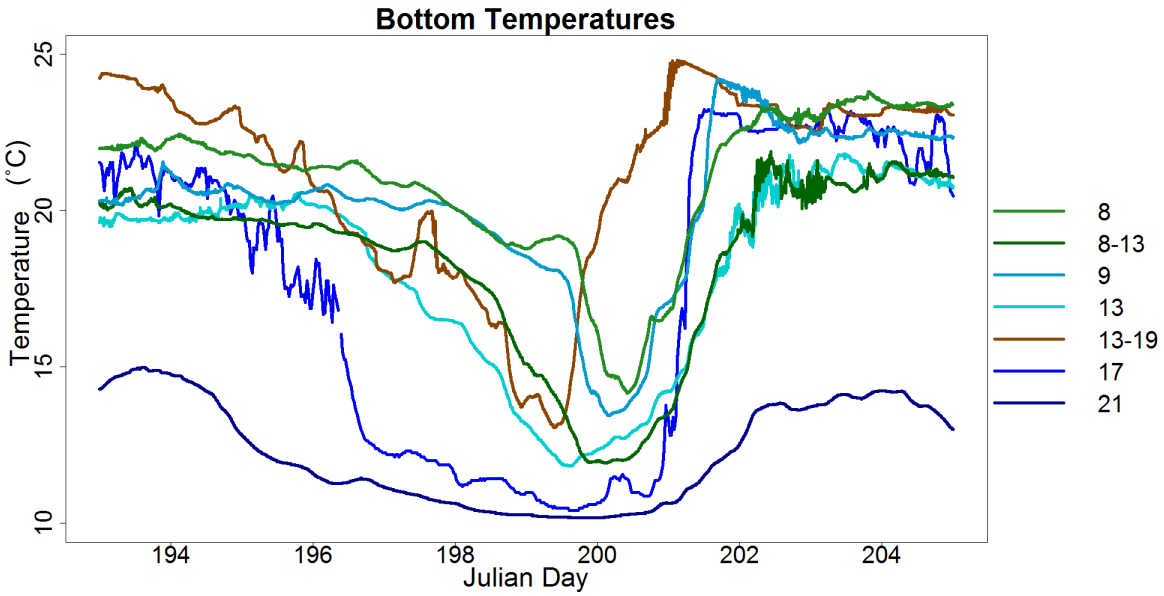

Figure 3.14a. Bottom water temperatures for stations 21, 17, 13, 13-19, 8-13, 9, 8 for the period Julian day 193 to 205.

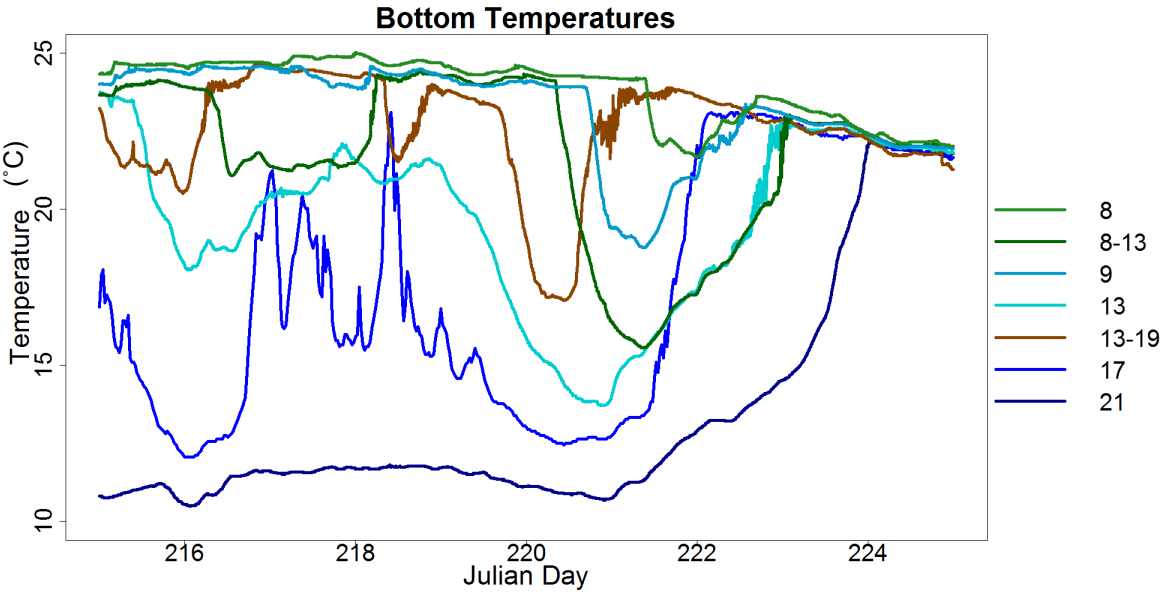

Figure 3.14b. Bottom water temperatures for stations 21, 17, 13, 13-19, 8-13, 9, 8 for the period Julian day 215 to 225.

Between the two methods, different results are reached. Station 13-19 shows, at times, that it reaches the minimum temperature prior to Station 13. When also considering when stations reach the same temperature, it becomes evident that the cold water intrusion tracks along the central axis of the bay, following the isobathic plateaus within the bay

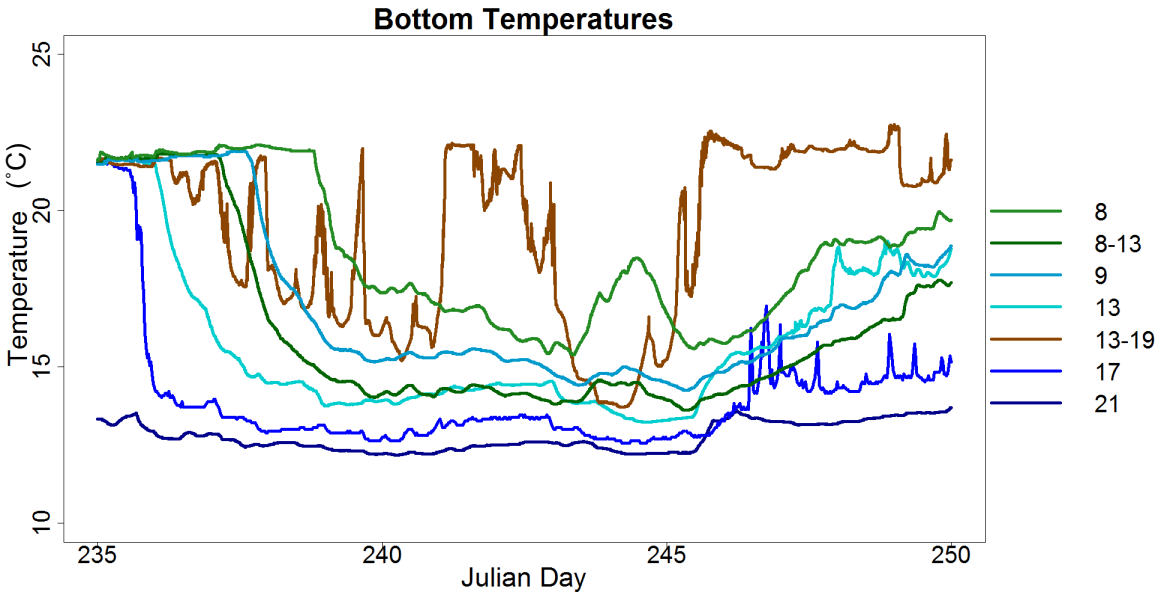

Figure 3.14c. Bottom water temperatures for stations 21, 17, 13, 13-19, 8-13, 9, 8 for the period Julian day 235 to 250.

where changes in depth are gradual. As the cold water intrudes into the lower bay, it pushes cool, hypolimnetic mid-bay waters up into shallower isobaths, similar to a wave crashing onto a beach. This is revealed by the difference in temperatures across different regions, including Station 13-19 and Station 13 exhibiting similar minimum temperatures of approximately 1˚C warmer than Stations 17 and 21 during the period Julian day 193 to 205, and Station 8-13 and Station 9 exhibiting temperatures approximately 2˚C warmer than Stations 17 and 21 over the same period (Fig. 3.14a). Station 8, the eastern-most station and the second shallowest exhibits a temperature that is 2.5˚C warmer than Station 17 and 21 over this period.

Figures 3.14b and 3.14c display similar pathways of cold water masses across the stations. These findings agree well with previous studies suggesting a pathway of cooler Lake Michigan waters along the western shore of Green Bay (Kennedy 1982; Miller and Saylor 1985; Lathrop et al. 1990). This study shows the pathway of the cold water mass in higher detail. It also suggests that considerable mixing and displacement of mid-bay hypolimnetic waters occurs, a topic that requires further study in the future. These

processes result in significant ramifications for lower Green Bay oxygen dynamics, with consequences tracking up the food web (Valenta et al. 2012).

Chapter 4: Discussion and Conclusions

4.1 Discussion

Temperature moorings placed throughout southern Green Bay for the summer and early fall of 2012 verified trends that other researchers have found in the past – namely, that Green Bay stratification becomes increasingly unstable south of Chambers Island, with cold water intrusions playing a large part in both the re-stratification of the southerly region as well as gradual and repeated cooling of the water column throughout the summer period (Kennedy 1982; Miller and Saylor 1985; Gottlieb et al. 1990; Hamidi et al, in prep). The origin of these cold water intrusions could not be explicitly determined from this study. However, past studies have suggested that the cold water originates from Lake Michigan proper, with the water which intrudes into the southern bay either Lake Michigan water or hypolimnetic waters from northern Green Bay (Gottlieb et al. 1990). These cold water intrusions play a crucial role in the cooling of southern Green Bay throughout the summer, with net advection several times larger than net air-sea heat flux at times for southerly stations. While the cold water masses are infrequent, they serve as a reset button for the system, reinvigorating stratification in waters that become increasingly well-mixed through the summer months. Thus, the cold water masses significantly impact the thermal structure for short periods of time, resulting in increased hypoxia and local anoxic events throughout the summer due to high sediment oxygen demand and a water mass separated from atmospheric re-oxygenation for days and even weeks (Valenta et al. 2012).

While these cold water masses were common throughout the season at more northerly sites (e.g. Station 31), the size of these masses, as well as their presence in more southerly stations (e.g. Station 8-13), followed a distinct trend of northerly and westerly stations being impacted prior to southerly and easterly stations. This agrees well with previous work while also furthering our understanding of the dynamics of the distinct

water masses within the system, namely resident Green Bay water, incoming Fox River water, and cold, hypolimnetic intrusions (Kennedy 1982; Miller and Saylor 1985; Klump et al. 1997). Additionally, k_d values estimated from profile data and interpolated spatially across the bay indicate trends in water clarity that follow temperature observations, namely that more easterly stations exhibit higher k_d values. This likely represents Fox River water and nutrient-enhanced bay waters, where productivity is much higher and resultant algal growth reacts accordingly. This also agrees well with previous studies that have assessed the general and historic trends of a distinct trophic gradient in the bay (Sager and Richman 1991; Klump et al. 1997; Klump et al. 2009).

There is a large amount of movement between bottom waters throughout Green Bay. Cold water intrusions seen within the hypolimnion at mid-bay sites correspond to a general cooling of waters in more southerly sites. However, the cooling is to a much greater degree at more northern sites, suggesting that the warmer hypolimnion water of mid-bay sites is being displaced by cold water intrusions from the upper bay, and this displaced water then migrates to more southerly stations. During this migration, the cold water intrusions are slowly eroded away and typically become fully mixed into the water column at southerly stations during periods of high winds or large convective mixing. By tracking individual cold water intrusions, the general path of this migration and the origin of the water present (based on temperature) can be inferred. Based on the findings of this study, cold water intrusions and the water displaced by these water masses follows a track that is defined by the morphometry and seasonal currents of Green Bay coupled with the inflow of Fox River water. The primary flow of cold water occurs via the passage west of Chambers Island, with the bulk of the water flowing down the central depth contours of the bay. By the curvature of the bay itself, and by the direction of the depth contours (southwesterly), the cold water follows a path that also corresponds to the dominant currents observed in prior

studies (Kennedy 1982; Miller and Saylor 1985). In addition, the dominant track of Fox River water is along the eastern shoreline of southern Green Bay (Lathrop et al. 1990). The extent to which the cold water intrusions themselves affect the dominant currents observed is unknown, but a theoretical approach suggests that the morphometry coupled with meteorological forcing is the primary reason for the observed path of the cold water masses.

Entrainment of cold bottom waters and cooling of surface waters occurred frequently and was correlated with above average wind speeds (>5 $m \cdot s^{-1}$). Typically, a cooling of air temperatures was also observed and all-sky conditions were present a day before mixing. When clear-sky conditions were present during cooling and mixing periods, winds were typically higher (>10 $m \cdot s^{-1}$).

Clear-sky conditions resulted in diel warming, with peak surface temperatures lagging peak incident irradiance by approximately four hours. While warming signals were stronger at more southerly, and turbid, sites, the warming seen between southerly sites was not consistent. Past studies have found significant changes in the depth of the thermocline in small lakes due to a decrease in water clarity and an increase in CDOM (Fee et al. 1996; Perez-Fuentaja et al. 1999; Gunn et al. 2001). However, small lakes carry much stronger signals due to reduced fetch and effect of wind on the physics of the system; thus, water clarity plays a stronger role in the thermal structure of those systems. Additionally, these studies rely upon long-term data sets where clear changes are seen and correlations are more easily drawn between variables and observed changes. Dynamic systems such as Green Bay experience a multitude of factors which affect the physics of the system, from small scale effects including water clarity (despite a largely unknown effect) to large scale effects including wind and internal seiches. Oceanic studies have found water clarity to play a significant role in the distribution of heat and mean annual sea surface temperatures, with

modeling studies observing abnormal subsurface heating when light extinction is contingent only on the interactions of pure water with light (Simpson and Dickey 1981; Kara et al. 2005; Morel et al. 2007). These systems also have a multitude of physical forcing variables and have shown somewhat inconsistent results as model complexity has increased, perhaps suggesting the complexity of feedbacks within these systems (Gnanadesikan and Anderson 2009). While the system of scale suggests that, due to the size, the forcing of oceanic environments is more consistent and, perhaps, more predictable (e.g. currents), research on lakes across size ranges has tended to ignore oceanic studies on water clarity and resultant thermal structure. The common thought is that meteorological forcing variables play a larger role in the thermal structure to such an extent that water clarity can no longer play a role (Fee et al. 1996; King et al. 1999a). While no definitive results were found between water clarity and thermal structure of the water column, or on diel surface warming signals, the findings do suggest that there is significant complexity that requires further analysis. Oceanic studies have found clear trends between competing variables that define surface energy budgets, including wind speed and direction, incoming shortwave radiation, longwave radiation, water clarity and prevailing currents (Kara et al. 2007). Similar approaches have been taken in Great Lakes circulation models. However, within these models lakes are treated as whole systems and to increase the efficiency of the models, the water clarity parameters have been homogenized across the lakes based on the predominant optical properties. It is in the author's opinion that all participating variables be considered to the fullest capacity through nested models.

For this study, a complex but somewhat expected picture of the interactions between wind, solar irradiance, and air temperature was seen when analyzing the data. Solar irradiance consistently heats the water column, with the distribution of this heat subject to turbulence in the water column. Mean wind speeds above 8 $m \cdot s^{-1}$, and persistent

mean winds above 5 $m \cdot s^{-1}$, result in deeper mixing of warm surface waters. The depth of this mixing, and whether full water column mixing occurs, relies both on the duration and speed of these wind events.

Warm air temperatures help to insulate surface waters, resulting in exaggerated diel warming signals during calm, warm air periods. Again, this is expected, as the air-sea boundary layer becomes increasingly stable, or less unstable, under these conditions (Blanken et al. 2011). Local (surface) heating is exaggerated in Green Bay waters, with significant diel warming seen at Station 8. The end result appears to be significant fluxes of heat out of surface waters and into the atmosphere in these waters, resulting in less heating of the water column as a whole. Initially, it was expected that warmer surface waters due to increased local heating would result in higher rates of convective mixing as surface waters would cool more rapidly during the evening hours. However, it appears that much of the increased solar absorption occurs at a depth in the water column which allows for rapid outflux of this heat into the atmosphere, as inspection of continuous temperature mooring data suggests that cooling of surface waters occurs at similar rates across stations (except for Station 8).

While many of the findings within this study were not significant, several followed established trends. The heat flux for this study agrees well with previous studies when considering periods of net positive and net negative flux for the bay. However, flux values tended to be larger and more variable, likely due to the large advection terms in this system. Previous studies worked in systems where advection did not play as significant a role. Schertzer (1987) found mean monthly values that, when converted to like units, result in flux values of approximately 115-125 $W \cdot m^{-2} day^{-1}$ during the months of June and July. This study found net flux values become negative near the end of August, approximately 1-2 weeks later than the average period for Lake Erie switching to net negative flux values

(Schertzer 1987). The degree of variance both interannually and in the calculations of flux values suggests close agreement with findings on Lake Erie.

Bennett (1978) found peak surface temperatures in all of the Great Lakes to be significantly below surface temperatures seen within this study across mooring data (including Chambers West), as well as flux values that are below those found in this study and in better agreement with those found by Schertzer (1987). Lofgren and Zhu (2000) also found that the earliest net negative flux out of the Great Lakes occurred in Lake Erie, near the end of August, a finding similar to the results from this study. The peak surface temperatures for all sampled stations was much above the peak surface temperatures observed by Schertzer et al. in the western basin of Lake Erie (1987).

This study compares well with previous studies considering the abnormal spring and summer in 2012. For all NCDC divisions sharing coastline with Green Bay, March 2012 was the warmest March on record. Additionally, July 2012 was rated as 0.96 on a scale of 1, indicating above average temperatures observed during that month. Overall, the spring and summer periods for 2012 were above average as a whole. When comparing 2012 data from Station 9 to data from 2011, it is evident that the water column contained much more thermal energy in 2012, with comparative early summer stratification at Station 9 occurring at least five days earlier in 2012 than in 2011. Additionally, the 2012 water column at Station 9 took two weeks longer to cool and reach the same isothermal conditions observed in 2011, a finding that agrees well with the THERMOS study in which a Norwegian lake was thermally manipulated (Lydersen et al. 2008).

Warming trends observed within this study suggest that Green Bay is following fairly typical trends in many ways, including an increased summer heat gain and warmer surface temperatures (Blanken et al. 2011). However, previous studies have suggested that a shallowing of the mixed layer and a more stable thermocline will be present (King et al.

1997). If these conditions occur in Green Bay, hypoxic conditions in the hypolimnion will be further aggravated. Current research has seen an increase in hypoxia in lower Green Bay, which correlates with more frequent cold water incursions into the bay (Valenta et al. 2012). This study finds that, in the mid-bay, a deepening of the mixed layer has occurred, to the point that many stations experience full water column mixing throughout the summer. These conditions are only changed upon the arrival of cold water intrusions, which form a temporary thermocline that separates the benthic water mass from overlying waters. It is very likely that these water masses displace already oxygen deficient waters into the lower bay, which likely explains the findings by Valenta et al. (in prep). Thus, while incoming waters from the northern bay and Lake Michigan may be better oxygenated, the hypoxia and anoxia is likely a result of both high sediment oxygen demand and the persistent separation of water masses from atmospheric re-oxygenation. The dynamics of these cold water intrusions were tracked to a better degree in this study, but the overall dynamics, including the cause of these events, still requires further research.

4.2 Conclusions

Green Bay exhibited a persistent, stable thermocline throughout the summer months at stations with a depth greater than 15 meters. However, occasional breakdown of the thermocline occurred, resulting in full water column mixing, with re-formation of the thermocline occurring with subsequent cold water intrusions. Stations that have shown small thermoclines in the past for most of the summer months exhibited only periodic stratification for this warmer than average field year (e.g. Station 17). Shallow, southerly sites only displayed a thermocline and strong stratification when cold water masses entered southern Green Bay.

The role of water clarity on the thermal structure of Green Bay was not determined. Significant surface heating occurred at more turbid stations but with significant daily

variability, resulting in no established trends. The heating of surface waters, and the resultant air-sea fluxes, were heavily dependent on prevailing meteorological conditions. Periods of high solar irradiance did show more extensive surface heating at southerly stations than northerly stations. However, these results are not conclusive with turbidity, as the advection terms were quite large.

Overall, the stability of the atmospheric boundary layer (ABL) was quite variable. However, the stability of the ABL, based on calculated air-sea fluxes, followed established trends in that overall stability was higher in the early summer months and lower in the late summer and early fall. Latent and sensible heat fluxes were highest, particularly for extended periods, later in the season. The effect of wind direction could not be ascertained within this study; however, wind speed plays a significant role in the overall flux terms and thermal structure of the bay.

Other researchers have worked on basins within large lakes to better determine the physics of the systems, as well as working within multiple basins of moderately sized lakes (~60 km^2) (King et al. 1997; King et al. 1999a). These studies give great insight into the processes of large systems while maintaining the integrity of the data through scope and scale. Considering the variable nature of surface heating across southerly sites with similar k_d, more extensive studies are needed over either the same region or within a smaller area, preferably with more accurate equipment. While the general physics of the system are understood, more baseline information is needed, particularly considering the activity of cold water intrusions into the southern bay. This information is vital to recovery efforts for the bay, especially when attempting to understand the outcome of potential effects due to climate change.

When considering the findings of this study within the context of previous research, it becomes evident that summer-time energetics are following similar, but exaggerated,

trends (Bennett 1978; Schertzer 1987; Lofgren and Zhu 2000; Blanken et al. 2011). Surface water temperatures will likely be much above average in years with abnormally warm spring and summer periods, and the heating of the mixed layer in Green Bay will result in erosion of hypolimnetic waters to a point where full water column mixing becomes increasingly common. While this is somewhat unexpected, as a higher temperature differential should lead to stronger stratification, Green Bay is a well-mixed system. The meteorological energetics, along with an increased thermal capacity to rapidly erode and incorporate smaller, cold water masses, are expected to result in a decrease in stratification. Further attention should be paid to climate trends using the near real-time monitoring buoy deployed in the bay, with attention also paid to cloud cover estimates and resultant surface and whole water column temperatures.

References

Babin, M., D. Stramski, G. M. Ferrari, H. Claustre, A. Bricaud, G. Obolensky, N. Hoepffner. 2003. Variations in the light absorption coefficients of phytoplankton, nonalgal particles, and dissolved organic matter in coastal water around Europe. *J. Geophys. Res*. 108 (C7), 3211.

Beardsley, R. C., E. P. Dever, S. J. Lentz, J. P. Dean. 1998. Surface heat flux variability over the northern California shelf. *J. Geophys. Res*. 103(310): 21553-21586.

Bennett, E. B. 1978. Characteristics of the thermal regime of Lake Superior. *J. Great Lakes Res.* 4(3-4): 310-319.

Blanken, P. D., C. Spence, N. Hestrom, J. D. Lenters. 2011. Evaporation from Lake Superior: 1. Physical controls and processes. *J. Great Lakes Res*. 37: 707-716.

Boothe, R. G. 2002. *Perception of the visual environment*. Springer-Verlag. New York.

Boyce, F. M. 1974. Some aspects of Great Lakes physics of importance to biological and chemical processes. *J. Fish. Res. Board Can.* 31: 689-730.

Boyer, G. L. 2008. Cyanobacterial toxins in New York, in Ed. H. Kenneth Hudnell *Cyanobacterial harmful algal blooms: State of the science and research needs*. Advances in experimental medicine and biology, Vol. 619: 153-165.

Brutsaert, W. H. 1982. *Evaporation into the atmosphere: Theory, history, and applications*. D. Reidel, Dordrecht, Netherlands.

Burns, N. M., D. C. Rockwell, P. E. Bertram, D. M. Dolan, J. J. H. Ciborowski. 2005. Trends in temperature, Secchi depth, and dissolved oxygen depletion rates in the central basin of Lake Erie, 1983-2002. *J. Great Lakes Res*. 31(Supplement 2): 35-49.

Crawford, T. M., and C. E. Duchon. 1999. An improved parameterization for estimating effective atmospheric emissivity for use in calculating daytime downwelling longwave radiation. *J. Appl. Meteorol*. 38(4): 474-480.

Dobiesz, N. E., and N. P. Lester. 2009. Changes in mid-summer water temperature and clarity across the Great Lakes between 1968 and 2002. *J. Great Lakes Res.* 35: 371-384.

Duarte, H. F., N. L. Dias, S. R. Maggiotto. 2006. Assessing daytime downward longwave radiation estimates for clear and cloudy skies in southern Brazil. *Agric. For. Meteorol*. 139(3-4): 171-181.

Effler, S. W., M. G. Perkins, F. Peng, C. Strait, A. D. Weidemann, M. T. Auer. 2010. Light-absorbing components in Lake Superior. *J. Great Lakes Res*. 36: 656-665.

Fee, E. J., R. E. Hecky, S. E. M. Kasian, D. R. Cruikshank. 1996. Effects of lake size, water clarity, and climatic variability on mixing depths in Canadian Shield Lakes. *Limnol. Oceanogr.* 41(5): 912-920.

Frenette, J., M. T. Arts, J. Morin, D. Gratton, C. Martin. 2006. Hydrodynamic control of the underwater light climate in fluvial Lac Saint-Pierre. *Limnol. Oceanogr*. 51: 2632-2645.

Gebremariam, S.Y., J.F. Martin, C. Demarchi, E. Irwin, W. Zhang, N. Chen, S.A. Ludsin. 2013. Impacts of crop management practices in the Maumee watershed on dissolved phosphorus inputs to Lake Erie, presented at the 56th Annual International Conference on Great Lakes Research, Int. Assoc. of Great Lakes Res., West Lafayette, IN, USA.

Gnanadesikan, A., and W. G. Anderson. 2009. Ocean water clarity and the ocean general circulation in a coupled climate model. *Journal of Physical Oceanography*. 39: 314-332.

Gorham, E., and F. M. Boyce. 1989. Influence of lake surface area and depth upon thermal stratification and the depth of the summer thermocline. *J. Great Lakes Res.* 15(2): 233-245.

Gottlieb, E. S., J. H. Saylor, G. S. Miller. 1990. Currents and water temperatures observed in Green Bay, Lake Michigan. Part I: Winter 1988-1989, Part II: Summer 1989, NOAA GLERL TM-073.

Graham, L. E., J. M. Graham, L. W. Wilcox. 2009. *Algae*. 2nd Ed. Pearson Education, Inc. New York, NY. 616 p.

Gunn, J. M., E. Snucins, N. D. Yan, M. T. Arts. 2001. Use of water clarity to monitor the effects of climate change and other stressors on oligotrophic lakes. *Environmental Monitoring and Assessment.* 67: 69-88.

Hamidi, S. A., H. R. Bravo, J. V. Klump. In prep. Water exchange between Green Bay and Lake Michigan, wind direction and internal oscillations.

Hecky, R. E., R. E. H. Smith, D. R. Barton, S. J. Guildford, W. D. Taylor, M. N. Charlton, T. Howell. 2004. The nearshore phosphorus shunt: a consequence of ecosystem engineering by dreissenids in the Laurentian Great Lakes. *Can. J. Fish Aquat. Sci.* 61: 1285-1293.

Henderson-Sellers, B. 1986. Calculating the surface energy balance for lake and reservoir modeling: A review. *Rev. Geophys*. 24: 625-649, doi:10.1029/RG024i003p00625.

Houser, J. N. 2006. Water color affects the stratification, surface temperature, heat content, and mean epilimnetic irradiance of small lakes. *Can. J. Fish Aquat. Sci*. 63: 2447-2455.

Kara, A. B., A. J. Wallcraft, H. E. Hurlburt. 2005. How does solar attenuation depth affect the ocean mixed layer? Water turbidity and atmospheric forcing impacts on the

simulation of seasonal mixed layer variability in the turbid Black Sea. *Journal of Climate*. 18(3): 389-409.

Kara, A. B., H. E. Hurlburt, W.-Y. Loh. 2007. Which near-surface atmospheric variable drives air-sea temperature differences over the global ocean? J. *Geophys. Res.* 112, C05020, doi:10.1029/2006JC003833.

Kennedy, J.A. 1982. Water-mass structures and exchanges in Green Bay, Lake Michigan. Thesis.

King, J. R., B. J. Shuter, A. P. Zimmerman. 1997. The response of the thermal stratification of South Bay (Lake Huron) to climatic variability. *Can. J. Fish Aquat. Sci.* 54: 1873-1882.

King, J. R., B. J. Shuter, A. P. Zimmerman. 1999a. Signals of climate trends and extreme events in the thermal stratification pattern of multibasin Lake Opeongo, Ontario. *Can. J. Fish Aquat. Sci.* 56: 847-852.

King, J. R., B. J. Shuter, A. P. Zimmerman. 1999b. Empirical links between thermal habitat, fish growth and climate change. *Trans. Am. Fish. Soc.* 128: 656-665.

Kirk, J.T.O. 1994. *Light and Photosynthesis in Aquatic Ecosystems*. 2nd Ed. Cambridge University Press. New York, NY. 509 p.

Klump, J. V., D. Edgington, P. Sager, D. Robertson. 1997. *Sedimentary phosphorus cycling and a phosphorus mass balance for the Green Bay (Lake Michigan) ecosystem.* Can. J. fish. Aquat. Sci. 54: 10-26.

Klump, J. V., S. A. Fitzgerald, J. T. Waples. 2009. Benthic biogeochemical cycling, nutrient stoichiometry, and carbon and nitrogen mass balances in a eutrophic freshwater bay. *Limnol. Oceanogr.* 54(3): 692-712.

Kruk, N. S., I. F. Vendrame, J. R. da Rocha, S. C. Chou, O. Cabral. 2010. Downward longwave radiation estimates for clear and all-sky conditions in the Sertãozinho region of São Paulo, Brazil. *Theor. Appl. Climatol*. 99: 115-132. DOI 10.1007/s00704-009-0128-7.

Lam, D. C. L., W. M. Schertzer, A. S. Fraser. 1983. Simulation of Lake Erie water quality responses to loading and weather variations. IWD, Scientific Series 134, NWRI, Canada Centre for Inland Waters.

Lathrop, R. G., J. R. Vande Castle, T. M. Lillesand. 1990. Monitoring river plume transport and mesoscale circulation in Green Bay, Lake Michigan, through satellite remote sensing. *J. Great Lakes Res.* 16(3): 471-484.

Liu, P. C., and D. B. Ross. 1980. Airborne measurements of wave growth for stable and unstable atmospheres in Lake Michigan. *Journal of Physical Oceanography*. 10: 1842-1853.

Lofgren, B. M., and Y. Zhu. 2000. Surface energy fluxes on the Great Lakes based on satellite-observed surface temperatures 1992 to 1995. *J. Great Lakes Res*. 26(3): 305-314.

Lydersen, E., K. J. Aanes, S. Andersen, P. Brettum, T. Baekken, L. Lien, E. A. Lindstrom, J. E. Løvik, M. Mjelde, T. J. Oredalen, A. L. Solheim, R. Romstad, R. F. Wright. Ecosystem effects of thermal manipulation of a whole lake, Lake Breisjøen, southern Norway (THERMOS project). *Hydrol. Earth Syst. Sci*. 12: 509-522.

Mazumder, A., and W. Taylor. 1994. Thermal structure of lakes varying in size and water clarity. *Limnol. Oceanogr.* 39(4): 968-976.

McInnes, A., and A. Quigg. 2010. *Near-annual fish kills in small embayments: Casual vs. causal factors.* Jour. of Coastal Res. 26(5) 957-966.

McKinley, K. R., and R. G. Wetzel. 1979. Photolithotrophy, photoheterotrophy, and chemoheterotrophy: Patterns of resource utilization on an annual and diurnal basis within a pelagic microbial community. *Microbial Ecology*. 5: 1-15.

Miller, G. S., and J. H. Saylor. 1985. Currents and temperature in Green Bay, Lake Michigan. *J. Great Lakes Res.* 11(2): 97-109.

Morel, A., H. Claustre, D. Antoine, B. Gentili. 2007. Natural variability of bio-optical properties in Case I waters: Attenuation and reflectance in the visible and near-UV spectral domains, as observed in South Pacific and Mediterranean waters. *Biogeosciences*. 4: 913-925.

Mortimer, C. H. 1978. Water movement, mixing, and transport in Green Bay, Lake Michigan. In *Research Needs for Green Bay*, pp. 10-56. UW Sea Grant Report WIS-SG-78-234.

Murtugudde, R., J. Beauchamp, C. R. McClain, M. Lewis, A. Busalacchi. 2002. Effects of penetrative radiation on the upper tropical ocean circulation. *J. Climate*. 15: 470-486.

Perez-Fuentetaja, A., P. J. Dillon, N. D. Yan, D. J. McQueen. 1999. Significance of dissolved organic carbon in the prediction of thermocline depth in small Canadian shield lakes. *Aquat. Ecol*. 33: 127-133.

Pope, R. M., and E. S. Fry. 1997. Absorption spectrum (380-700 nm) of pure water. II. Integrating cavity measurements. *Appl. Opt*. 36: 8710-8723.

Reed, R. K. 1976. On the estimation of net long-wave radiation from the oceans. *J. Geophys. Res*. 81:5793-5794.

Sadro, S. J. M. Melack, S. MacIntyre. 2011. Depth-integrated estimates of ecosystem metabolism in a high-elevation lake (Emerald Lake, Sierra Nevada, California). *Limnol. Oceanogr*. 56: 1764-1780.

Sager, P. E., G. Banta, J. Kirk. 1984. The relation between areal and volumetric expressions of ^{14}C productivity in Green Bay, Lake Michigan. *Verh. Internat. Verein. Limnol*. 22: 470-474.

Sager, P. E., and S. Richman. 1991. Functional interaction of phytoplankton and zooplankton along the trophic gradient in Green Bay, Lake Michigan. *Can. J. Fish. Aquat. Sci*. 48: 116-122.

Schertzer, W. M. 1978. Energy budget and monthly evaporation estimates for Lake Superior. *J. Great Lakes Res.* 4: 320-330.

Schertzer, W. M. 1987. Heat balance and heat storage estimates for Lake Erie, 1967 to 1982. *J. Great Lakes Res.* 13(4): 454-467.

Schertzer, W. M., J. Saylor, F. Boyce, D. Robertson, F. Rosa. 1987. Seasonal thermal cycle of Lake Erie. *J. Great Lakes Res.* 13(4): 468-486.

Schneider, E., and Z. Zhu. 1998. Sensitivity of the simulated annual cycle of sea surface temperature in the equatorial Pacific to sunlight parameterization. *J. Climate*. 11: 1932-1950.

Schwab, D. J., and D. Beletsky. 2003. Relative effects of wind stress curl, topography, and stratification on large scale circulation in Lake Michigan. J. Geophys. Res. 108(C2): 26-1 to 26-6.

Simpson, J. J., and T. D. Dickey. 1981. The relationship between downward irradiance and upper ocean structure. *J. Phys. Oceanogr.* 11: 309-323.

Snucins, E., and J. Gunn. 2000. Interannual variation in the thermal structure of clear and colored lakes. *Limnol. Oceanogr*. 45(7): 1639-1646.

Sridhar, V., and R. L. Elliott. 2002. Development of a simple downwelling longwave radiation scheme. *Agric. For. Meteorol*. 112(3-4): 237-243.

Valenta, T.J., J. A. Kennedy, J. V. Klump, D. M. Dolan, P. E. Sager. 2012. Thermal stratification and oxygen depletion in the hypolimnion of the deep waters of Green Bay, presented at the 55th Annual International Conference on Great Lakes Research, Int. Assoc. of Great Lakes Res., Cornwall, ON, CA.

Verburg, P. and J. P. Antenucci. 2010. Persistent unstable atmospheric boundary layer enhances sensible and latent heat loss in a tropical great lake: Lake Tanganyika. *J. Geophys. Res*. 115, D11109, doi:10.1029/2009JDo12839.

Waples, J. T., and J. V. Klump. 2002. Biophysical effects of a decadal shift in summer wind direction over the Laurentian Great Lakes. *Geophys. Res. Letters*. 29: 10.1029/2001GL014564.

Wetzel, R. G. 1992. Gradient-dominated ecosystems: sources and regulatory functions of dissolved organic matter in freshwater ecosystems. *Hydrobiologia.* 229: 181-198.

WICCI. 2011. Wisconsin Initiative on Climate Change Impacts. www.wicci.wisc.edu

Appendix A: HOBO pendant response curve

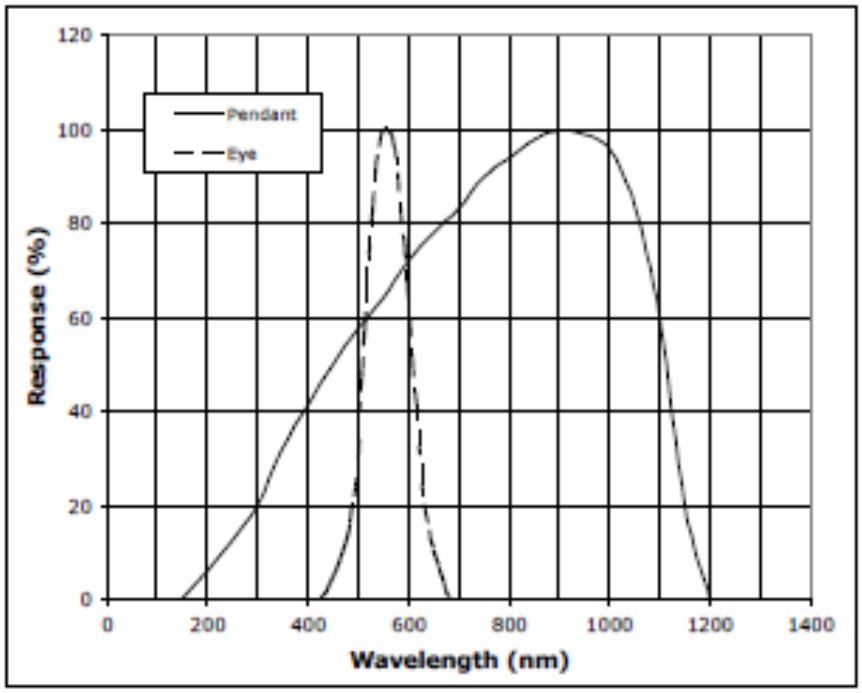

Appendix B: Heat Budget Script

```
#Includes components or entirety of: "solarclouds.R", "Verburg&Antenucci2010 sensheat script.R"

Met<-read.csv("C:/Users/Brice/Desktop/GB Buoy/GB17/2012/Excel Files/2012MetData.csv",
header=T)
WT<-read.csv("C:/Users/Brice/Desktop/GB Buoy/GB17/2012/Excel Files/2012tempprof.csv",
header=T)
setwd("C:/Users/Brice/Desktop/MS")

#-----------------------------------------------------------
#Cloud Cover calculations

TIME.Met<-as.character(Met$Date.Time)
TIME.Met<-strptime(TIME.Met,format="%m/%d/%Y %H:%M")

MetCloud <-array()
MetSolarHourMax <-array()

for (day in 183:285){
 dayfilter <-TIME.Met$yday>=day-14 & TIME.Met$yday<=day+14
 for (hour in 0:23) {
  hourfilter <-TIME.Met$hour == hour & dayfilter
  maxhour <-max(Met$SolarRad[hourfilter],na.rm=TRUE)
  MetSolarHourMax[hourfilter] <-maxhour
 }
}
#for loops above calculate the maximum irradiance value for a 4 week moving window, where the
current day acts
#as the center point, with the 14 days before and after considered for the maximum value

zerofilter <-MetSolarHourMax < 10       #occassionally night values were below
                        #10 but above 0, likely moonlight (lunar cycle) or shiplight
SolarRad = Met$SolarRad
SolarRad[zerofilter] = NA
MetSolarHourMax[zerofilter] = 1         #maximum irradiance is set to 1 ([zerofiler], i.e. only consider
non-zero values)

MetCloud <- 1-(SolarRad/MetSolarHourMax)  #fraction of cloud cover, determined dividing the
observed irradiance by maximum irradiance
                        #determined above; 1-(value) is to obtain the fraction of cloud cover
MetCloud

GB<-read.csv("C:/Users/Brice/Desktop/GBmet2012summer.csv", header=T)

TIME.GB<-as.character(GB$Date.Time)
TIME.GB<-strptime(TIME.GB,format="%m/%d/%Y %H:%M")

July<-which(TIME.GB$mon==6)
August<-which(TIME.GB$mon==7)
September<-which(TIME.GB$mon==8)
October<-which(TIME.GB$mon==9)

sky<-as.character(GB$Sky.Condition)
sky2<-as.character(GB$Sky.Condition.2)
```

```
sky3<-as.character(GB$Sky.Condition.3)

sky<-ifelse(sky=="CLR", 0, sky)        #assigning fractions to character strings, based on
documentation
sky<-ifelse(sky=="FEW", 0.125, sky)
sky<-ifelse(sky=="SCT", 0.45, sky)
sky<-ifelse(sky=="BKN", 0.75, sky)
sky<-ifelse(sky=="OVC", 1.0, sky)
sky<-ifelse(sky=="M", NA, sky)
sky<-ifelse(sky=="VV", NA, sky)

sky2<-ifelse(sky2=="", NA, sky2)
sky2<-ifelse(sky2=="FEW", 0.125, sky2)
sky2<-ifelse(sky2=="SCT", 0.45, sky2)
sky2<-ifelse(sky2=="BKN", 0.75, sky2)
sky2<-ifelse(sky2=="OVC", 1.0, sky2)

sky3<-ifelse(sky3=="", NA, sky3)
sky3<-ifelse(sky3=="FEW", 0.125, sky3)
sky3<-ifelse(sky3=="SCT", 0.45, sky3)
sky3<-ifelse(sky3=="BKN", 0.75, sky3)
sky3<-ifelse(sky3=="OVC", 1.0, sky3)

sky<-as.numeric(sky)
sky2<-as.numeric(sky2)
sky3<-as.numeric(sky3)

sky.m<-matrix(nrow=3000,ncol=3)
sky.m[,1]<-sky
sky.m[,2]<-sky2
sky.m[,3]<-sky3

skyMeans <-rowMeans(sky.m,na.rm=TRUE)     #integrating multiple cloud fractions for hourly
periods into one mean value for that hour
skyMeans

GB[,ncol(GB)+1]<-skyMeans              #adding the mean cloud fractions onto the original GB data
frame

Met[,ncol(Met)+1]<-MetCloud            #adding the cloud fractions onto the original buoy data frame

metarray<-array()

for (myrow in 1:length(TIME.Met$yday)){

 thishourfilter <-which(TIME.GB$hour == TIME.Met$hour[myrow] & TIME.GB$yday ==
TIME.Met$yday[myrow])
 thishourfilter=thishourfilter[length(thishourfilter)]
 metarray[myrow] <- GB$V20[thishourfilter]
}

met.m<-matrix(nrow=4932, ncol=1)
met.m<-metarray

cloudarray<-array()
```

```
cloudarray<-ifelse(is.na(Met$V10), met.m, Met$V10)

#-------------------------------------------------------

x<-WT$Julian.Day
match<-match(x, Met$Julian.Day)                #syncing t-string data with met data (due to some data
missing for each dataset)

MetDF<-matrix(nrow=length(match),ncol=9)          #ncol is the number of columns in the original
dataset
MetDF<-data.frame(Met[match,])

cloudfractionmatrix<-matrix(nrow=4932, ncol=2)
cloudfractionmatrix[,1]<-Met$Julian.Day
cloudfractionmatrix[,2]<-cloudarray

match<-match(x, cloudfractionmatrix[,1])

cloudfractionDF<-matrix(nrow=length(match), ncol=2)
cloudfractionDF<-data.frame(cloudfractionmatrix[match,])
c <-cloudfractionDF[,2]                    #fraction cloud cover

#Constants used in the calculations
const_SpecificHeatAir = 1005          #Units : J kg-1 K-1
const_vonKarman = 0.41              #Units : none
const_Gravity = 9.81                #Units : m s-2
const_Charnock = 0.013              #Units : none


Ts <-WT$X1m                #Surface temperature, water
Ta <-MetDF$AirTemp          #air temperature (buoy met station)
P <- MetDF$Rel.BP           #hPa, equivalent to mbar (mbar used in V&A 2010)
Uz <-MetDF$WindSp
RH <-MetDF$RH
z <-rep(1.5, 4828)          #met station height on buoy, in meters
print(length(Uz))

filter = (!is.na(Ts)) & (!is.na(Ta)) & (!is.na(P)) & (!is.na(Uz)) & (!is.na(RH)) & (!is.na(z))
print(sum(filter))
Ts=Ts[filter]
Ta=Ta[filter]
P=P[filter]
Uz=Uz[filter]
RH=RH[filter]
z=z[filter]
c=c[filter]

#-------------------------------------------------------
#Function list, used by script below
#-------------------------------------------------------

PSIM=function(zeta) {
 psim=NA
 #function psim=PSIM(zeta)
 #Function to compute stability functions for momentum
```

```
 if (zeta < 0) {
  X = (1 - 16*zeta)^0.25
  psim = 2*log((1 + X)/2) + log((1 + X*X)/2)-2*atan(X) + pi/2

 } else if (zeta > 0) {    #Stable case
  if (zeta > 0.5) {
   if (zeta > 10.0) {
    psim = log(zeta) - 0.76*zeta - 12.093
   } else {
    psim = 0.5/(zeta*zeta) - 4.25/zeta - 7.0*log(zeta) - 0.852
   }
  } else {
   psim = -5*zeta
  }
 }else{
  psim = 0
 }
 return(psim)
}

#-------------------------------------------------------
PSITE=function(zeta) {
 psite=NA
 #Function to compute stability functions for sensible and latent heat
 if (zeta < 0.0) {
  X = (1 - 16*zeta)^0.25
  psite = 2*log((1 + X*X)/2)

 } else if (zeta > 0.0) {    #Stable case
  if (zeta > 0.5) {
   if (zeta > 10.0) {
    psite = log(zeta) - 0.76*zeta - 12.093
   } else {
    psite = 0.5/(zeta*zeta) - 4.25/zeta - 7.0*log(zeta) - 0.852
   }
  } else {
   psite = -5*zeta
  }
 } else {
  psite = 0.0
 }
 return(psite)
}

#-------------------------------------------------------

compute_senslatentheat <- function(Uz,Ta,Ts,RH,P,z){

#USAGE

#    mm=compute_senslatentheat(Dates,Uz,Ta,Ts,RH,p,z);

#Script to compute surface thermodynamic fluxes (sensible and latent) using the
#bulk aerodynamic approach taking into account atmospheric stability,
#including roughness lengths of momentum, vapor and temperature
```

```
#This set of scripts was constructed by Piet Verburg and Jason P. Antenucci

#Please reference the following paper if this script is of use to you.
#Verburg, P. and J.P. Antenucci. 2010. Persistent unstable atmospheric boundary layer
#enhances sensible and latent heat loss in a tropical great lake: Lake Tanganyika.
#Journal of Geophysical Research - Atmospheres 115, D11109. doi:
  #10.1029/2009JD012839

#Input
  #Uz:   Wind Speed at the measurement height (m/s)
  #Ta:    Air Temperature at the measurement height (degrees C)
  #Ts:   Surface Water Temperature (degrees C)
  #RH:   Relative Humidity (%)
  #P :   Air Pressure (mb)
  #z:    Wind Sensor Height (m)

# Output
#   mm=[RH Ta Ts U_Z u_star zeta L C_H C_HN C_D C_DN E Evap H z_0 z_E z_T del_theta];

#Last update 2010-10-11

#Step 2c - Compute saturated vapour pressure at air temperature
es<-6.11*exp((17.27*Ta)/(237.3+Ta))  #Units : mb ##REF##
#Step 2d - Compute vapour pressure
ea<-(RH*es)/100  #Units : mb
#End step 2


#Step 3 - Compute other values used in flux calculations
#Step 3a - Compute specific humidity
qz <-(0.622*ea)/P   #Units: kg kg-1
#Step 3b - Compute saturated vapour pressure at water temperature
esat<-6.11*exp((17.27*Ts)/(237.3+Ts))  #Units : mb ##REF##
#Step 3c - Compute humidity at saturation (Henderson-Sellers 1986 eqn 36)
qs <-(0.622*esat)/P   #Units: kg kg-1
#Step 3d - Compute latent heat of vaporisation
Lv <-2.501e6 - 2370*Ts  #Units : J kg-1 ** EQUATION FROM PIET ##REF##
#Step 3e - Compute gas constant for moist air
Ra <-287*(1+0.608*qz)  #Units : J kg-1 K-1
#Step 3f - Compute air density
pa <-(100*P)/(Ra*(Ta+273.16))  #Units : kg m-3
#Step 3g - Compute kinematic viscosity of air
v = (1/pa)*(4.94e-8*Ta + 1.7184e-5);  #Units : m2 s-1
#Step 3h - Compute virtual air temperature and virtual air-water temperature difference
Tav = (Ta+273.16)*(1+0.61*qz)  #Units - K
Tsv = (Ts+273.16)*(1+0.61*qs)  #Units - K
del_theta = Tsv - Tav
#Step 3h - Compute water density
pw = 1000*(1-1.9549*0.00001*abs(Ts-3.84)^1.68)
#End step 3

#Step 4 - Compute initial estimates of neutral transfer coefficients. This contains an iteration loop
#Step 4a - Compute initial approximation to AIR shear velocity
```

```
u_star = Uz*sqrt(0.00104+0.0015/(1+exp((-Uz+12.5)/1.56)))              #Amorocho and DeVries,
initialise ustar using Uz
#Step 4b - Compute initial roughness length for momentum
z_0 = (const_Charnock*u_star^2/const_Gravity) + (0.11*v/u_star)          #Units: m
#Step 4c - Iterate initial u_star
sprintf('Computing neutral coefficients\n')
z_0_prev=z_0*1.1                                          #To initiate the iteration


for (i in 1:length(Uz)){
 if(is.finite(abs(z_0_prev[i])) && (abs(z_0_prev[i]) > 0.000001)){          #&& is for a scalar
  while (abs((z_0[i] - z_0_prev[i]))/abs(z_0_prev[i]) > 0.000001) {          #Converge when z_0
within 0.0001 of previous value
    u_star[i]=const_vonKarman*Uz[i]/(log(z[i]/z_0[i]))                    #Compute u_star
    dummy = z_0[i]                                        #Used to control while loop
    dummy2=(const_Charnock*u_star[i]^2/const_Gravity) + (0.11*v[i]/u_star[i])    #Compute new
roughness length
    z_0_prev[i] = dummy
    if(!is.finite(dummy2))break
    z_0[i]=dummy2
  }
 }                                                  #Used to control while loop
}

#Step 4d - Compute initial neutral drag coefficient
C_DN = (u_star^2)/(Uz^2)                                  #Units - none
#Step 4e - Compute roughness Reynolds number
Re_star = u_star*z_0/v                                    #Units - none
#Step 4f - Compute initial roughness length for temperature
z_T = z_0*exp(-2.67*(Re_star)^(1/4) + 2.57)                        #Units - m
#z_T = real(z_T)                                          #Get real components, and NaN can create imag
component despite no data
#Step 4g - Compute initial roughness length for vapour
z_E = z_0*exp(-2.67*(Re_star)^(1/4) + 2.57)                        #Units - m
#z_E = real(z_E)                                          #Get real components, and NaN can create imag
component despite no data
#Step 4h - Compute initial neutral sensible heat transfer coefficient
C_HN = const_vonKarman*sqrt(C_DN)/(log(z/z_T))
#Step 4i - Compute initial neutral latent heat transfer coefficient
C_EN = const_vonKarman*sqrt(C_DN)/(log(z/z_E))
#End step 4

#Step 5 - Start iteration to compute corrections for atmospheric stability
H_initial = c()
E_initial = c()
L_initial = c()
zeta_initial = c()
psim = c()
psit = c()
psie = c()
C_D = c()
C_H = c()
C_E = c()
L = c()
count = c()
```

```
zeta = c()
H = c()
E = c()
L = c()

sprintf('Correcting neutral coefficients\n')
for (i in which(Uz>0)){                                    #Need to iterate separately for each record
                                                  #Step 5a - Compute initial sensible heat flux based on neutral
coefficients
 H_initial[i] = pa[i]*const_SpecificHeatAir*C_HN[i]*Uz[i]*(Ts[i]-Ta[i])          #Units : W m-2
                                                  #Step 5b - Compute initial latent heat flux based on
neutral coefficients
 E_initial[i] = pa[i]*Lv[i]*C_EN[i]*Uz[i]*(qs[i]-qz[i])                    #Units : W m-2
                                                  #Step 5c - Compute initial Monin-Obukhov length
 L_initial[i] = (-
pa[i]*u_star[i]^3*Tav[i])/(const_vonKarman*const_Gravity*(H_initial[i]/const_SpecificHeatAir +
0.61*E_initial[i]*(Ta[i]+273.16)/Lv[i]))
                                                  #Units - m
                                                  #Step 5d - Compute initial stability parameter
 zeta_initial[i] = z[i]/L_initial[i]
                                                  #Step 5e - Compute initial stability function
 psim[i]=PSIM(zeta_initial[i])                              #Momentum stability function
 psit[i]=PSITE(zeta_initial[i])                            #Sensible heat stability function
 psie[i]=PSITE(zeta_initial[i])                             #Latent heat stability function
                                                  #Step 5f - Compute corrected coefficients
 C_D[i]=const_vonKarman*const_vonKarman/(log(z[i]/z_0[i])-psim[i])^2
 C_H[i]=const_vonKarman*sqrt(C_D[i])/(log(z[i]/z_T[i])-psit[i])
 C_E[i]=const_vonKarman*sqrt(C_D[i])/(log(z[i]/z_E[i])-psie[i])
                                                  #Step 5g - Start iteration
 L_prev = L_initial[i]
 L[i] = L_prev*1.1                                      #Initialise while loop
 count[i]=0
 while (abs((L[i] - L_prev))/abs(L_prev) > 0.000001) {                    #Converge when L within
0.0001 or previous L
                                                  #Iteration counter
        count[i]=count[i]+1
  if (count[i] > 20) break
                                                  #Step 5i - Compute new z_O, roughness length for
momentum
  z_0[i]= (const_Charnock*u_star[i]^2/const_Gravity) + (0.11*v[i]/u_star[i])
                                                  #Step 5j - Compute new Re_star
  Re_star[i] = u_star[i]*z_0[i]/v[i]
                                                  #Step 5k - Compute new z_T, roughness length for
temperature
  z_T[i] = z_0[i]*exp(-2.67*(Re_star[i])^(1/4) + 2.57)
                                                  #Step 5l - Compute new z_E, roughness length for vapour
  z_E[i] = z_0[i]*exp(-2.67*(Re_star[i])^(1/4) + 2.57)
                                                  #Step 5p - Compute new stability parameter
  zeta[i] = z[i]/L[i]
                sprintf('zeta %g\n',zeta[i])
                                                  #Step 5q - Check and enforce bounds on zeta
  if (zeta[i] > 15)
        zeta[i] = 15
  else if (zeta[i] < -15)
                zeta[i] = -15;
```

```
                                        #Step 5r - Compute new stability functions
      psim[i]=PSIM(zeta[i])  #Momentum stability function
      psit[i]=PSITE(zeta[i])  #Sensible heat stability function
      psie[i]=PSITE(zeta[i])  #Latent heat stability function
                                        #Step 5s - Compute corrected coefficients
      C_D[i]=const_vonKarman*const_vonKarman/(log(z[i]/z_0[i])-psim[i])^2
      C_H[i]=const_vonKarman*sqrt(C_D[i])/(log(z[i]/z_T[i])-psit[i])
      C_E[i]=const_vonKarman*sqrt(C_D[i])/(log(z[i]/z_E[i])-psie[i])
#Step 5m - Compute new H (now using corrected coefficients)
      H[i] = pa[i]*const_SpecificHeatAir*C_H[i]*Uz[i]*(Ts[i]-Ta[i])
#Step 5n - Compute new E (now using corrected coefficients)
      E[i] = pa[i]*Lv[i]*C_E[i]*Uz[i]*(qs[i]-qz[i])
#Step 5h - Compute new u_star
      u_star[i]=sqrt(C_D[i]*Uz[i]^2)
#Step 5o - Compute new Monin-Obukhov length
      dummy = L[i]  #Used to control while loop
      L[i] = (-pa[i]*u_star[i]^3*Tav[i])/(const_vonKarman*const_Gravity*(H[i]/const_SpecificHeatAir
+ 0.61*E[i]*(Ta[i]+273.16)/Lv[i]))
      L_prev = dummy    #Used to control while loop
   }
}

for(i in which(Uz==0)){
   H[i]=0
   E[i]=0
}
#end
#end
#End step 5

#Take real values to remove any complex values that arise from missing data or NaN.
#C_D=real(C_D)
#C_E=real(C_E)
#C_H=real(C_H)
#z_0=real(z_0)
#z_E=real(z_E)
#z_T=real(z_T)

#Compute evaporation [mm/day]
Evap = 86400*1000*E/(pw*Lv)

#Clean up output signal based on any missing data points
#index=which(is.na(RH)); E(index)=NaN; H(index)=NaN; Evap(index)=NaN; zeta(index)=NaN;
ustar(index)=NaN; C_H(index)=NaN; C_D(index)=NaN; C_HN(index)=NaN; C_DN(index)=NaN;
L(index)=NaN; z_0(index)=NaN; z_E(index)=NaN; z_T(index)=NaN; del_theta(index)=NaN;
#index=which(is.na(Ta)); E(index)=NaN; H(index)=NaN; Evap(index)=NaN; zeta(index)=NaN;
ustar(index)=NaN; C_H(index)=NaN; C_D(index)=NaN; C_HN(index)=NaN; C_DN(index)=NaN;
L(index)=NaN; z_0(index)=NaN; z_E(index)=NaN; z_T(index)=NaN; del_theta(index)=NaN;
#index=which(is.na(Ts)); E(index)=NaN; H(index)=NaN; Evap(index)=NaN; zeta(index)=NaN;
ustar(index)=NaN; C_H(index)=NaN; C_D(index)=NaN; C_HN(index)=NaN; C_DN(index)=NaN;
L(index)=NaN; z_0(index)=NaN; z_E(index)=NaN; z_T(index)=NaN; del_theta(index)=NaN;
#index=which(is.na(Uz)); E(index)=NaN; H(index)=NaN; Evap(index)=NaN; zeta(index)=NaN;
ustar(index)=NaN; C_H(index)=NaN; C_D(index)=NaN; C_HN(index)=NaN; C_DN(index)=NaN;
L(index)=NaN; z_0(index)=NaN; z_E(index)=NaN; z_T(index)=NaN; del_theta(index)=NaN;
```

```
#index=which(is.na(p)); E(index)=NaN; H(index)=NaN; Evap(index)=NaN; zeta(index)=NaN;
ustar(index)=NaN; C_H(index)=NaN; C_D(index)=NaN; C_HN(index)=NaN; C_DN(index)=NaN;
L(index)=NaN; z_0(index)=NaN; z_E(index)=NaN; z_T(index)=NaN; del_theta(index)=NaN;

mm=data.frame(RH, Ta, Ts, Uz, u_star, zeta, L, C_H, C_HN, C_D, C_DN, E, Evap, H, z_0, z_E, z_T,
del_theta, pa, pw)
return(mm)
}
dataframedata = data.frame(Uz,Ta,Ts,RH,P,z)
write.table(x=dataframedata, file="formatlab.txt")
holygrail=compute_senslatentheat(Uz,Ta,Ts,RH,P,z)

#-------------------------------------------------------
#Necessary Variables from previous loop
es<-6.11*exp((17.27*Ta)/(237.3+Ta))
ea<-(RH*es)/100
qz <-(0.622*ea)/P   #Units: kg kg-1
esat<-6.11*exp((17.27*Ts)/(237.3+Ts))  #Units : mb ##REF##
qs <-(0.622*esat)/P   #Units: kg kg-1
Lv <-2.501e6 - 2370*Ts  #Units : J kg-1 ** EQUATION FROM PIET ##REF##
Ra <-287*(1+0.608*qz)  #Units : J kg-1 K-1
pa <-(100*P)/(Ra*(Ta+273.16))  #Units : kg m-3
v = (1/pa)*(4.94e-8*Ta + 1.7184e-5);  #Units : m2 s-1
Tav = (Ta+273.16)*(1+0.61*qz)  #Units - K
Tsv = (Ts+273.16)*(1+0.61*qs)  #Units - K
del_theta = Tsv - Tav
pw = 1000*(1-1.9549*0.00001*abs(Ts-3.84)^1.68)

#-------------------------------------------------------
#Longwave Calculations
sbc <-5.67e-8                    #Stefan-Boltzmann constant, W m^-2 K^-1
Em <-0.97                        #emissivity, from Lerman, Imboden & Gat, 1995

Ecl <-0.643*((ea/(Ta+273.15))^(1/7))    #clear sky emissivity
Qlw_clear <-Ecl*sbc*((Ta+273.15)^4)    #longwave radiation under clear sky conditions

Qlw <-Qlw_clear*(1+0.242*(c^0.583))

Qlw_up <-Em*sbc*((Ts+273.15)^4)         #Ts in Kelvin for calculation, L,I&G, 1995

#-------------------------------------------------------
#Shortwave Calculations
Qsw <-MetDF$SolarRad[filter]
a<-.08                           #8%, based on Schertzer 1978, estimates for May through October
                                 #using Lake Superior data from 1973
Qsw_up <-a*Qsw

#-------------------------------------------------------

H <-holygrail$H                  #sensible heat, W/m^2

E <-holygrail$E                  #latent heat, W/m^2

Evaporation <-holygrail$Evap          #evaporation, units = mm/day
```

```
Qnet <- Qsw - Qsw_up + Qlw - Qlw_up - H - E

flux.m <-matrix(nrow=4533, ncol=9)

JD <-MetDF[,1]
JD <-JD[filter]

flux.m[,1]<-JD
flux.m[,2]<-Qnet
flux.m[,3]<-Qsw
flux.m[,4]<-Qsw_up
flux.m[,5]<-Qlw
flux.m[,6]<-Qlw_up
flux.m[,7]<-H
flux.m[,8]<-E
flux.m[,9]<-Evaporation

windows()
plot(JD, E, type="p", main="Energy Flux", xlab="Julian Day", ylab="W/m^2", ylim=c(-600,1000),
col="red", pch=17)
points(JD, H, col="blue", pch=15)
points(JD, Qsw, col="orange", pch=8)
points(JD, Qlw, col="green", pch=4)
points(JD, Qnet, col="black", pch=19)

legendtxt<-c("Net", "Latent", "Sensible", "Shortwave (incoming)", "Longwave (incoming)")
legendlns<-c(lwd=1,lwd=1,lwd=1,lwd=1,lwd=1)
legendcol<-c(col="black", col="red", col="blue", col="orange", col="green")
legend("topright", legendtxt, lwd=legendlns, col=legendcol, bty="n", cex=0.7)


TimeVector = seq(flux.m[14,1], max(flux.m[,1]), 1)

matrix = matrix(nrow=100, ncol=9)

for (i in 1: length(TimeVector)-1) {
 L1<-(JD>TimeVector[i] & JD<TimeVector[i+1])
 matrix[i,1]<-mean(JD[L1])
 matrix[i,2]<-mean(Qnet[L1], na.rm=T)
 matrix[i,3]<-mean(Qsw[L1], na.rm=T)
 matrix[i,4]<-mean(Qsw_up[L1], na.rm=T)
 matrix[i,5]<-mean(Qlw[L1], na.rm=T)
 matrix[i,6]<-mean(Qlw_up[L1], na.rm=T)
 matrix[i,7]<-mean(H[L1], na.rm=T)
 matrix[i,8]<-mean(E[L1], na.rm=T)
 matrix[i,9]<-mean(Evaporation[L1], na.rm=T)
}

matrix2 = matrix(nrow=100, ncol=7)

for (i in 1: length(TimeVector)-1) {
 L1<-(JD>TimeVector[i] & JD<TimeVector[i+1])
 matrix2[i,1]<-mean(JD[L1])
 matrix2[i,2]<-mean(Qnet[L1], na.rm=T)
 matrix2[i,3]<-mean(Qsw[L1]-Qsw_up[L1], na.rm=T)
```

```
 matrix2[i,4]<-mean(Qlw[L1]-Qlw_up[L1], na.rm=T)
 matrix2[i,5]<-mean(-1*H[L1], na.rm=T)
 matrix2[i,6]<-mean(-1*E[L1], na.rm=T)
 matrix2[i,7]<-mean(Evaporation[L1], na.rm=T)
}

windows()
plot(matrix2[,1], matrix2[,2], type="l", main="Energy Flux", xlab="Julian Day", ylab="W/m^2",
ylim=c(-600,800), col="black", lwd=3, cex=2, cex.main=1.6, cex.axis=1.6, cex.lab=1.6)
lines(matrix2[,1], matrix2[,5], col="blue", lwd=3)
lines(matrix2[,1], matrix2[,3], col="orange", lwd=3)
lines(matrix2[,1], matrix2[,4], col="forestgreen", lwd=3)
lines(matrix2[,1], matrix2[,6], col="red", lwd=3)

legendtxt<-c("Net", "Latent", "Sensible", "Net Shortwave", "Net Longwave")
legendlns<-c(lwd=3,lwd=3,lwd=3,lwd=3,lwd=3)
legendcol<-c(col="black", col="red", col="blue", col="orange", col="forestgreen")
legend(x=264, y=850, legendtxt, lwd=legendlns, col=legendcol, bty="n", cex=1.4)

windows()
plot(matrix2[,1], matrix2[,2], type="p", main="Energy Flux", xlab="Julian Day", ylab="W/m^2",
ylim=c(-600,800), col="black", pch=20, cex=1.4)
points(matrix2[,1], matrix2[,5], col="blue", pch=17, cex=1.4)
points(matrix2[,1], matrix2[,3], col="orange", pch=8, cex=1.4)
points(matrix2[,1], matrix2[,4], col="forestgreen", pch=4, cex=1.4)
points(matrix2[,1], matrix2[,6], col="red", pch=3, cex=1.4)

legendtxt<-c("Net", "Latent", "Sensible", "Net Shortwave", "Net Longwave")
legendlns<-c(lwd=2,lwd=2,lwd=2,lwd=2,lwd=2)
legendcol<-c(col="black", col="red", col="blue", col="orange", col="forestgreen")
legend("topright", legendtxt, lwd=legendlns, col=legendcol, bty="n", cex=0.7)
```

Appendix C: Matching Sonde profiles to HOBO profiles

```
library(akima)
setwd("C:/Users/Brice/Desktop/2012 HOBO/July")

#---------------------------------------------------------------------

SP<-read.csv("C:/Users/Brice/Desktop/Sonde Profs 12 R/July 2012/CE.csv", header=T)

HOBO<-read.csv("C:/Users/Brice/Desktop/2012 HOBO/July/CE_july.csv", header=T)
timebase<-as.numeric(as.POSIXct("1980-01-01 00:00:00"))
timenum<-function(x) as.numeric(as.POSIXct(paste("1980-01-01", x)))-timebase
sptimenum<-timenum(SP$Time)
str(sptimenum)
HOBOtimenum<-timenum(HOBO$Time)
spmax<-max(sptimenum)
spmin<-min(sptimenum)
HOBOfilter<-HOBOtimenum>=spmin & HOBOtimenum<=spmax
HOBO<-HOBO[HOBOfilter,]

result<-aspline(x=timenum(SP$Time), y=SP$Depth, xout=timenum(HOBO$Time),
method="original")
result
windows()
plot(result)

TimeDF<-matrix(nrow=length(HOBO$Time),ncol=2)
TimeDF<-data.frame(result)
write.table(TimeDF, file="CEHOBOdepths.txt", sep="\t", quote=FALSE, row.names=FALSE)
```

Appendix D: Light-Dark Bottle Data

Bottle	June 2012		July 2012		August 2012	
	12h-respiration	12-h GPP	12h-respiration	12-h GPP	12h-respiration	12-h GPP
CLR	-0.349	0.052	-0.226	0.282	0.282	0.282
2.5	0.114	0.514	0.563	1.071	1.071	1.071
4	0.039	0.439	0.516	1.024	1.024	1.024

Bottle column indicates the type of bottle used for the experiment, with clear meaning a clear bottle, 2.5 being 2.5 wraps of screen and 4 being 4 wraps of screen around a clear bottle. Respiration was measured using a dark bottle. Data is from 2012.

*Data courtesy of Shelby LaBuhn, PhD candidate

Wrap Level	Avg. Irradiance (lum/ft^2)	Percent Available	Avg. Percent Available
Clear 6-25	8690.206994	100	
Clear 6-27	5636.121878	100	
2x 6-25	2774.898363	31.93132643	
2x 6-27	1703.130836	30.21813355	**31.07472999**
4x 6-25	1524.82381	17.54646133	
4x 6-27	451.4723127	8.010336228	**12.77839878**

Wrap level indicates the number of times screen was wrapped around an individual HOBO pendant for shading purposes. The average irradiance was taken for the period when HOBO sensors were "incubated" alongside the light/dark bottles. This time period was approximately 9 hours on June 25 and approximately 6 hours on June 27. Data is from 2013.

*Data courtesy of Troy Barber, REU intern

Algal Energetic Sink Calculations (from Section 2.3)

Minimum Primary Production Estimate

$$\frac{375\ mg\ C}{m^3 day}\left|\frac{1\ g}{1000\ mg}\right|\frac{1\ mol}{12.011\ g}\left|\frac{6.022\times10^{23}}{1\ mol}\right|\frac{1\ day}{86400\ s}\left|\frac{8hc}{5.5\times10^{-9}\ m}\right|\frac{6\ m}{} = 3.78\ W\cdot m^{-2}$$

where the units for h are J·s^{-1} and for c are m·s^{-1}

Maximum Primary Production Estimate

$$\frac{1200\ mg\ C}{m^3 day}\left|\frac{1\ g}{1000\ mg}\right|\frac{1\ mol}{12.011\ g}\left|\frac{6.022\times10^{23}}{1\ mol}\right|\frac{1\ day}{86400\ s}\left|\frac{8hc}{5.5\times10^{-9}\ m}\right|\frac{6\ m}{} = 12.08\ W\cdot m^{-2}$$

where the units for h are J·s^{-1} and for c are m·s^{-1}

*These estimates are based on primary production estimates from 2012 as shown above and are based upon an average photic depth of 6 meters.

Appendix E: Cold Water Intrusion Schematic